A&A, 686, A31 (2024)
https://doi.org/10.1051/0004-6361/202348787

Astronomy & Astrophysics

Molecular isotopologue measurements toward super star clusters and the relation to their ages in NGC 253 with ALCHEMI

J. Butterworth[1], S. Viti[1], P. P. Van der Werf[1], J. G. Mangum[2], S. Martín[3,4], N. Harada[5,6,7], K. L. Emig[2]*, S. Muller[8], K. Sakamoto[6,7], Y. Yoshimura[9], K. Tanaka[10], R. Herrero-Illana[3,11], L. Colzi[12], V. M. Rivilla[12], K. Y. Huang[1], M. Bouvier[1], E. Behrens[13], C. Henkel[14,15,16], Y. T. Yan[14], D. S. Meier[17,18], and D. Zhou[1,19,20,21]

(Affiliations can be found after the references)

Received 29 November 2023 / Accepted 10 February 2024

ABSTRACT

Context. Determining the evolution of the CNO isotopes in the interstellar medium (ISM) of starburst galaxies can yield important constraints on the ages of super star clusters (SSCs), or on other aspects and factors contributing to their evolution, such as the initial mass function (IMF). Due to the time-dependent nature of the abundances of isotopes within the ISM – as they are supplied from processes such as nucleosynthesis or chemical fractionation –, this provides the opportunity to test whether or not isotope ratios trace the ages of highly star-forming regions, such as SSCs.
Aims. The goal of this study is to investigate whether the isotopic variations in SSC regions within NGC 253 are correlated with their different ages as derived from stellar population modelling.
Methods. We measured abundance ratios of CO, HCN, and HCO^+ isotopologues in six regions containing SSCs within NGC 253 using high-spatial-resolution (1.6″, ∼28 pc) data from the ALCHEMI (ALma Comprehensive High-resolution Extragalactic Molecular Inventory) ALMA Large program. We then analysed these ratios using `RADEX` radiative transfer modelling, with the parameter space sampled using the nested sampling Monte Carlo algorithm MLFriends. These abundance ratios were then compared to ages predicted in each region via the fitting of observed star-formation tracers (such as Brγ) to `Starburst99` starburst stellar population evolution models.
Results. We determined the isotopic column density ratios across multiple regions of SSC activity in NGC 253 using non-LTE radiative transfer modelling. We do not find any significant trend with age for the CO and HCN isotopologue ratios on timescales of the ages of the SSC* regions observed. However, HCO^+ may show a correlation with age over these timescales in $^{12}C/^{13}C$.
Conclusions. The driving factors of these ratios within SSCs could be the IMF or fractionation effects. To further probe these effects in SSCs over time, a larger sample of SSCs must be observed spanning a larger age range.

Key words. astrochemistry – ISM: molecules – galaxies: active – galaxies: ISM – galaxies: starburst

1. Introduction

Starburst galaxies are characterised by vigorous star formation activity, which can lead to the emergence of super star clusters (SSCs). SSCs are typically quite young (<10 Myr) and have been observed within our Galaxy, with masses of $\sim 10^4\ M_\odot$ (Ginsburg et al. 2018). Even more massive ($\sim 10^5\ M_\odot$) clusters have been observed in starburst regions of nearby galaxies, such as NGC 4945 and NGC 253 (Leroy et al. 2018; Emig et al. 2020; Rico-Villas et al. 2020, 2022).

SSCs, as compact (∼2–3 pc) regions with high star-formation rates (SFRs) of up to $5\ M_\odot\ yr^{-1}$, serve as ideal laboratories in which to explore processes that may influence and transform the interstellar medium (ISM); in particular, the variation of the isotope ratios of carbon (C), nitrogen (N), and oxygen (O). These atoms and their isotopes are important due to their high abundances and potential to probe stellar nucleosynthesis. This is due to the differing processes by which they typically form: ^{12}C for example is believed to be primarily formed in helium burning of both low- and high-mass stars. ^{13}C on the other hand is believed to form in the CNO cycle of asymptotic giant branch (AGB) stars (Pagel 1997). Both ^{14}N and ^{15}N are thought to be produced during the CNO cycles of massive stars and in the so-called hot bottom burning of AGB stars, with a higher proportion of both ^{14}N and ^{15}N formed in intermediate-mass stars relative to massive stars. ^{15}N is also largely produced by novae (Izzard et al. 2004; Romano et al. 2017, 2019; Colzi et al. 2022). ^{16}O and ^{18}O are believed to be products of the helium-burning phase of high-mass stars (with ^{18}O, primarily formed in metal-rich stars) and ^{17}O is formed as a product of the CNO cycle of intermediate-mass stars (Wouterloot et al. 2008; Wiescher et al. 2010; Henkel et al. 2014; Romano 2022). As such, the abundances of these isotopes and their evolution with time in a star-forming region are greatly affected by the initial conditions of star formation, such as the initial mass function (IMF; Papadopoulos 2010; Papadopoulos et al. 2011).

Through the lens of submillimetre (submm) measurements, these isotopic variations are primarily traced with observations of isotopologues (isotope-bearing molecules). Thanks to the Atacama Large Millimeter Array (ALMA), it is possible to observe compact energetic sources, such as SSCs, on a resolvable scale in the starburst regions within nearby galaxies. Within the submm regime probed by ALMA, there are multiple rotational transitions of CNO-bearing isotopologues available (e.g. CO, HCN, HCO^+). Observations of these isotopologues within the star-forming regions of galaxies (e.g. SSCs) can also inform us as to the IMF (Romano et al. 2017; Romano 2022). For example, Romano et al. (2017) found that C, N, and O isotope ratios

* Jansky Fellow of the National Radio Astronomy Observatory.

imply a top-heavy IMF in nearby star-forming galaxies. Galaxies with a high SFR, such as starbursts, have been shown to possess a higher isotopic ratio of $^{12}C/^{13}C$ than more 'normal' galaxies such as the Milky Way. Chemical fractionation can also influence the observed isotopologue ratios (Roueff et al. 2015; Colzi et al. 2018, 2020, 2022; Viti et al. 2019, 2020). For instance, the presence of certain exothermic chemical reactions in the gas phase of the ISM – in which isotopes are exchanged – may lead to chemical fractionation, whereby the enhancement of certain isotopologues is favoured over others (Langer et al. 1984; Szücs et al. 2014; Loison et al. 2019; Martín et al. 2019).

CO, HCN, HCO^+, and their isotopologues have been used as tools to investigate the $^{12}C/^{13}C$ ratio in nearby galaxies (Pasquali et al. 2004; Jiang et al. 2011; González-Alfonso et al. 2012; Sliwa et al. 2013, 2014; Henkel et al. 2014; Martín et al. 2019, 2021; Tang et al. 2019) as well as in higher-redshift galaxies ($z \leq 2.5$) (Muller et al. 2006; Danielson et al. 2013; Spilker et al. 2014; Wallström et al. 2016). Meanwhile, $^{14}N/^{15}N$ has been investigated through the use of HCN and its $HC^{15}N$ isotopologue in extra-galactic sources (Henkel et al. 1998, 2018; Chin et al. 1999; Wang et al. 2009, 2014, 2016; Jiang et al. 2011; Martín et al. 2021) and $^{16}O/^{18}O$ has been investigated towards individual giant molecular clouds (GMCs) in NGC 253, using isotopologues of CO (Meier et al. 2015).

In this work, we investigated whether the observed isotope ratios in starburst regions are determined by age or whether other mechanisms drive the variations in isotope ratio, such as those proposed in Romano et al. (2017). To this end, we analysed ALMA multi-transition observations of CO, HCN, and HCO^+ and their ^{13}C, ^{15}N, ^{17}O, and ^{18}O isotopologues towards the starburst galaxy NGC 253, which we present here. We extracted these measurements from the ALMA large program imaging of the central molecular zone (CMZ) of NGC 253, named the 'ALMA Comprehensive High-resolution Extragalactic Molecular Inventory' (ALCHEMI; Martín et al. 2021).

NGC 253 is a nearby ($d \sim 3.5$ Mpc, Rekola et al. 2005) galaxy containing a nuclear starburst (SFR $\sim 2\,M_\odot\,yr^{-1}$; see Leroy et al. 2015), which accounts for ~50% of the galaxy's total star-forming activity. A previous study by Leroy et al. (2018) led to the identification of 14 SSCs located within the central molecular zone (CMZ) of NGC 253. These clusters were estimated to have masses of $\sim 10^5\,M_\odot$ with an upper limit to their ages of <10 Myr.

The broad frequency range of ALCHEMI permits the systematic study of both the physical and chemical properties of NGC 253 as viewed through molecular observations. Other studies made possible thanks to the ALCHEMI data have given rise to constraints on the high cosmic-ray ionisation rate (CRIR) nature of the galaxy (Holdship et al. 2021, 2022; Harada et al. 2021; Behrens et al. 2022), the first detection of a phosphorous-bearing molecule in extragalactic sources (Haasler et al. 2022), the identification of new methanol maser transitions (Humire et al. 2022), the use of $HOCO^+$ as a chemical tracer of CO_2 (Harada et al. 2022), and also the ability to reconstruct the shock history of the GMCs located within the CMZ of the galaxy (Huang et al. 2023).

Alongside ALMA observations of the isotopologues of CO, HCN, and HCO^+, the H39α emission was extracted from the ALCHEMI data in order to estimate the ionising photon rate with a method similar to that used by Emig et al. (2020). By combining these ionising photon rates with other tracers of significant star formation such as the Brackett gamma (Brγ) line (Pasha et al. 2020), the ages of star-forming populations can be approximated using stellar population evolution modelling (e.g. `Starburst99`; Leitherer et al. 1999, 2014). Being a near-infrared hydrogen recombination line, Brγ is primarily emitted in regions ionised by massive stars (O-, B-type stars). Brγ is also affected very little by dust attenuation (~14%), making it an extremely reliable tracer of the ages of star-forming regions. We use observations of Brγ taken with the Spectrograph for INtegral Field Observations in the Near-Infrared (SINFONI) near-infrared (1.1–2.45 μm) integral field spectrograph installed on the Very Large Telescope (VLT; Eisenhauer et al. 2003; Bonnet et al. 2004).

This paper is structured as follows: in Sect. 2, we present an overview of the ALCHEMI data used alongside the data from SINFONI. Section 3.1 covers the methods with which we extracted the spectral lines and produced the moment maps. In Sect. 3.2, we summarise the selection of the beam-sized SSC regions. In Sect. 4.1, we present an initial local thermal equilibrium (LTE) analysis of the isotopologues. This is followed by a non-LTE large velocity gradient (LVG) modelling in Sect. 4.2, performed in order to determine the physical conditions within each SSC. In Sect. 5, we show how we derived the ages of the SSCs and correlated them with the observed molecular ratios. We summarise our conclusions in Sect. 6.

2. Observations

2.1. ALMA observations

All of the ALMA observations used within this study are part of ALCHEMI (project code 2017.1.00161.L and 2018.1.00162.S). A detailed explanation of the calibration setup and of the data acquisition and imaging of this large program can be found in Martín et al. (2021). We provide a brief summary here. ALCHEMI imaged the CMZ of NGC 253 across the ALMA frequency Bands 3–7. This provided a near contiguous coverage of the frequencies from 84.2 GHz to 373.2 GHz. The nominal phase centre of the observations is $\alpha = 00^h47^m33\overset{s}{.}26$, $\delta = -25°17'17\overset{''}{.}7$ (ICRS). A common rectangular area of $50'' \times 20''$ (850×340 pc) in size at a position angle of 65° was imaged to cover the central nuclear region in NGC 253. The final homogeneous angular and spectral resolution for each of the image cubes produced from these measurements are $1\overset{''}{.}6$ (~28 pc; Martín et al. 2021) and ~10 km s^{-1}, respectively. The common maximum recoverable angular scale achieved is 15″ after combining the 12 m Array and Atacama Compact Array (ACA) measurements at all frequencies. The desired species for which the image cubes were created are summarised in Tables 1–3, which include the main most abundant isotopologues of the molecules CO, HCN, and HCO^+.

2.2. SINFONI observations

The SINFONI instrument at the ESO VLT was used to obtain infrared *J*-, *H*- and *K*-band images toward NGC 253. The SINFONI instrument is mounted at the Cassegrain focus of the Unit Telescope 4 at VLT. This paper uses the SINFONI *K* band observations first published in Müller-Sánchez et al. (2010), and a more detailed description of these observations may be found in that paper. Briefly, the observations of NGC 253 were made in visitor mode on August 28, 2005. The *K*-band observations were taken using a spatial pixel scale of 0.25″ corresponding to a field of view of $8'' \times 8''$ per frame and a spectral resolution of 68 km s^{-1}. These observations were taken primarily to observe H_2 emission across the CMZ, and therefore multiple frames were taken along the CMZ until no H_2 was observed, resulting in ten

Table 1. Transitions of CO and its isotopologues used in this work.

Species	Transition	Rest frequency [GHz]	E_u [K]	A_{ul} [s^{-1}]	Ref.
CO	1–0	115.271	5.53	7.203×10^{-8}	
	2–1	230.538	16.60	6.910×10^{-7}	1, 2, 3
	3–2	345.796	33.19	2.497×10^{-6}	
^{13}CO	1–0	110.201	6.25	6.333×10^{-8}	
	2–1	220.399	15.87	6.075×10^{-7}	3, 4, 5
	3–2	330.588	31.73	2.194×10^{-6}	
C^{17}O	1–0	112.359	5.39	6.697×10^{-8}	
	2–1	224.715	16.18	6.425×10^{-7}	3, 6
	3–2	337.061	32.35	1.805×10^{-6}	
C^{18}O	1–0	109.782	5.27	6.266×10^{-8}	
	2–1	219.560	15.81	6.012×10^{-7}	3, 7
	3–2	329.331	31.61	2.171×10^{-6}	

Notes. We use molecular data of CO and its isotopologues from: 1) Goorvitch (1994), 2) Winnewisser et al. (1997), 3) Yang et al. (2010), 4) Klapper et al. (2000), 5) Cazzoli et al. (2004), 6) Klapper et al. (2003), and 7) Klapper et al. (2001). The data were sourced from the LAMDA database (Schöier et al. 2005) and the Cologne Database for Molecular Spectroscopy (CDMS) catalogue (https://cdms.astro.uni-koeln.de/) (Müller et al. 2001, 2005; Endres et al. 2016).

Table 2. Transitions of HCN and its isotopologues used in this work.

Species	Transition	Rest frequency [GHz]	E_u [K]	A_{ul} [s^{-1}]	Ref.
HCN	1–0	88.632	4.25	2.407×10^{-5}	1
	2–1	177.261	12.76	2.311×10^{-4}	
	3–2	265.886	25.52	8.356×10^{-4}	
	4–3	354.505	42.53	2.054×10^{-3}	
H^{13}CN	1–0	86.340	4.14	2.226×10^{-5}	1, 2
	2–1	172.678	12.43	2.136×10^{-4}	
	3–2	259.012	24.86	7.725×10^{-4}	
	4–3	345.340	41.44	1.899×10^{-3}	
HC^{15}N	1–0	86.055	4.13	2.203×10^{-5}	1, 3
	2–1	172.108	12.38	2.115×10^{-4}	
	3–2	258.157	24.78	7.649×10^{-4}	
	4–3	344.200	41.30	1.880×10^{-3}	

Notes. We use molecular data of HCN and its isotopologues from: 1) Navarro-Almaida et al. (2023), 2) Fuchs et al. (2004), 3) Cazzoli et al. (2005). The data were sourced from the CDMS catalogue (Müller et al. 2001, 2005; Endres et al. 2016), or via private communication with authors.

pointings altogether. This mosaic covers most of the CMZ of NGC 253; further details of these observations are available in Müller-Sánchez et al. (2010).

3. Moment maps and region selection

3.1. Spectral-line extraction

The molecules we focus on in this study are the ^{13}C, ^{15}N, ^{17}O (of CO), and ^{18}O isotopologues of CO, HCN, and HCO$^+$. A full summary of the investigated lines are shown in Tables 1–3. The integrated spectral line intensities from our data cubes were extracted using `CubeLineMoment`[1] (Mangum et al. 2019). `CubeLineMoment` works by extracting integrated intensities for a given list of targeted spectral frequencies by applying a set of spectral and spatial masks (defined by the user). The

[1] https://github.com/keflavich/cube-line-extractor

Table 3. Transitions of HCO$^+$ and its isotopologues used in this work.

Species	Transition	Rest frequency [GHz]	E_u [K]	A_{ul} [s^{-1}]	Ref.
HCO$^+$	1–0	89.188	4.28	4.187×10^{-5}	1, 2, 3, 4
	2–1	178.375	12.84	4.019×10^{-4}	
	3–2	267.558	25.68	1.453×10^{-3}	
	4–3	356.734	42.80	3.572×10^{-3}	
H^{13}CO$^+$	1–0	86.754	4.16	3.853×10^{-5}	1, 2, 5
	2–1	173.507	12.46	3.699×10^{-4}	
	3–2	260.255	24.98	1.337×10^{-3}	
	4–3	346.998	41.63	3.287×10^{-3}	
HC^{18}O$^+$	1–0	85.162	4.09	3.6449×10^{-5}	1, 2, 6
	2–1	170.322	12.26	3.498×10^{-4}	
	3–2	255.479	24.52	1.265×10^{-3}	

Notes. We use molecular data of HCO$^+$and its isotopologues from: 1) Flower (1999), 2) Denis-Alpizar et al. (2020), 3) Lattanzi et al. (2007), 4) Tinti et al. (2007), 5) Gregersen & Evans (2001), 6) Schmid-Burgk et al. (2004). The data were sourced from the LAMDA database (Schöier et al. 2005) and the CDMS catalogue (Müller et al. 2001, 2005; Endres et al. 2016).

`CubeLineMoment` masking process uses a brighter spectral line (typically the main isotopologue line of the same rotational transition), whose velocity structure over the galaxy is most representative of the science target line, which is used as a tracer of the velocity of the inspected gas component. The products of `CubeLineMoment` are moment 0, 1, and 2 maps in the units chosen by the user, masked below a chosen σ threshold (channel-based). Mangum et al. (2019) provides a more detailed overview of this process.

For use in the age approximation fitting (see Sect. 5.1), we also extracted H39α (rest freq: 106.73738 GHz) radio recombination line emission from the ALCHEMI dataset in the six SSC apertures in order to estimate a dust-unobscured ionising photon rate; we elaborate on in this process in Sect. 5. In order to completely image the line, we used the spectra over barycentric velocity ranges $[-200, 750]$ km s^{-1} to fit and measure the line emission. The Brγ line was also extracted from the SINFONI data described, and is consistent with the map shown in Fig. 11 of Rosenberg et al. (2013).

3.2. Region selection

We selected six SSC regions using the aperture size of the beam of the ALCHEMI observations. Given the lower resolution of the ALCHEMI observations (~28 pc) with respect to the continuum observations of Leroy et al. (2018) (~2 pc), we define new SSC regions; see Table 4 for details. These regions were selected and identified because they cover all of the SSC regions defined in Leroy et al. (2018) at the ALCHEMI beam size resolution, with no overlap. Each of these regions contains between 1 and 4 of the SSC regions approximately resolved in Leroy et al. (2018). Due to the fact that our newly defined regions do not correspond to those of Leroy et al. (2018), a new nomenclature is needed. Each region has therefore been designated an SSC* region name, each with a number corresponding to one of the SSCs that it contains.

Within each SSC* region, we obtained the line intensities extracted over a beam-sized aperture of the available J transitions for each isotopologue. In Figs. 1 and 2 we present the velocity-integrated line intensity moment 0 maps from H^{13}CN (1-0) to (4-3) as an example of the lines we imaged (Tables 1–3). The remaining moment maps are shown in Appendix A. In each

Table 4. All the selected NGC 253 positions of the beam-sized SSC* regions described in Sect. 3.2.

SSC Group	RA(ICRS) (00^h47^m)	Dec(ICRS) ($-25°17'$)	Leroy SSCs
SSC-1*	32^s.8108	21″.293	1, 2, 3
SSC-4*	32^s.9178	20″.426	4
SSC-7*	33^s.0147	19″.341	5, 6, 7
SSC-9*	33^s.0970	18″.053	8, 9
SSC-13*	33^s.1927	16″.928	10, 11, 12, 13
SSC-14*	33^s.2971	15″.583	14

Notes. The SSCs defined in Leroy et al. (2018) that are contained within each SSC group have been provided for clarity, using the nomenclature of that paper.

moment 0 map, the SSC* regions listed in Table 4 are shown with the ALCHEMI beam size plotted in the lower left corner in each map. The line intensities in each of these maps are shown in units of K km s^{-1}, and the conversion to brightness temperature units from Jy beam^{-1} was accomplished using the `astropy` Python package (Astropy Collaboration 2022). It must be noted that SSC-9* and SSC-13* tend to show weaker emission in each of our molecules compared to the other regions in the CMZ; this is seen towards the centre of the moment maps shown in Figs. 1 and 2. We also identify an absorption feature at these locations, within certain J lines of certain isotopologues, which particularly affects the weaker emission species such as HC^{15}N, and H^{13}CO$^+$ and affects lower J lines most prominently. This absorption feature, affecting both SSC-9* and SSC-13*, is consistent with the position of the nuclear continuum source designated 'TH2' (Turner & Ho 1985; Müller-Sánchez et al. 2010; Mangum et al. 2019). This latter is a strong continuum source at the dynamical centre of NGC 253 first identified in Turner & Ho (1985) and long thought to possibly contain a low-luminosity AGN (LLAGN); however, it is now believed to be a supernova or supernova remnant source (Mangum et al. 2019). This absorption primarily affects weaker lines, and as such no transitions of HC^{15}N were used for either SSC-9* or SSC-13*. An example of the effect of this absorption upon HC^{15}(1-0) in SSC-13* compared to SSC-1* is shown in Appendix B.

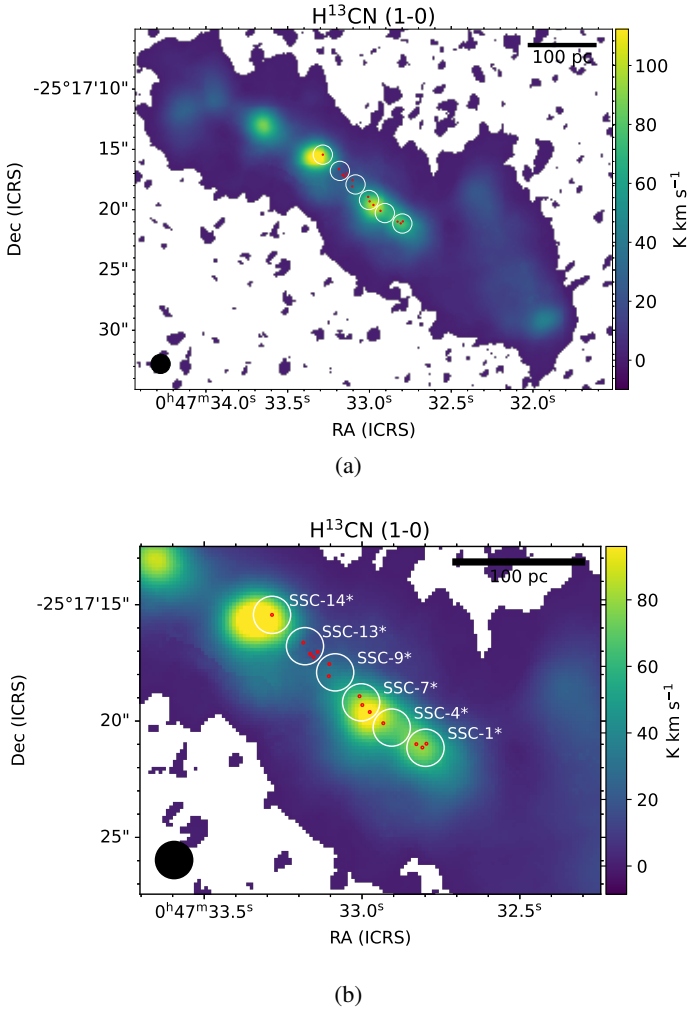

Fig. 1. Velocity-integrated line intensities in units of K km s^{-1} H^{13}CN (1-0). Panel a shows a region covering the entire CMZ of NGC 253 and panel b covers a zoomed-in region of the SSC* regions studied in this paper. The studied SSC regions as listed in Table 4 are labelled in white text on the map. The original SSC locations with appropriate beam sizes from Leroy et al. (2018) are shown by the red regions. The ALCHEMI 1.″6 × 1.″6 beam is displayed in the lower-left corner of the map.

4. Inference of gas properties

4.1. LTE analysis

In order to help with informing the priors of the non-LTE analysis shown in the following Sect. 4.2, we obtained estimates of the molecular column densities assuming LTE. The upper state column density, N_u, of a molecular transition can be approximated as

$$N_u = \frac{8\pi k \nu^2 W}{hc^3 A_{\rm ul}} \left(\frac{1}{\eta_{\rm ff}}\right) \frac{\tau}{1 - e^{-\tau}}, \quad (1)$$

where W is the integrated line intensity, $_u$ signifies the upper level of a rotational transition, $A_{\rm ul}$ is the Einstein A-coefficient, τ is the optical depth, and $\eta_{\rm ff}$ is the beam filling factor. Given the variation between the beam size of this project (1.″6 × 1.″6) and that of Leroy et al. (2018), where these regions were first defined (0.″11 × 0.″11), we accounted for the beam filling factor, $\eta_{\rm ff}$ by defining it as:

$$\eta_{\rm ff} = \frac{\theta_{\rm S}^2}{\theta_{\rm beam}^2 + \theta_{\rm S}^2}, \quad (2)$$

where $\theta_{\rm S}$ and $\theta_{\rm beam}$ are the respective resolutions of the source and the beam. For the purposes of the LTE estimation, $\theta_{\rm S}$ was defined as the size of the regions observed in Leroy et al. (2018). We were then able to use these transition column densities, N_u, to derive the total column density of the emitting molecule, N, using

$$N = \frac{N_u Z(T)}{g_u e^{\frac{E_u}{kT}}}, \quad (3)$$

where $Z(T)$ is the partition function, g_u is the statistical weight of level u, and E_u is the excitation energy of level u. To compute the partition function, we make use of molecular data from the Cologne Database for Molecular Spectroscopy (CDMS; Müller et al. 2005; Endres et al. 2016). We used a combination of Eqs. (1) and (3) following the methodology of Goldsmith & Langer (1999) to compute an estimate of the total column density for each molecule. These total column densities were estimated over a range of temperatures and optical depth. The temperature range was left free up to the maximum

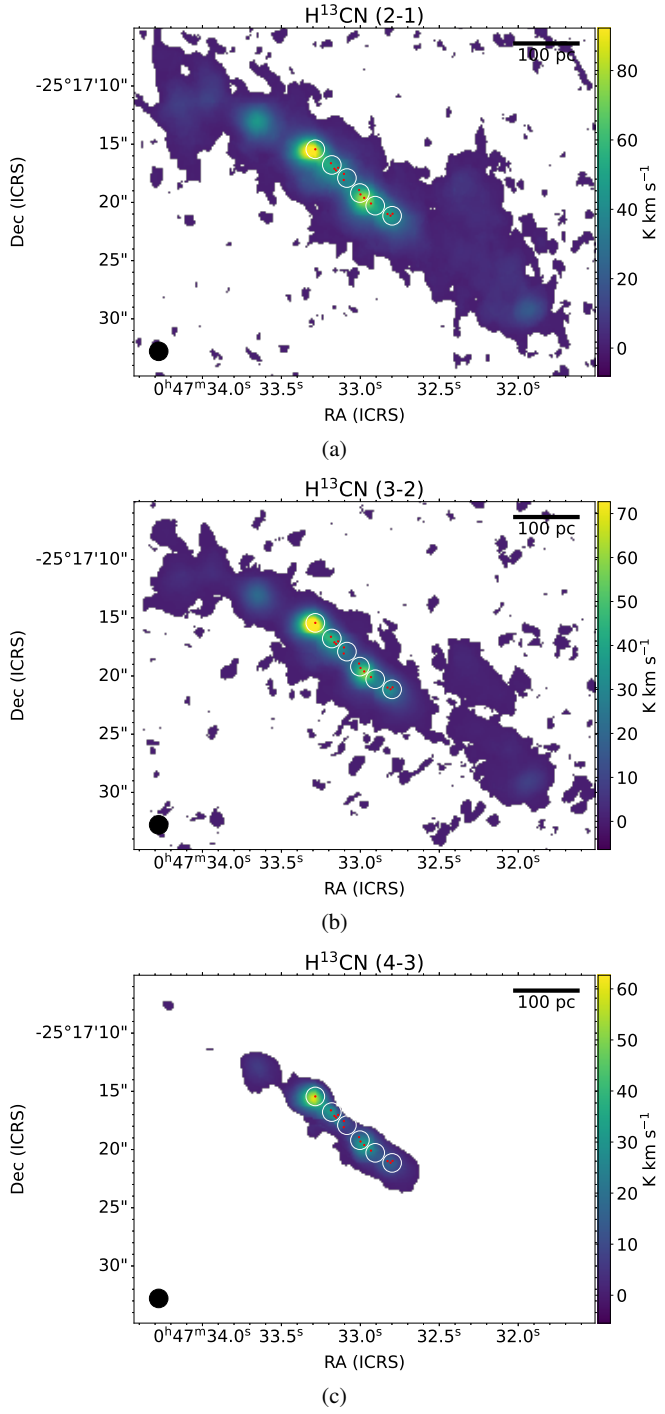

Fig. 2. Velocity-integrated line intensities (moment 0) maps in units of K km s^{-1} for H^{13}CN (2–1), (3–2) and (4–3). All of the maps shown were generated using a signal-to-noise cutoff of 3. The studied SSC regions as listed in Table 4 are labelled in white text on the map. The original SSC locations with appropriate beam sizes are from Leroy et al. (2018). The ALCHEMI 1.″6 × 1.″6 beam is displayed in the lower-left corner of the map.

range chosen to be consistent with the RADEX analysis (shown in Sect. 4.2), with the upper limit being 500 K. We used a range of values for optical depth (τ) from 0 to 10 in increments of 0.1 in the optically thin regime, $\tau < 1$ and 0.5 in the optically thick regime $\tau > 1$. These column densities, shown in Table 5, are now used to define the prior distribution column density ranges

Table 5. Minimum and maximum LTE column densities generated for each species directly from the observed intensities using Eqs. (1) and (3).

Species	$N_{\rm min}$	$N_{\rm max}$
CO	1.8e+18	8.9e+20
^{13}CO	6.1e+17	2.0e+20
C^{17}O	5.3e+15	3.9e+17
C^{18}O	9.1e+16	3.2e+19
HCN	3.1e+15	3.5e+17
H^{13}CN	7.7e+12	4.3e+16
HCO$^+$	1.4e+14	1.8e+17
H^{13}CO$^+$	5.5e+12	9.8e+16
HC^{15}N	8.4e+11	1.0e+15
HC^{18}O$^+$	2.0e+12	8.5e+15

studied during the RADEX modelling in the following section. Thanks to the fact that we have multiple transitions across each region for most of the species (the exceptions being weaker isotopologues (e.g. HC^{15}N and HC^{18}O$^+$) in the regions affected by absorption) the temperature can also be constrained via the use of rotational diagrams. Most species across the regions show a behaviour that can be explained by either multiple temperature components or the optical depth effects upon the higher J lines relatively to low-J. A notable exception to this is HCN, which can consistently be fit with a single temperature component. This analysis drove the initial temperature ranges for each species seen in the non-LTE analysis (see Sect. 4.2).

4.2. Non-LTE RADEX analysis

We use a non-LTE analysis in order to infer the physical characteristics and optical depth (per transition) of each region. We employ the radiative transfer code RADEX (van der Tak et al. 2007). We reference the sources of the collisional data in the subtext of Tables 1–3. In order to determine these physical conditions, we followed a similar methodology, combining SpectralRadex and UltraNest, as Holdship et al. (2021), Behrens et al. (2022), Huang et al. (2022, 2023), with the difference being that in our study each group of isotopologues (e.g. HCN, H^{13}CN, and HC^{15}N) was modelled together for the process. The physical conditions constrained within our modelling are: gas density ($n_{\rm H2}$), gas temperature ($T_{\rm kin}$), the total column density of each isotopologue (i.e. N(HCN), N(H^{13}CN), and N(HC^{15}N)), and the beam filling factor ($\eta_{\rm ff}$). The beam filling factor has been allowed to be a free parameter between 0 and 1, this has been done as the number of lines that we possess allow it to be constrained despite its degeneracy with N and $n_{\rm H}$.

We inferred the gas properties by combining the RADEX modelling with a Bayesian inference process in order to properly sample the parameter space and obtain reliable uncertainties. While collisional data were available for HCO$^+$, HCN, H^{13}CN, HC^{15}N, CO, ^{13}CO, C^{18}O, and C^{17}O, this was not the case for the isotopologues of HCO$^+$. Collisional data for HCO$^+$ were therefore used for its respective isotopologues, as recommended by the LAMDA database (van der Tak et al. 2020) (see Table 3). In order to test the validity of this assumption, RADEX models were computed under the same physical parameters as the different isotopologues of CO, of which the collisional data is available for all four isotopologues, and the results were then compared. These models were found to be consistently similar and therefore

Table 6. Parameter space allowed as a prior for the nested sampling of the CO isotopologue RADEX models.

Variable	Range	Distribution type
Gas density, n_{H2} [cm−3]	10^3–10^7	log-uniform
Gas temperature, T_{kin} [K]	40–500	Uniform
N(CO) [cm^{-2}]	10^{18}–10^{21}	log-uniform
N(^{13}CO) [cm^{-2}]	10^{17}–10^{20}	log-uniform
N(C^{18}O) [cm^{-2}]	10^{15}–10^{19}	log-uniform
N(C^{17}O) [cm^{-2}]	10^{16}–10^{19}	log-uniform
Beam filling factor, η_{ff}	0.0–1.0	Uniform

Table 7. Parameter space allowed as a prior for the nested sampling of the HCN isotopologue RADEX models.

Variable	Range	Distribution type
Gas density, n_{H2} [cm^{-3}]	10^3–10^7	log-uniform
Gas temperature, T_{kin} [K]	40–500	Uniform
N(HCN) [cm^{-2}]	10^{14}–10^{18}	log-uniform
N(H^{13}CN) [cm^{-2}]	10^{12}–10^{16}	log-uniform
N(HC^{15}N) [cm^{-2}]	10^{11}–10^{15}	log-uniform
Beam filling factor, η_{ff}	0.0–1.0	Uniform

Table 8. Parameter space allowed as a prior for the nested sampling of the HCO$^+$ isotopologue RADEX models.

Variable	Range	Distribution type
Gas density, n_{H2} [cm^{-3}]	10^3–10^7	log-uniform
Gas temperature, T_{kin} [K]	40–500	Uniform
N(HCO$^+$) [cm^{-2}]	10^{14}–10^{18}	log-uniform
N(H^{13}CO$^+$) [cm^{-2}]	10^{12}–10^{17}	log-uniform
N(HC^{18}O$^+$) [cm^{-2}]	10^{12}–10^{16}	log-uniform
Beam filling factor, η_{ff}	0.0–1.0	Uniform

the assumption we make regarding the isotopologues of HCO$^+$ is valid.

The posterior probability distributions are derived with the nested sampling Monte Carlo algorithm MLFriends (Buchner 2016, 2019), which was integrated into our analysis via the Python package UltraNest[2] (Buchner 2021). Similarly to the approach adopted by Huang et al. (2022, 2023), for each modelling run we assume the prior distributions of our parameters to be uniform or log-uniform, where the column density priors are based on the N_u results obtained during the LTE analysis (see Sect. 4.1; these are given for each species group in Tables 6–8). We assume that the uncertainty on our measured intensities is Gaussian so that our likelihood is given by $P(\theta|d) \sim \exp(-\frac{1}{2}\chi^2)$, where χ^2 is the chi-squared statistic between our measured intensities and the RADEX output for a set of physical parameters θ (summarised earlier).

This analysis provides an indication of the mean gas properties of our SSC* regions, under the assumption that all of the fitted transitions in each group arise from the same gas component. The results presented here therefore provide more of a general idea of the mean properties of the gas present in each SSC* region as predicted by each molecule and its isotopologues. Along with the physical parameters described, this RADEX fitting also provides us with an indication of the optical depths, τ, of the fitted lines for each region.

Appendix C contains the posterior distributions of the sampling for the CO, HCN, and HCO$^+$ isotopologues toward each of the SSC* regions. A summary of the results of the Ultranest RADEX model fitting can be found in Tables D.1–D.3. As can be seen from the posterior distributions, the majority of the parameters are constrained for each isotopologue group sampling thanks to the large number of lines available in the ALCHEMI survey. However, the kinetic temperature, T_K, remains largely unconstrained, regardless of the region or isotopologue group. As already suggested by the LTE analysis, this may be (at least partly) due to the fact that there are multiple temperature components of the gas: a cold one being traced by the lower J transitions and another hot one traced by higher J transitions. Another contributing factor is that the transitions observed have an excitation temperature of $<\sim$40 K, and as we are probing a temperature regime of >100 K (see Mangum et al. 2019) in these regions, these lines are not suited to constrain T_K.

As one would expect, the HCN and HCO$^+$ isotopologues trace denser regions of the gas ($\log(n_H) > 4.3$) compared to the CO isotopologues ($\log(n_H) \lesssim 3.5$). Also, as may be expected, CO isotopologues appear to be tracing more extended regions of the gas as shown by the larger beam filling factors, η_{ff} ($\sim$0.3, $\sim$5 pc), compared to those of the HCN and HCO$^+$ isotopologues ($\lesssim$0.1, $\lesssim$2 pc, with the exception of the two regions affected by absorption for HCN). These lower values of η_{ff} correspond to the scale of the constituent SSCs – as defined by Leroy et al. (2018) (2–3 pc) – located within each beam, which reassures us that the emission we are tracing and modelling is sourced from the SSCs observed rather than the larger-scale GMCs defined in NGC 253 (Martín et al. 2021; Huang et al. 2023).

A particular region of note for HCN and HCO$^+$ and their isotopologues is SSC-14* as it shows significantly higher-intensity emission than the other regions. This can be associated with the increased predicted column density of each of these molecules by $\leq$0.5 dex for some isotopologues, compared to the next most abundant region. These high column densities approach the parameter space under which RADEX struggles to converge as a result of line saturation at high opacities, particularly for HCO$^+$ ($N_{HCO^+} > 10^{17}$ cm^{-2}).

The predicted column densities of both HCO$^+$ and its corresponding ^{13}C isotopologue are shown to be consistently higher than their corresponding HCN species counterparts. This enhancement is nearly of an order of magnitude for two of the regions (SSC-1* and SSC-14*). This supports the conclusion made in previous studies that HCO$^+$ and its isotopologues are relatively more abundant than HCN in other actively star forming regions, such as AGN-dominated regions (Krips et al. 2008; Izumi et al. 2016; Butterworth et al. 2022).

Moreover, we obtained the optical depth conditions of each investigated species and its respective transitions for each SSC* region. These results are shown in Appendix F. We observe that the majority of non-main isotopologues are indeed optically thin ($\tau < 1$) for the majority of our SSC* regions, with a couple of notable exceptions. Specifically, ^{13}CO, H^{13}CO$^+$, and HC^{18}O$^+$ have multiple lines across the different regions that are optically thick, primarily driven by the significant column densities that we observe for these species. The optical depth for each species is also predicted to be lower for the J = 1–0 transitions than for the J = 2–1 transitions ($\tau_{10} < \tau_{21}$). The physical reason for this occurrence can be explained by the dependence of τ on the

[2] https://johannesbuchner.github.io/UltraNest/

N_u and B_{ul} parameters (see Eq. (6), Goldsmith & Langer 1999), where B_{ul} is the Einstein coefficient for induced emission. In the case of the lines studied here, the increase in B_{ul} with increasing transitions is larger than the decrease in N_u, which results in increasing optical depth with transition level.

5. Isotopic ratios and their relationship to SSC ages

5.1. SSC age determination

As isotopes are generated and supplied to the ISM over varying timescales depending on the evolutionary stages of intermediate-mass or more massive stars, by examining and comparing how these ages correlate (or not) to abundance ratios, we can more reliably test the hypothesis that factors such as the IMF are the primary driving forces of the observed isotopic ratios (Romano et al. 2017). In order to determine ages for each SSC* region, we used the stellar population modelling software `Starburst99` to examine how the equivalent width of the Brγ, EW(Brγ), and the ionising photon rate estimated from the H39α line evolve with the age of the star-forming region (Leitherer et al. 1999, 2014). How the ionising photon rate is derived is summarised in Appendix E. Ionising photon rate and EW(Brγ) are both inversely proportional to the age of a high star-forming region, such as an SSC, as they are primarily driven by the presence of the most massive stars. `Starburst99` operates by populating a main sequence of stars under specified initial conditions and allowing the evolution of these populations to occur over a user-defined timescale (in this study, 10^4–10^9 yr). The evolution of these populations afffects observable properties, such as ionising photon rate and EW(Brγ), in various ways as a result of how their constituent stars progress along their evolutionary track. The IMF and the upper mass boundary of the formed stars can be specified in `Starburst99` (S99). New stars can be formed in this model in two ways: either all of the population can be created initially (known as instantaneous formation) or stars can be created continuously over the entire period of the model at intermittent time steps; these models are referred to here as Instantaneous and Continuous, respectively.

S99 allows for various input parameters, but those most relevant to this study are the IMF power law, the stellar mass cutoff, and formation type. Before we can obtain ages for the SSC* regions, we have to identify the combination of parameters that reliably reproduces the observed conditions in these regions. To this end, we fitted the ionising photon rates of H39α and the equivalent width of Brγ, as both are available outputs of S99. The range of initial conditions can be found in Table 9. The different formation types (Instantaneous and Continuous) determine whether S99 is entirely populated with stars initially or if there is a constant rate of new stars formed, respectively. The masses used as a part of these models were taken from a previous study of the SSCs in NGC 253 ($\sim 10^5\ M_\odot$, Leroy et al. 2018). We find that, when setting appropriate masses to be achieved of $10^5\ M_\odot$, the Continuous models are not able to reproduce the observed values of Brγ EW or the ionising photon rate over the entire time range and were therefore discarded in favour of Instantaneous models. The remaining parameters of both IMF and star mass boundary were then fit using the ionising rate and EW(Brγ). The IMF power-law values were chosen to represent typical IMF scenarios; values of 1.5, 2.35, and 3.3 were chosen, which represent top-heavy, a typical Salpeter IMF, and a bottom-heavy scenario, respectively (Salpeter 1955).

We extracted H39α radio recombination line emission from the ALCHEMI dataset in the six SSC* apertures in order to estimate an ionising photon rate free of dust obscuration. In all SSCs*, a component consistent with He39α was also present that has a velocity offset from H39α of $-122.15\ \mathrm{km\,s^{-1}}$. In SSC-1*, 4*, 7*, and 14*, we fit one Gaussian component to hydrogen and one Gaussian component to helium. In SSCs-9* and 13*, we fit two Gaussian components to the two observed velocity components of hydrogen and one Gaussian component to helium. The spectra, shown with fitting, for each region are supplied in Appendix E. We use the total hydrogen H39α integrated emission – summed over two components where applicable – to estimate the ionising photon rate, as described in Emig et al. (2020) and briefly in Appendix E.

The equivalent width of the Brγ line was obtained by measuring the line emission over the SSC* apertures using the Brγ image from Rosenberg et al. (2013). The equivalent width was obtained using this line emission in combination with the K continuum.

A top-heavy IMF power law of 1.5 and an upper stellar mass cutoff of 150 $M_\odot$ with instantaneous star formation was shown to provide the best fit to both the H39α and Brγ data. We used this fit to obtain ages for each of the SSC* regions as predicted by `Starburst99`. We find an average best fit for the age of the order of 10^6 yr, which implies that nucleosynthesis effects are unlikely to lead to isotopic differentiation across the SSC regions because of their young ages – which are on the order of 10^6 yr – relative to the necessary timescales required for the production of the isotopes ($\sim 10^8$ yr, Milam et al. 2005). For example, ^{13}C is primarily produced from ^{12}C during the CNO cycle of intermediate-mass stars (1.5–6 $M_\odot$) and is ejected during their AGB phase (Clayton 2003). Similarly, ^{15}N can be produced and supplied to the ISM via nova explosions; this can lead to variations in the ^{14}N/^{15}N across the galactic disc, but 10^9 yr are typically required for a sufficiently significant nova to occur (Romano et al. 2017, 2019; Colzi et al. 2022). We investigate the relationship between the SSCs* ages and isotopic ratios in the following section in order to decipher whether or not a correlation indeed exists.

Table 9. Investigated initial parameters of `Starburst99`.

Variable	Range
Formation type	Instantaneous, Continuous
IMF (power law)	1.5, 2.35, 3.3
Star mass boundary [$M_\odot$]	100, 150, 250

5.2. SSC age versus isotopic ratio

From the derived column densities, we have the possibility to investigate whether there is a correlation between the age of each star-forming region and the isotopic ratio. Table 10 contains the ranges and means of the isotopologue column ratios produced from the `RADEX` modelling. Here, we summarise the primary isotopic ratios investigated in this study and how their predicted column densities correlate to the modelled ages of each region. The plots for the column densities ratios versus the predicted ages are shown for each isotopologue ratio, but the line intensity ratio versus age are only shown for the J(1–0) transition of ^{12}CO/^{13}CO. The `RADEX` column density predictions give the abundance of a molecule and `RADEX` takes into account the optical depth effects; as such, these predictions typically give a more reliable result than individual line intensity ratios. For optically thin LTE gas, both results should be comparable. Given the low sample size

Table 10. Ranges and means of the isotopologue column density ratios from across all the SSC* regions.

Ratio	$X_{\rm Ratio}$	$\bar{X}_{\rm Ratio}$
CO/^{13}CO	26.7–35.9	28.3
HCO$^+$/H^{13}CO$^+$	36.3–89.9	58.1
HCN/H^{13}CN	11.1–22.4	15.4
HCO$^+$/HC^{18}O$^+$	144.6–409.6	262.7
CO/C^{18}O	100.0–145.1	106.6
HCN/HC^{15}N	75.7–183.4	128.4
CO/C^{17}O	778.8–1147.0	847.2

of four to six regions (depending on the ratio), we cannot provide robust statistics for any possible correlation between age and column density ratio. Instead, we simply provide a qualitative assessment of each ratio versus age plot.

5.2.1. ^{12}C/^{13}C

Figure 3 shows the intensity and column density ratios of ^{12}CO/^{13}CO. The column density ratio in particular shows no correlation to the predicted ages of each region. This may be because these regions are too young ($\ll 10^8$ yr) for a meaningful effect to be observed as a result of nucleosynthesis from all but the most massive stars. There is also no correlation between the spatial location of these regions and their column density ratios. The regions away from the TH2 region do show lower ^{12}C(1–0)/^{13}C(1–0) intensities ratios, but all differences fall within the error bars.

Figure 4 shows the column density ratio of the H^{12}CO$^+$/H^{13}CO$^+$ ratio (range, ~36–90) versus age. This column density ratio does indeed show a negative correlation with the age of the SSC regions studied, with the exception of SSC*-9 and SSC*-13. However, we note that SSC*-13 is the region most affected by the absorption source observed near the dynamical centre of NGC 253, as discussed above. If we disregard these regions, the remaining regions imply that there are some processes other than nucleosynthesis that can affect this ratio within a relevant timescale. Indeed, Roueff et al. (2015) found that H^{12}CO$^+$/H^{13}CO$^+$ experiences a turbulent variation due to fractionation processes until ~10^6 yr, which is of the same order as the observed ages of these regions (Sipilä et al. 2023). Fractionation processes as an explanation is a tentative hypothesis however, as we have only a few observed regions over a relatively small timescale, and we assume that SSC-13* is significantly affected by absorption features.

If fractionation processes are indeed responsible for the trend seen in H^{12}CO$^+$/H^{13}CO$^+$ then it is possible that ISM fractionation processes have already approached an equilibrium with regards to the ^{12}CO/^{13}CO ratio within the time frame covered by our regions. Indeed this would be consistent with the chemical models of Roueff et al. (2015), who found that the ^{12}CO/^{13}CO ratio approaches equilibrium swiftly and with less variation than H^{12}CO$^+$/H^{13}CO$^+$.

Similarly to the ^{12}CO/^{13}CO ratio, the H^{12}CN/H^{13}CN ratio shown in Fig. 5 shows little correlation with age, though the ratio shows significantly more variation between the regions than its CO counterpart. The H^{12}CN/H^{13}CN ratio has been predicted to undergo a similarly turbulent variation to H^{12}CO$^+$/H^{13}CO$^+$ on timescales approaching those observed across these SSC* regions this may explain the significant variation that we observe (Roueff et al. 2015; Sipilä et al. 2023).

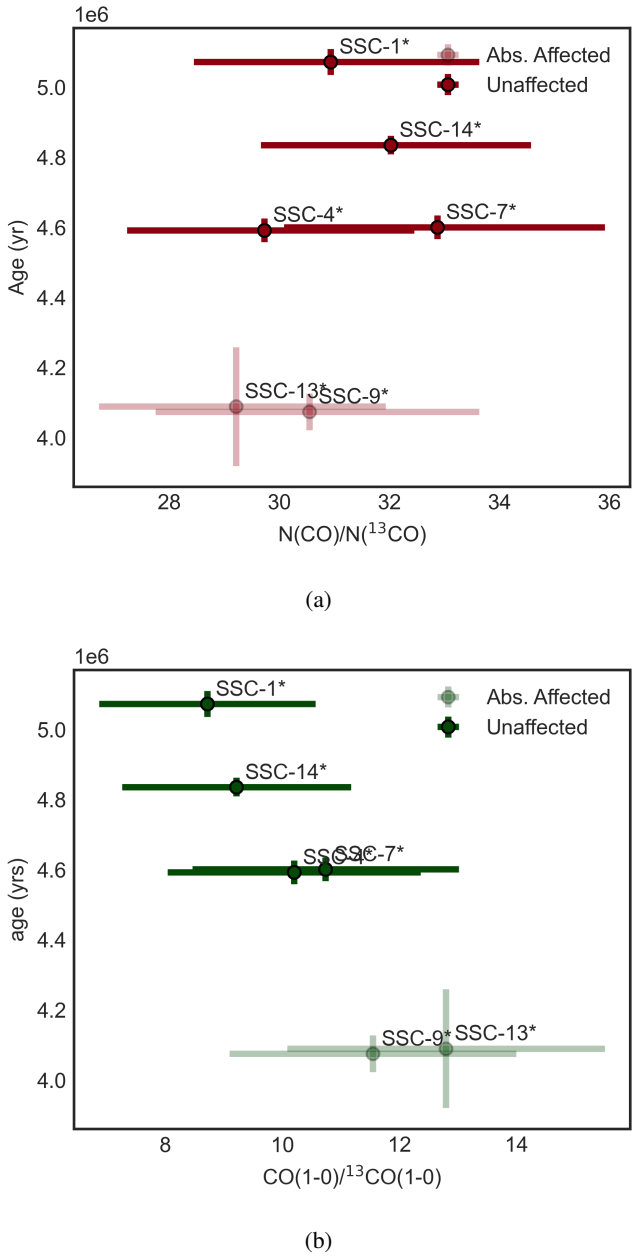

Fig. 3. The ratios of both intensity of column density are shown. The ^{12}CO/^{13}CO column density ratio derived from `RADEX` is shown in (a) while the line intensity ratio ^{12}CO/^{13}CO for the J = 1–0 transition from the ALCHEMI observations is shown in (b). The regions unaffected by the absorption effects observed near GMC-5 in NGC 253 are shown in full colour, whereas those regions that are affected are shaded.

H^{13}CO$^+$ and H^{13}CN are the ^{13}C-bearing isotopologues of the dense gas tracers HCN and HCO$^+$. These isotopologues are optically thin, unlike their ^{12}C counterparts. We observe an interesting relation in the column density ratio of these isotopologues. As shown in Fig. 6, once we disregard the absorption-affected regions of SSC-9* and SSC-13* (for the reasons stated above; the equivalent plot including the absorption-affected region can be seen in Appendix B), there appears to be a positive relation between age and this ratio. This is in contrast to the equivalent ratio of HCO$^+$/HCN shown in Fig. 7, for which no correlation with age can be seen. This result perhaps supports the fractionation hypothesis for the correlation seen in H^{12}CO$^+$/H^{13}CO$^+$, and

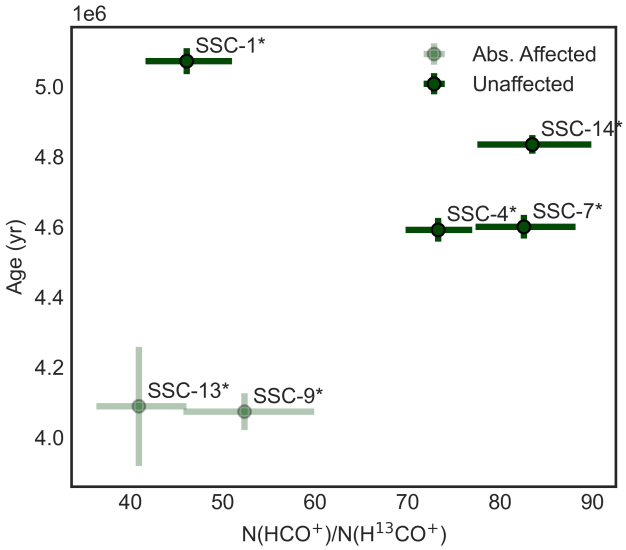

Fig. 4. $H^{12}CO^+/H^{13}CO^+$ column density ratio derived from RADEX. The regions unaffected by the absorption effects observed near GMC-5 in NGC 253 are shown in full colour, whereas those regions that are effected are shaded.

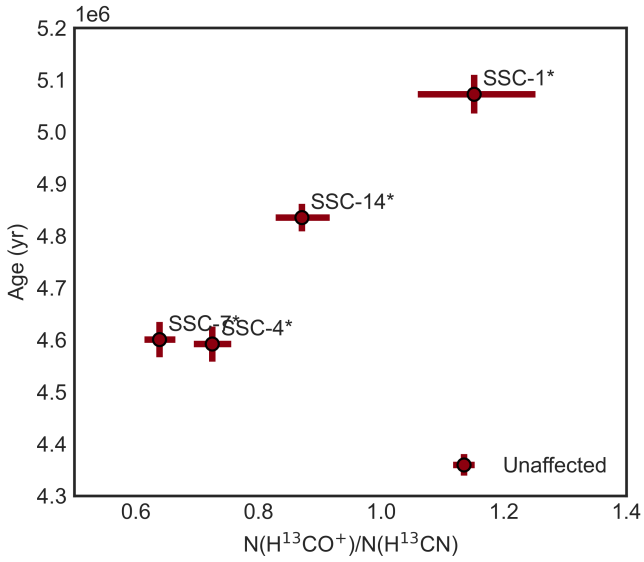

Fig. 6. $H^{13}CO^+/H^{13}CN$ column density ratio derived from RADEX. Due to the significant effect of the absorption on this ratio, only the unaffected regions are displayed here. An equivalent plot including the absorption-affected regions is shown in Appendix B.

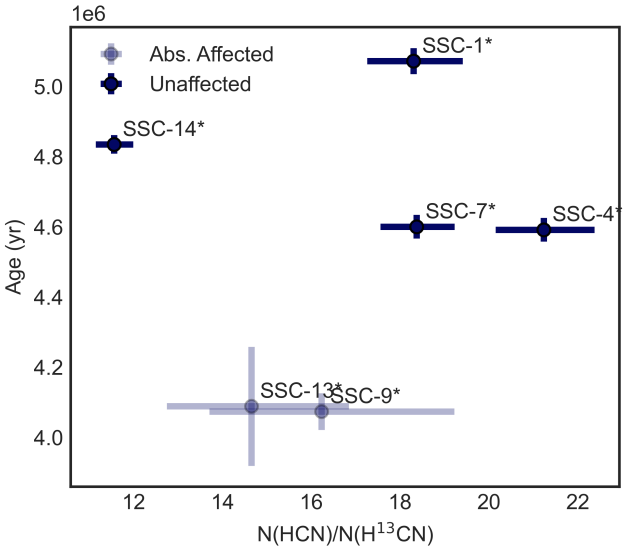

Fig. 5. $H^{12}CN/H^{13}CN$ column density ratio derived from RADEX. The regions unaffected by the absorption effects observed near GMC-5 in NGC 253 are shown in full colour, whereas those regions that are effected are shaded.

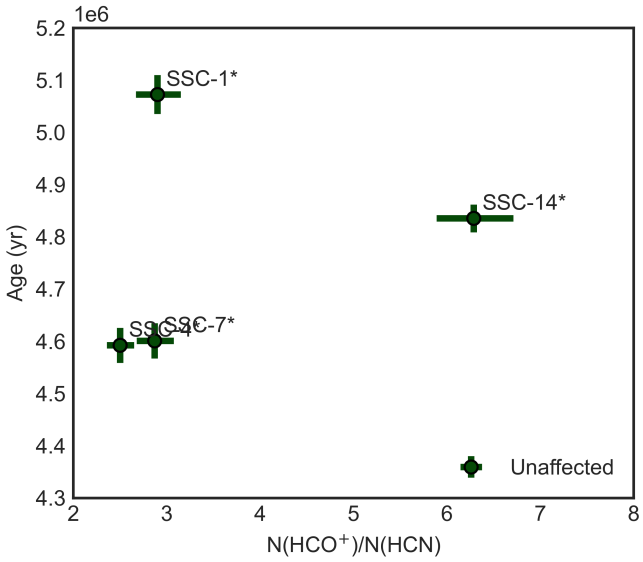

Fig. 7. HCO^+/HCN column density ratio derived from RADEX. Due to the significant effect of the absorption on this ratio, only the unaffected regions are displayed here. An equivalent plot including the absorption-affected regions is shown in Appendix B

therefore this ratio may also be a useful tool as a tracer of the age of SSC regions in the future.

Martín et al. (2019) observed isotope ratios using spatially resolved optically thin isotopologues of CO in NGC 253. These authors observed $^{12}C/^{13}C \sim 21 \pm 6$ using $C^{18}O$ and $^{13}C^{18}O$. In comparison, we observed a larger ratio than this when viewed with $CO/^{13}CO$ (~27–36) and $HCO^+/H^{13}CO^+$ (~36–80) in our SSC* regions. A smaller ratio is observed with $HCN/H^{13}CN$ (~11–22), this range of values is consistent with the observations of Meier et al. (2015), who observed $HCN/H^{13}CN$ at 2″ scale with a range of 10–20. Meier et al. (2015) also observed $HCO^+/H^{13}CO^+$ at this scale and found a range of 10–20. Martín et al. (2021) observed these isotopologue ratios as well, but at 15″ (~255 pc) resolution. These authors observed values for $CO/^{13}CO$ of 13.3 ± 1.4, for $HCN/H^{13}CN$ of 26.1 ± 1.3, and for $HCO^+/H^{13}CO^+$ of 21.2 ± 1.5. It should be noted that the assumed source size was 10″ (~170 pc) for the CO ratio and 5″ for the HCN and HCO^+ ratios. Therefore, the resolution and the region in which these ratios are observed significantly affect the result. Tang et al. (2019) observed CN and ^{13}CN at a resolution of 3.6″ × 1.7″ (~68 × 32 pc) in NGC 253 and observed an average $^{12}C/^{13}C$ ratio of 41.6 ± 0.2.

There have been no similar studies observing regions of intense star formation, like SSCs, at a comparable resolution in nearby galaxies, and therefore a comparison to observations of the $^{12}C/^{13}C$ ratio would not be appropriate. The $^{12}C/^{13}C$ ratio has been observed over many galactic regions. Yan et al. (2023) provides an overview (see Table 7 of that paper) of the $^{12}C/^{13}C$ ratios

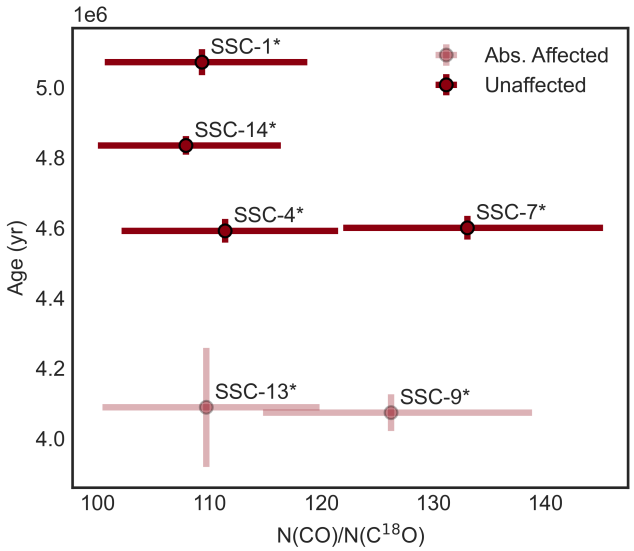

Fig. 8. $C^{16}O/C^{18}O$ column density ratio derived from RADEX. The regions unaffected by the absorption effects observed near GMC-5 in NGC 253 are shown in full colour, whereas those regions that are effected are shaded.

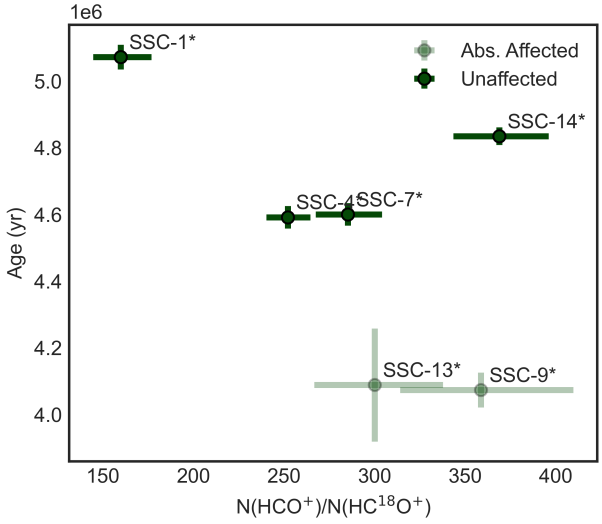

Fig. 9. $HC^{16}O^+/HC^{18}O^+$ column density ratio derived from RADEX. The regions unaffected by the absorption effects observed near GMC-5 in NGC 253 are shown in full colour, whereas those regions that are effected are shaded.

observed across different regions of the Milky Way. On average, $^{12}C/^{13}C$ varies between ~25 ± 2 in the CMZ and ~69 ± 12 in the outer Galaxy (Henkel et al. 1985; Langer & Penzias 1990, 1993; Wouterloot & Brand 1996; Keene et al. 1998; Savage et al. 2002; Milam et al. 2005; Yan et al. 2019, 2023).

In summary, the $^{12}C/^{13}C$ column density ratio from our RADEX modelling shows little correlation with the ages of these star-forming regions. A possible exception is the $H^{12}CO^+/H^{13}CO^+$ ratio. The correlation between this ratio and age could be a result of chemical fractionation affecting this ratio on the observed timescales (rather than nucleosynthesis). The lack of correlation observed for the $^{12}C/^{13}C$ column density ratio supports the conclusion of Romano et al. (2017) that the IMF is a primary driving factor in the isotopic ratio observed in star-forming regions. Though it must be noted that this may only be the case for the age range covered by these SSCs.

5.2.2. $^{16}O/^{18}O$

Figures 8 and 9 show the column density ratio of the $C^{16}O/C^{18}O$ and $HC^{16}O^+/HC^{18}O^+$ ratio, respectively. $C^{16}O/C^{18}O$ clearly shows no correlation between age and column density ratio. The $HC^{16}O^+/HC^{18}O^+$ ratio generally does not show a clear trend, though the oldest predicted region, SSC-1*, does show a significantly smaller ratio than the others. To explore whether or not this is a trend would require an investigation into more regions and a larger range of timescales. When compared to previous observations of $^{16}O/^{18}O$, $CO/C^{18}O$ (~100−145) is largely consistent with those derived at 3″ (~51 pc) resolution in NGC 253 by Martín et al. (2019) using $^{13}CO/^{13}C^{18}O$ (130 ± 40). However, our results for the ratio of $HCO^+/HC^{18}O^+$ are significantly higher (140−410). Martín et al. (2021) provides ALMA Compact Array observations of $^{16}O/^{18}O$ ratios in NGC 253 at 25″ (~255 pc) resolution calculated from $CO/C^{18}O$ (48 ± 5), $^{13}CO/^{13}C^{18}O$ (520±60), and $HCO^+/HC^{18}O^+$ (100±20). Aladro et al. (2015) observed the $HCO^+/HC^{18}O^+$ at an even lower resolution of 28″, finding a value of 69 ± 2.

As is the case for $^{12}C/^{13}C$, an appropriate comparison study in nearby galaxies has not yet been completed. However, $^{16}O/^{18}O$ ratios have been observed across different regions of the Milky Way. As viewed with H_2CO and its respective ^{18}O isotopologue, the $^{16}O/^{18}O$ varies from ~263 ± 45 in the CMZ to ~625 ± 144 in the outer Galaxy (Gardner & Whiteoak 1981; Wilson & Rood 1994; Yan et al. 2023).

The variations across all these observations and resulting ratios within the same galaxy show that resolution and the regions being traced play a key role in determining the observed isotope ratios. As stated above, the influence of nucleosynthesis on these ratios can most likely be discarded given the young ages of the regions studied.

5.2.3. $^{16}O/^{17}O$

The column density ratio of $C^{16}O/C^{17}O$ is shown in Fig. 10. This ratio is largely unaffected by the SSC* age, similar to what is observed in the other ratios. As opposed to ^{18}O, ^{17}O can be produced during nucleosynthesis in the hydrogen burning of less massive stars, and so its enrichment in the ISM would likely be observed at even larger timescales than those expected for ^{18}O. From the limited sample of this study, and on the timescale probed by these regions, this ratio appears to be independent of the age of these SSCs. This ratio was observed for NGC 253 by Martín et al. (2021) at an observed source size of 10″ and found to be 400 ± 40, which is significantly lower than the value we observe in these SSC* regions of ~780−1150.

Again, due to a lack of an appropriate comparison study in nearby galaxies, we instead supply a comparison to Galactic observations. $^{16}O/^{17}O$ ratios have been observed across different regions of the Milky Way. As viewed with H_2CO and its respective ^{17}O isotopologue, the $^{16}O/^{17}O$ ratio varies from ~894 ± 155 in the CMZ up to ~3000 ± 786 in the outer Galaxy according to Yan et al. (2023) using data from (Gardner & Whiteoak 1981; Wilson & Rood 1994; Zhang et al. 2020).

5.2.4. $^{14}N/^{15}N$

Figure 11 shows the column density ratio of the $HC^{14}N/HC^{15}N$ ratio. The analysis of this ratio is greatly affected by the necessity

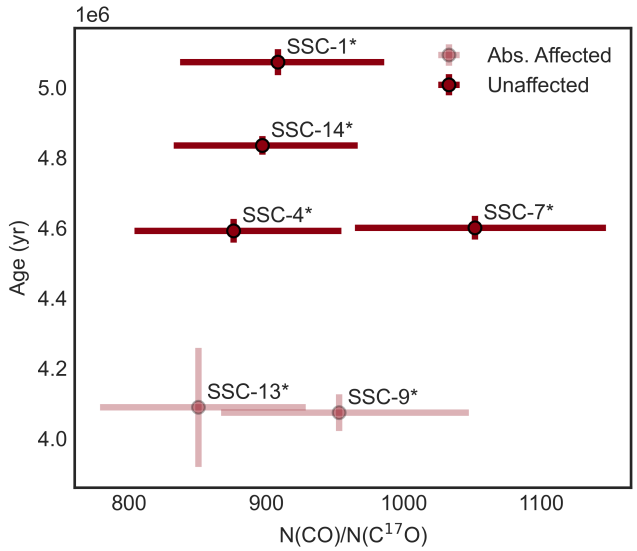

Fig. 10. $C^{16}O/C^{17}O$ column density ratio derived from RADEX. The regions unaffected by the absorption effects observed near GMC-5 in NGC 253 are shown in full colour, whereas those regions that are effected are shaded.

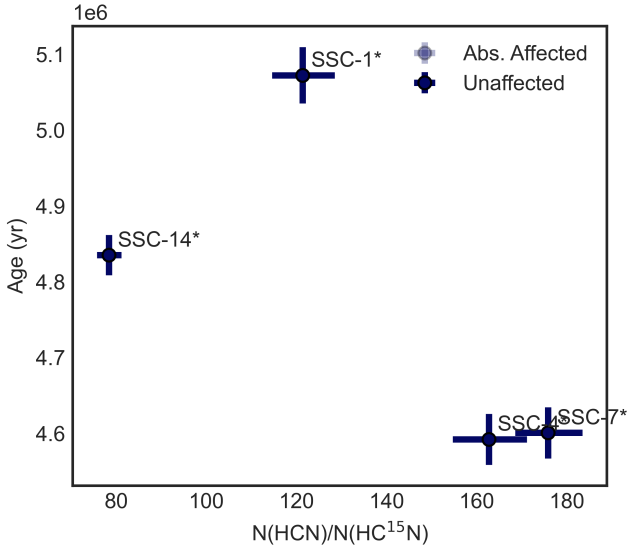

Fig. 11. The column density ratio produced from RADEX of the ratio $HC^{14}N/HC^{15}N$.

to discount the two regions, SSC*-9 and SSC*-13, where absorption effects become noticeable in the $HC^{15}N$ line profile. However, from the four remaining regions, we again find no sign of a correlation between age and the column density ratio. An interesting distinction is that the two regions located closest to the edge of the CMZ (SSC*-1 and SSC*-14) both have significantly lower $HC^{14}N/HC^{15}N$ ratios than their more central counterparts (SSC*-4 and SSC*-7). Nevertheless, without observing more regions, we cannot draw any conclusions from this. Galactic observations of $^{14}N/^{15}N$ have been carried out in previous studies, including with $HC^{14}N/HC^{15}N$, as was observed in the present study. The values of $^{14}N/^{15}N$ viewed across the Milky Way, when observed with $HC^{14}N/HC^{15}N$, range from 284 ± 63 within the inner Galactic disc up to 388 ± 32 in the outer Galaxy (Adande & Ziurys 2012; Colzi et al. 2018).

5.2.5. Isotopic ratios and ISM fractionation

Table 10 lists the observed ranges of isotopic ratios for the various species. Focusing initially on $^{12}C/^{13}C$, Viti et al. (2020) conducted a theoretical chemical modelling study of carbon fractionation in different physical conditions that may represent different types of galaxies. Taking the most suitable model from this study, representing starburst galaxies (see Fig. 10 in Viti et al. 2020), $H^{12}CN/H^{13}CN$ is predicted (~70) to be higher than what we observe (~11–22). The models agree relatively well for the younger regions with regards to $H^{12}CO^+/H^{13}CO^+$ (~55). $^{12}CO/^{13}CO$ is also relatively well predicted by these models (~30) relative to our observations (~26–~36).

Viti et al. (2019) completed a similar study on nitrogen fractionation. These authors found that, depending on the physical parameters, the resulting $HC^{14}N/HC^{15}N$ abundance ratio could vary from ~10 to ~1000. The most elevated ratios (~1000) were found where fractionation processes were suppressed; these were typically for cases of relatively low density $n_H \sim 10^4$ cm^{-3} and high cosmic-ray ionisation rate, visual extinction, or radiation field. The significantly lower range of $HC^{14}N/HC^{15}N$ seen in this study (~75–180) as well as the higher densities predicted by the non-LTE results ($n_H > 10^5$ cm^{-3}) would imply that fractionation processes are occurring within these regions.

6. Conclusions

Using the plethora of data made available to us by the ALCHEMI collaboration, we made use of lines from ten isotopologues of CO, HCN, and HCO^+ in order to investigate the possibility of a correlation between the age of star-forming regions in NGC 253 and the observed isotopic ratios. Our findings are summarised below:

- Our RADEX results suggest that HCN and its isotopologues trace a slightly denser component of the gas ($n_H > 10^5$ cm^{-3}) than HCO^+ and its isotopologues.
- HCO^+ and its isotopologues have larger column densities than their HCN counterparts. This is consistent with previous studies that found HCO^+ to be more abundant than HCN in regions of high star formation. CO and its isotopologues, as one might expect, trace a more diffuse and extended component of the gas in these regions, as shown by their lower densities ($n_H < 10^4$ cm^{-3}).
- Our results regarding the $^{12}CO/^{13}CO$ and $H^{12}CN/H^{13}CN$ seem to discount a clear relation between the age of a star forming region and the isotopic ratio $^{12}C/^{13}C$.
- $H^{12}CO^+/H^{13}CO^+$ may show a tentative negative correlation, but only when assuming that the results for SSC*-13 are greatly perturbed by the absorption feature. In order to verify this trend, a follow-up study of these regions at higher resolution is needed in order to differentiate the individual SSCs in HCO^+ and its isotopologues. This would allow a more complete understanding of the possible fractionation occurring in these regions.
- The $^{16}O/^{18}O$ ratios generally show little correlation with age, with the exception of the oldest region (SSC*-1), which appears to have a significantly lower $HC^{16}O^+/HC^{18}O^+$ ratio than the younger regions.
- The ratios $HC^{14}N/HC^{15}N$ and $HC^{16}O^+$ and $HC^{17}O^+$ also show no correlation with the age of the SSCs.
- The ratios observed in this study generally support the conclusion that age has a minor effect on isotopic ratios, at least over the limited age range observed in these regions,

which supports the hypothesis that the IMF is a primary driving factor of the observed isotopic ratios in these regions (Romano et al. 2017); however, we cannot rule out the possibility that fractionation effects are another primary driver. Future studies observing the SSC regions in NGC 253 at higher spatial resolution or perhaps a multi-object study observing a wider range of star-forming regions spanning a larger range of ages would allow more robust conclusions regarding the use of C, N, or O isotopic ratios.

Acknowledgements. J.B., S.V., K.Y.H., and M.B. have received funding from the European Research Council (ERC) under the European Union's Horizon 2020 research and innovation programme MOPPEX 833460. This paper makes use of the following ALMA data: ADS/JAO.ALMA#2017.1.00161.L and ADS/JAO.ALMA#2018.1.00162.S. ALMA is a partnership of ESO (representing its member states), NSF (USA) and NINS (Japan), together with NRC (Canada), MOST and ASIAA (Taiwan), and KASI (Republic of Korea), in cooperation with the Republic of Chile. The Joint ALMA Observatory is operated by ESO, AUI/NRAO and NAOJ. V.M.R. has received support from the project RYC2020-029387-I funded by MCIN/AEI /10.13039/501100011033, and from the Consejo Superior de Investigaciones Científicas (CSIC) and the Centro de Astrobiología (CAB) through the project 20225AT015 (Proyectos intramurales especiales del CSIC). L.C. acknowledges financial support through the Spanish grant PID2019-105552RB-C41 funded by MCIN/AEI/10.13039/501100011033.

References

Adande, G. R., & Ziurys, L. M. 2012, ApJ, 744, 194
Aladro, R., Martín, S., Riquelme, D., et al. 2015, A&A, 579, A101
Astropy Collaboration (Price-Whelan, A. M., et al.) 2022, ApJ, 935, 167
Behrens, E., Mangum, J. G., Holdship, J., et al. 2022, ApJ, 939, 119
Bendo, G. J., Beswick, R. J., D'Cruze, M. J., et al. 2015, MNRAS, 450, L80
Bonnet, H., Abuter, R., Baker, A., et al. 2004, The Messenger, 117, 17
Buchner, J. 2016, Stat. Comput., 26, 383
Buchner, J. 2019, PASP, 131, 108005
Buchner, J. 2021, J. Open Source Software, 6, 3001
Butterworth, J., Holdship, J., Viti, S., & García-Burillo, S. 2022, A&A, 667, A131
Cazzoli, G., Puzzarini, C., & Lapinov, A. V. 2004, ApJ, 611, 615
Cazzoli, G., Puzzarini, C., & Gauss, J. 2005, ApJS, 159, 181
Chin, Y.-N., Henkel, C., Langer, N., & Mauersberger, R. 1999, ApJ, 512, L143
Clayton, D. 2003, Handbook of Isotopes in the Cosmos (Cambridge, UK: Cambridge University Press)
Colzi, L., Fontani, F., Rivilla, V. M., et al. 2018, MNRAS, 478, 3693
Colzi, L., Sipilä, O., Roueff, E., Caselli, P., & Fontani, F. 2020, A&A, 640, A51
Colzi, L., Romano, D., Fontani, F., et al. 2022, A&A, 667, A151
Danielson, A. L. R., Swinbank, A. M., Smail, I., et al. 2013, MNRAS, 436, 2793
Denis-Alpizar, O., Stoecklin, T., Dutrey, A., & Guilloteau, S. 2020, MNRAS, 497, 4276
Eisenhauer, F., Abuter, R., Bickert, K., et al. 2003, in Instrument Design and Performance for Optical/Infrared Ground-based Telescopes, eds. M. Iye, & A. F. M. Moorwood, SPIE Conf. Ser., 4841, 1548
Emig, K. L., Bolatto, A. D., Leroy, A. K., et al. 2020, ApJ, 903, 50
Endres, C. P., Schlemmer, S., Schilke, P., Stutzki, J., & Müller, H. S. P. 2016, J. Mol. Spectrosc., 327, 95
Flower, D. R. 1999, MNRAS, 305, 651
Fuchs, U., Bruenken, S., Fuchs, G. W., et al. 2004, Zeitschrift Naturforschung Teil A, 59, 861
Gardner, F. F., & Whiteoak, J. B. 1981, MNRAS, 194, 37P
Ginsburg, A., Bally, J., Barnes, A., et al. 2018, ApJ, 853, 171
Goldsmith, P. F., & Langer, W. D. 1999, ApJ, 517, 209
González-Alfonso, E., Fischer, J., Graciá-Carpio, J., et al. 2012, A&A, 541, A4
Goorvitch, D. 1994, ApJS, 95, 535
Gregersen, E. M., Evans, Neal J., & I., 2001, ApJ, 553, 1042
Haasler, D., Rivilla, V. M., Martín, S., et al. 2022, A&A, 659, A158
Harada, N., Martín, S., Mangum, J. G., et al. 2021, ApJ, 923, 24
Harada, N., Martín, S., Mangum, J. G., et al. 2022, ApJ, 938, 80
Henkel, C., Guesten, R., & Gardner, F. F. 1985, A&A, 143, 148
Henkel, C., Chin, Y. N., Mauersberger, R., & Whiteoak, J. B. 1998, A&A, 329, 443
Henkel, C., Asiri, H., Ao, Y., et al. 2014, A&A, 565, A3
Henkel, C., Mühle, S., Bendo, G., et al. 2018, A&A, 615, A155
Holdship, J., Viti, S., Martín, S., et al. 2021, A&A, 654, A55
Holdship, J., Mangum, J. G., Viti, S., et al. 2022, ApJ, 931, 89
Huang, K. Y., Viti, S., Holdship, J., et al. 2022, A&A, 666, A102
Huang, K. Y., Viti, S., Holdship, J., et al. 2023, A&A, 675, A151
Humire, P. K., Henkel, C., Hernández-Gómez, A., et al. 2022, A&A, 663, A33
Izumi, T., Kohno, K., Aalto, S., et al. 2016, ApJ, 818, 42
Izzard, R. G., Tout, C. A., Karakas, A. I., & Pols, O. R. 2004, MNRAS, 350, 407
Jiang, X., Wang, J., & Gu, Q. 2011, MNRAS, 418, 1753
Keene, J., Schilke, P., Kooi, J., et al. 1998, ApJ, 494, L107
Klapper, G., Lewen, F., Gendriesch, R., Belov, S. P., & Winnewisser, G. 2000, J. Mol. Spectrosc., 201, 124
Klapper, G., Lewen, F., Gendriesch, R., Belov, S. P., & Winnewisser, G. 2001, Zeitschrift Naturforschung Teil A, 56, 329
Klapper, G., Surin, L., Lewen, F., et al. 2003, ApJ, 582, 262
Krips, M., Neri, R., García-Burillo, S., et al. 2008, ApJ, 677, 262
Langer, W. D., & Penzias, A. A. 1990, ApJ, 357, 477
Langer, W. D., & Penzias, A. A. 1993, ApJ, 408, 539
Langer, W. D., Graedel, T. E., Frerking, M. A., & Armentrout, P. B. 1984, ApJ, 277, 581
Lattanzi, V., Walters, A., Drouin, B. J., & Pearson, J. C. 2007, ApJ, 662, 771
Leitherer, C., Schaerer, D., Goldader, J. D., et al. 1999, ApJS, 123, 3
Leitherer, C., Ekström, S., Meynet, G., et al. 2014, ApJS, 212, 14
Leroy, A. K., Bolatto, A. D., Ostriker, E. C., et al. 2015, ApJ, 801, 25
Leroy, A. K., Bolatto, A. D., Ostriker, E. C., et al. 2018, ApJ, 869, 126
Loison, J.-C., Wakelam, V., Gratier, P., et al. 2019, MNRAS, 485, 5777
Mangum, J. G., Ginsburg, A. G., Henkel, C., et al. 2019, ApJ, 871, 170
Martín, S., Muller, S., Henkel, C., et al. 2019, A&A, 624, A125
Martín, S., Mangum, J. G., Harada, N., et al. 2021, A&A, 656, A46
Meier, D. S., Walter, F., Bolatto, A. D., et al. 2015, ApJ, 801, 63
Milam, S. N., Savage, C., Brewster, M. A., Ziurys, L. M., & Wyckoff, S. 2005, ApJ, 634, 1126
Mills, E. A. C., Gorski, M., Emig, K. L., et al. 2021, ApJ, 919, 105
Müller, H. S. P., Thorwirth, S., Roth, D. A., & Winnewisser, G. 2001, A&A, 370, L49
Müller, H. S. P., Schlöder, F., Stutzki, J., & Winnewisser, G. 2005, J. Mol. Struct., 742, 215
Muller, S., Guélin, M., Dumke, M., Lucas, R., & Combes, F. 2006, A&A, 458, 417
Müller-Sánchez, F., González-Martín, O., Fernández-Ontiveros, J. A., Acosta-Pulido, J. A., & Prieto, M. A. 2010, ApJ, 716, 1166
Navarro-Almaida, D., Bop, C. T., Lique, F., et al. 2023, A&A, 670, A110
Pagel, B. E. J. 1997, Nucleosynthesis and Chemical Evolution of Galaxies (Cambridge, UK: Cambridge University Press)
Papadopoulos, P. P. 2010, ApJ, 720, 226
Papadopoulos, P. P., Thi, W.-F., Miniati, F., & Viti, S. 2011, MNRAS, 414, 1705
Pasha, I., Leja, J., van Dokkum, P. G., Conroy, C., & Johnson, B. D. 2020, ApJ, 898, 165
Pasquali, A., Gallagher, J. S., & de Grijs, R. 2004, A&A, 415, 103
Rekola, R., Richer, M. G., McCall, M. L., et al. 2005, MNRAS, 361, 330
Rico-Villas, F., Martín-Pintado, J., González-Alfonso, E., Martín, S., & Rivilla, V. M. 2020, MNRAS, 491, 4573
Rico-Villas, F., González-Alfonso, E., Martín-Pintado, J., Rivilla, V. M., & Martín, S. 2022, MNRAS, 516, 1094
Romano, D. 2022, A&A Rev., 30, 7
Romano, D., Matteucci, F., Zhang, Z.-Y., Papadopoulos, P. P., & Ivison, R. J. 2017, MNRAS, 470, 401
Romano, D., Matteucci, F., Zhang, Z.-Y., Ivison, R. J., & Ventura, P. 2019, MNRAS, 490, 2838
Rosenberg, M. J. F., van der Werf, P. P., & Israel, F. P. 2013, A&A, 550, A12
Roueff, E., Loison, J. C., & Hickson, K. M. 2015, A&A, 576, A99
Salpeter, E. E. 1955, ApJ, 121, 161
Savage, C., Apponi, A. J., Ziurys, L. M., & Wyckoff, S. 2002, ApJ, 578, 211
Schmid-Burgk, J., Muders, D., Müller, H. S. P., & Brupbacher-Gatehouse, B. 2004, A&A, 419, 949
Schöier, F. L., van der Tak, F. F., van Dishoeck, E. F., & Black, J. H. 2005, A&A, 432, 369
Sipilä, O., Colzi, L., Roueff, E., et al. 2023, A&A, 678, A120
Sliwa, K., Wilson, C. D., Krips, M., et al. 2013, ApJ, 777, 126
Sliwa, K., Wilson, C. D., Iono, D., Peck, A., & Matsushita, S. 2014, ApJ, 796, L15
Spilker, J. S., Marrone, D. P., Aguirre, J. E., et al. 2014, ApJ, 785, 149
Szücs, L., Glover, S. C. O., & Klessen, R. S. 2014, MNRAS, 445, 4055
Tang, X. D., Henkel, C., Menten, K. M., et al. 2019, A&A, 629, A6
Tinti, F., Bizzocchi, L., Degli Esposti, C., & Dore, L. 2007, ApJ, 669, L113
Turner, J. L., & Ho, P. T. P. 1985, ApJ, 299, L77
van der Tak, F. F. S., Black, J. H., Schöier, F. L., Jansen, D. J., & van Dishoeck, E. F. 2007, A&A, 468, 627
van der Tak, F. F. S., Lique, F., Faure, A., Black, J. H., & van Dishoeck, E. F. 2020, Atoms, 8, 15
Viti, S., Fontani, F., Jiménez-Serra, I., & Holdship, J. 2019, MNRAS, 486, 4805

Viti, S., Fontani, F., & Jiménez-Serra, I. 2020, MNRAS, 497, 4333
Wallström, S. H. J., Muller, S., & Guélin, M. 2016, A&A, 595, A96
Wang, M., Chin, Y. N., Henkel, C., Whiteoak, J. B., & Cunningham, M. 2009, ApJ, 690, 580
Wang, J., Zhang, Z.-Y., Qiu, J., et al. 2014, ApJ, 796, 57
Wang, J., Zhang, Z.-Y., Zhang, J., Shi, Y., & Fang, M. 2016, MNRAS, 455, 3986
Wiescher, M., Görres, J., Uberseder, E., Imbriani, G., & Pignatari, M. 2010, Ann. Rev. Nucl. Part. Sci., 60, 381
Wilson, T. L., & Rood, R. 1994, ARA&A, 32, 191
Winnewisser, G., Belov, S. P., Klaus, T., & Schieder, R. 1997, J. Mol. Spectrosc., 184, 468
Wouterloot, J. G. A., & Brand, J. 1996, A&AS, 119, 439
Wouterloot, J. G. A., Henkel, C., Brand, J., & Davis, G. R. 2008, A&A, 487, 237
Yan, Y. T., Zhang, J. S., Henkel, C., et al. 2019, ApJ, 877, 154
Yan, Y. T., Henkel, C., Kobayashi, C., et al. 2023, A&A, 670, A98
Yang, B., Stancil, P. C., Balakrishnan, N., & Forrey, R. C. 2010, ApJ, 718, 1062
Zhang, J. S., Liu, W., Yan, Y. T., et al. 2020, ApJS, 249, 6

[1] Leiden Observatory, Leiden University, PO Box 9513, 2300 RA Leiden, The Netherlands
e-mail: butterworth@strw.leidenuniv.nl
[2] National Radio Astronomy Observatory, 520 Edgemont Road, Charlottesville, VA 22903, USA
[3] European Southern Observatory, Alonso de Córdova, 3107, Vitacura, Santiago 763-0355, Chile
[4] Joint ALMA Observatory, Alonso de Córdova, 3107, Vitacura, Santiago 763-0355, Chile
[5] National Astronomical Observatory of Japan, 2-21-1 Osawa, Mitaka, Tokyo 181-8588, Japan
[6] Institute of Astronomy and Astrophysics, Academia Sinica, 11F of AS/NTU Astronomy-Mathematics Building, No.1, Sec. 4, Roosevelt Rd, Taipei 10617, Taiwan
[7] Department of Astronomy, School of Science, The Graduate University for Advanced Studies (SOKENDAI), 2-21-1 Osawa, Mitaka, Tokyo 181-1855, Japan
[8] Department of Space, Earth and Environment, Chalmers University of Technology, Onsala Space Observatory, 43992 Onsala, Sweden
[9] Institute of Astronomy, Graduate School of Science, The University of Tokyo, 2-21-1 Osawa, Mitaka, Tokyo 181-0015, Japan
[10] Department of Physics, Faculty of Science and Technology, Keio University, 3-14-1 Hiyoshi, Yokohama, Kanagawa 223–8522, Japan
[11] Institute of Space Sciences (ICE, CSIC), Campus UAB, Carrer de Magrans, 08193 Barcelona, Spain
[12] Centro de Astrobiología (CAB, CSIC-INTA), Ctra. de Torrejón a Ajalvir km 4, 28850 Torrejón de Ardoz, Madrid, Spain
[13] Department of Astronomy, University of Virginia, PO Box 400325, 530 McCormick Road, Charlottesville, VA 22904-4325, USA
[14] Max-Planck-Institut für Radioastronomie, Auf-dem-Hügel 69, 53121 Bonn, Germany
[15] Astron. Dept., Faculty of Science, King Abdulaziz University, PO Box 80203, Jeddah 21589, Saudi Arabia
[16] Xinjiang Astronomical Observatory, Chinese Academy of Sciences, 830011 Urumqi, PR China
[17] New Mexico Institute of Mining and Technology, 801 Leroy Place, Socorro, NM 87801, USA
[18] National Radio Astronomy Observatory, PO Box O, 1003 Lopezville Road, Socorro, NM 87801, USA
[19] Cosmic Dawn Center (DAWN), Copenhagen, Denmark
[20] DTU Space, Technical University of Denmark, Elektrovej 327, 2800 Kgs. Lyngby, Denmark
[21] Department of Physics and Astronomy, University of British Columbia, 6225 Agricultural Rd., Vancouver V6T 1Z1, Canada

Appendix A: Additional moment 0 maps

This Appendix includes the remaining moment 0 maps generated using `CubeLineMoment`. The maps are provided in temperature units and cover the CMZ of NGC 253.

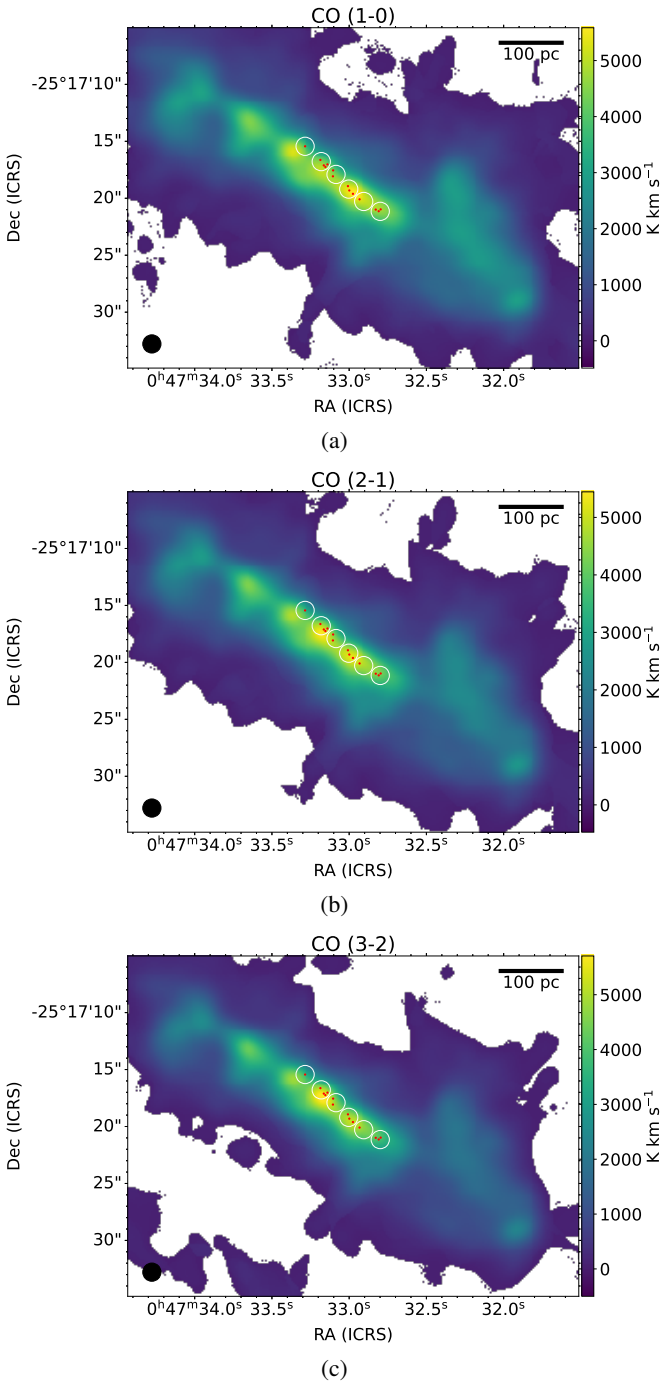

Fig. A.1. Velocity-integrated line intensities in [K km s^{-1}] of CO (1-0), (2-1), and (3-2). Each of the maps shown was generated using a signal-to-noise-ratio cutoff of 3. The studied SSC regions as listed in Table 4 are labelled in white text on the map. The original SSC locations with appropriate beam sizes from Leroy et al. (2018) are shown by the red regions. The ALCHEMI 1″.6 × 1″.6 beam is displayed in the lower-left corner of the map.

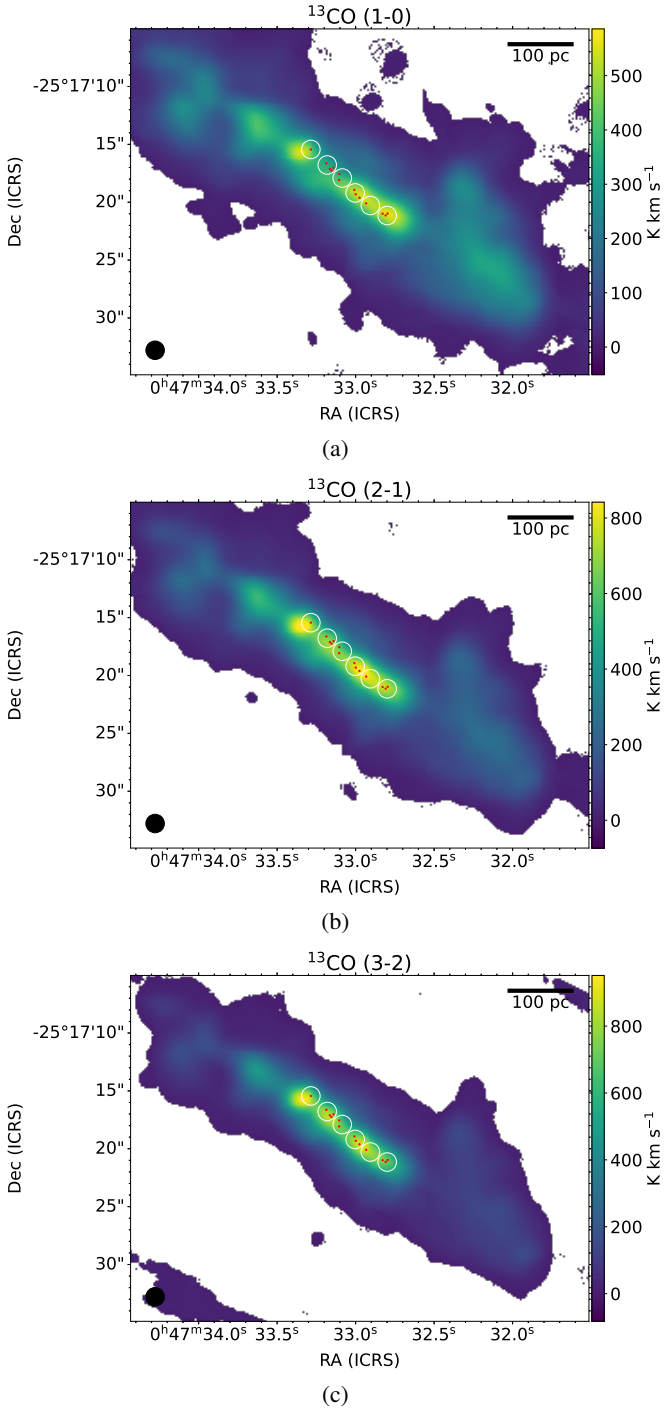

Fig. A.2. Velocity-integrated line intensities in [K km s^{-1}] of ^{13}CO (1-0), (2-1) and (3-2). Each of the maps shown was generated using a signal-to-noise-ratio cutoff of 3. The studied SSC regions as listed in Table 4 are labelled in white text on the map. The original SSC locations with appropriate beam sizes from Leroy et al. (2018) are shown by the red regions. The ALCHEMI 1″.6 × 1″.6 beam is displayed in the lower-left corner of the map.

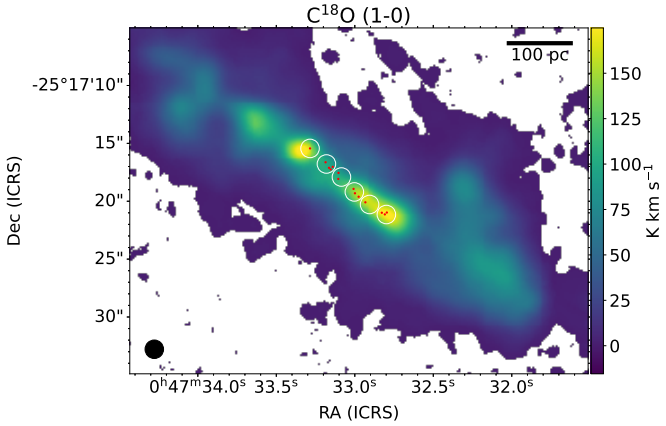

(a)

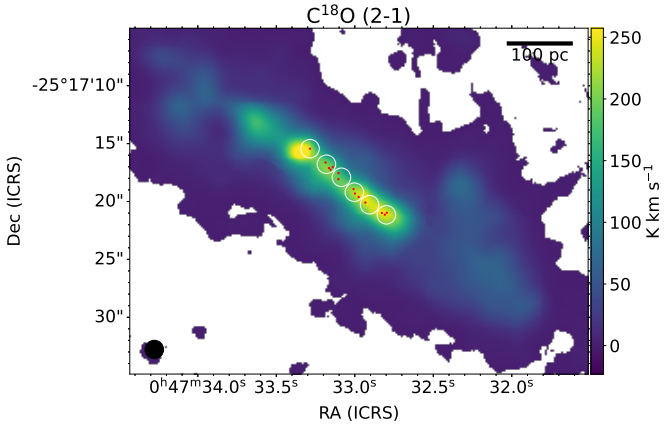

(b)

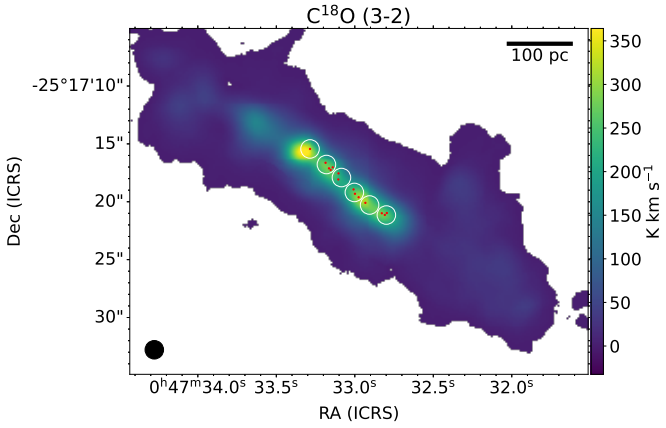

(c)

Fig. A.3. Velocity-integrated line intensities in [K km s^{-1}] of C^{18}O (1-0), (2-1) and (3-2). Each of the maps shown was generated using a signal-to-noise-ratio cutoff of 3. The studied SSC regions as listed in Table 4 are labelled in white text on the map. The original SSC locations with appropriate beam sizes from Leroy et al. (2018) are shown by the red regions. The ALCHEMI 1″.6 × 1″.6 beam is displayed in the lower-left corner of the map.

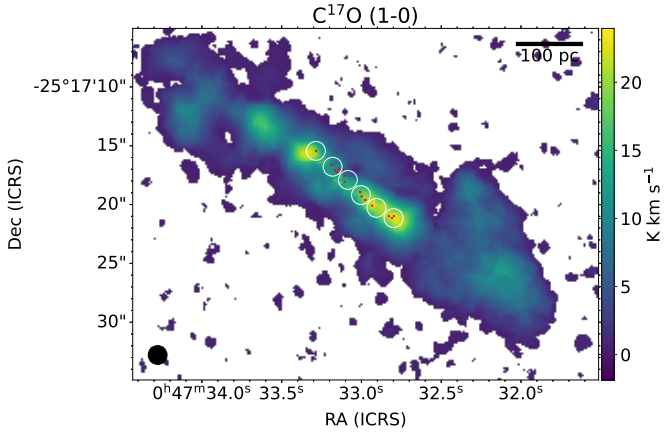

(a)

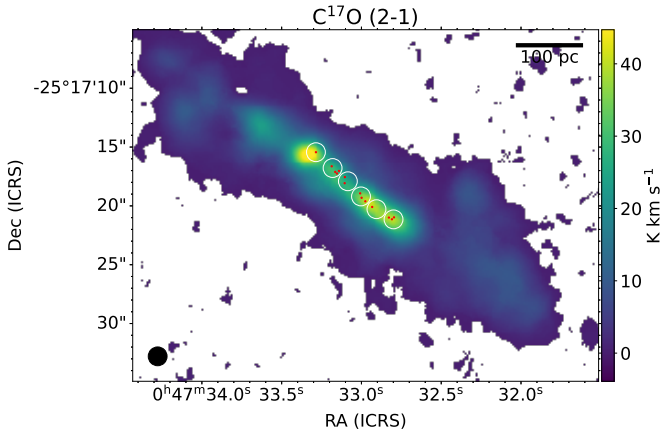

(b)

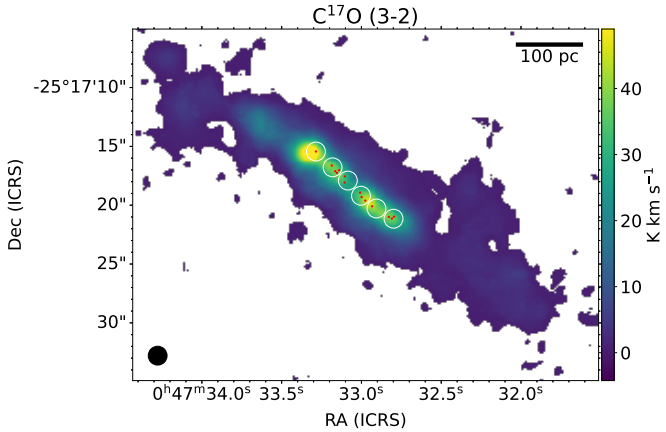

(c)

Fig. A.4. Velocity-integrated line intensities in [K km s^{-1}] of C^{17}O (1-0), (2-1) and (3-2). Each of the maps shown was generated using a signal-to-noise-ratio cutoff of 3. The studied SSC regions as listed in Table 4 are labelled in white text on the map. The original SSC locations with appropriate beam sizes from Leroy et al. (2018) are shown by the red regions. The ALCHEMI 1″.6 × 1″.6 beam is displayed in the lower-left corner of the map.

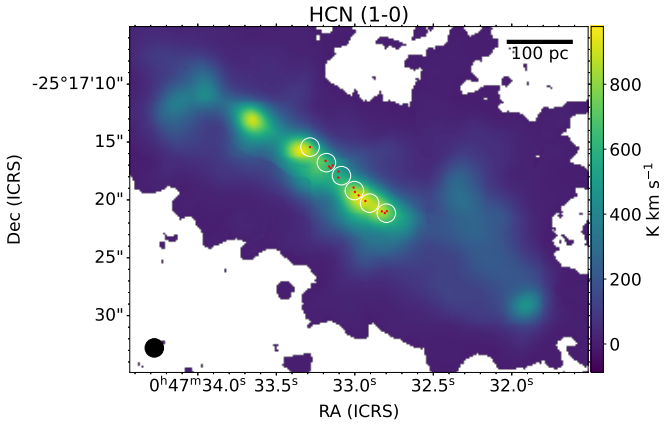

(a)

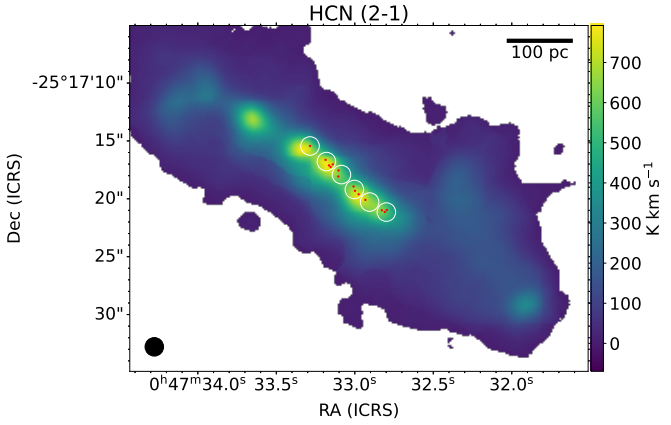

(b)

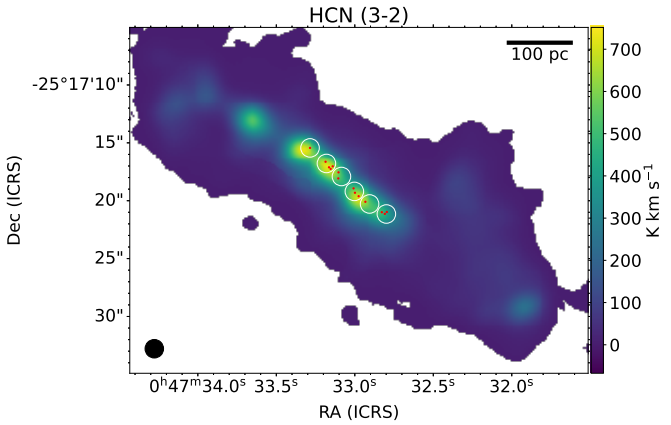

(c)

Fig. A.5. Velocity-integrated line intensities in [K km s^{-1}] of HCN (1-0), (2-1) and (3-2). Each of the maps shown was generated using a signal-to-noise-ratio cutoff of 3. The studied SSC regions as listed in Table 4 are labelled in white text on the map. The original SSC locations with appropriate beam sizes from Leroy et al. (2018) are shown by the red regions. The ALCHEMI 1″.6 × 1″.6 beam is displayed in the lower-left corner of the map.

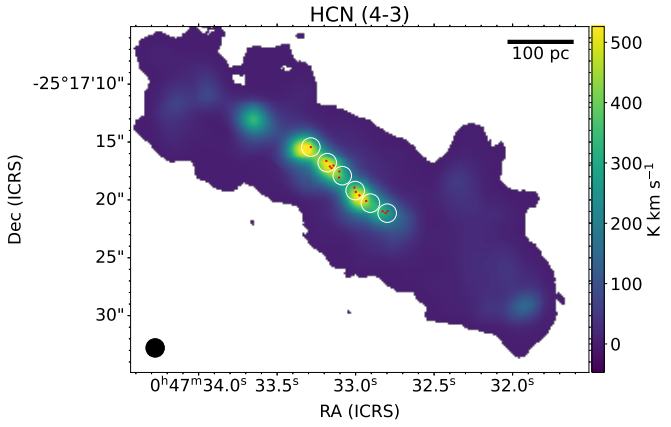

(a)

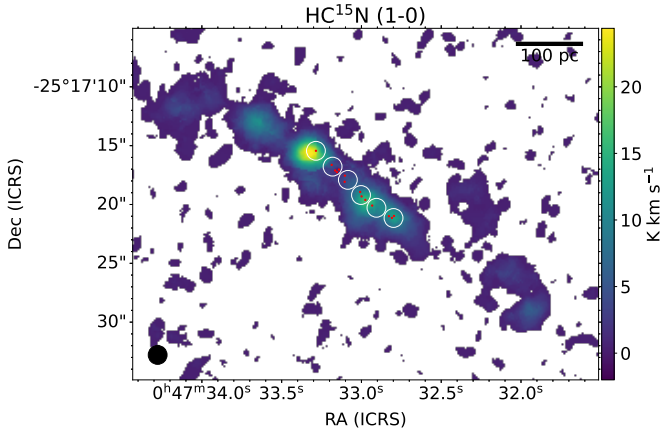

(b)

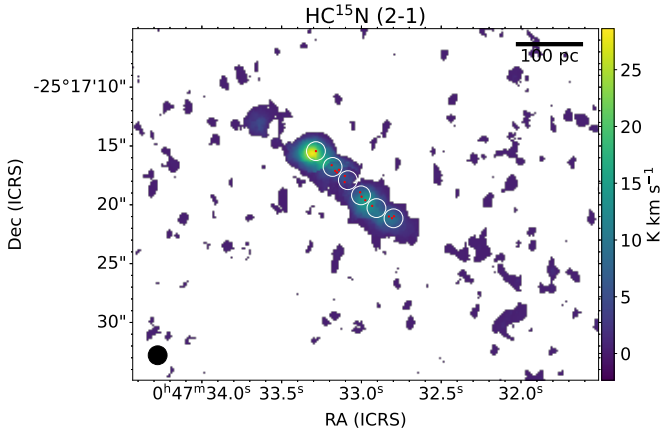

(c)

Fig. A.6. Velocity-integrated line intensities in [K km s^{-1}] of HCN (4-3), HC^{15}N(1-0) and (2-1). Each of the maps shown was generated using a signal-to-noise-ratio cutoff of 3. The studied SSC regions as listed in Table 4 are labelled in white text on the map. The original SSC locations with appropriate beam sizes from Leroy et al. (2018) are shown by the red regions. The ALCHEMI 1″.6 × 1″.6 beam is displayed in the lower-left corner of the map.

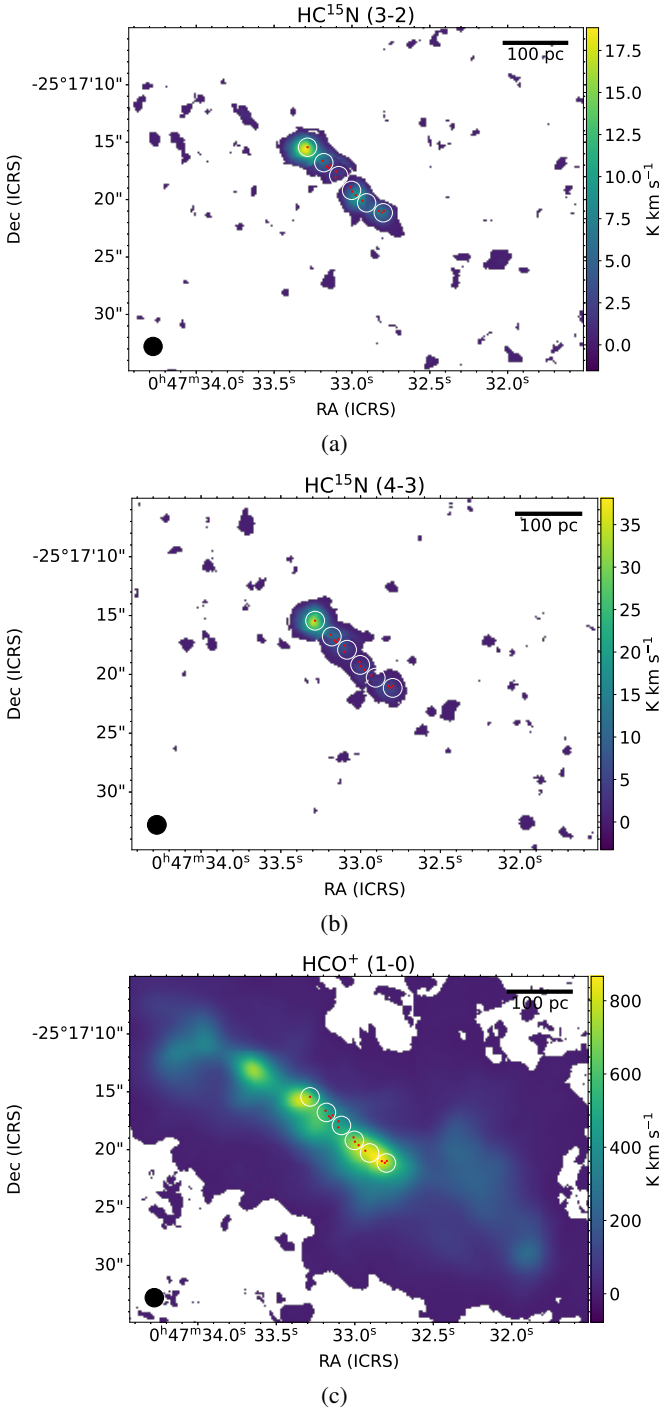

Fig. A.7. Velocity-integrated line intensities in [K km s^{-1}] of HC^{15}N (3-2), (4-3) and HCO$^+$ (1-0). Each of the maps shown was generated using a signal-to-noise-ratio cutoff of 3. The studied SSC regions as listed in Table 4 are labelled in white text on the map. The original SSC locations with appropriate beam sizes from Leroy et al. (2018) are shown by the red regions. The ALCHEMI 1″.6×1″.6 beam is displayed in the lower-left corner of the map.

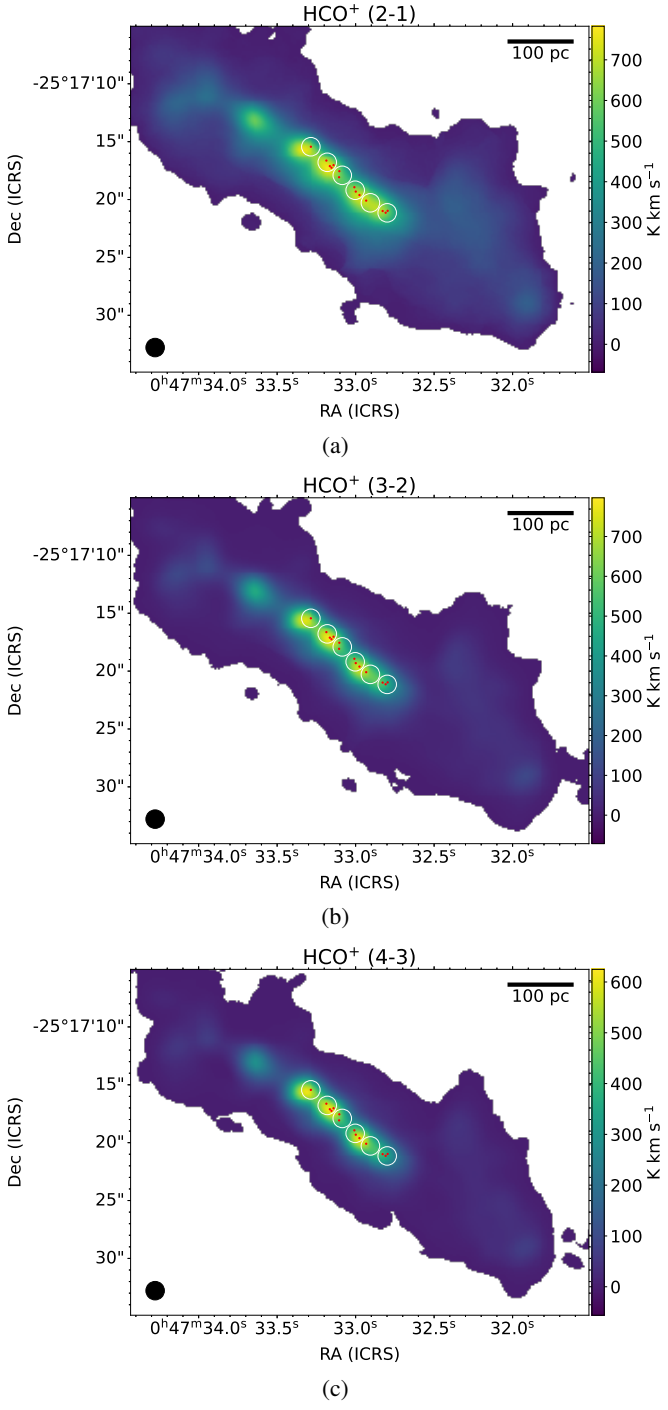

Fig. A.8. Velocity-integrated line intensities in [K km s^{-1}] of HCO$^+$ (1-0), (2-1) and (3-2). Each of the maps shown was generated using a signal-to-noise-ratio cutoff of 3. The studied SSC regions as listed in Table 4 are labelled in white text on the map. The original SSC locations with appropriate beam sizes from Leroy et al. (2018) are shown by the red regions. The ALCHEMI 1″.6×1″.6 beam is displayed in the lower-left corner of the map.

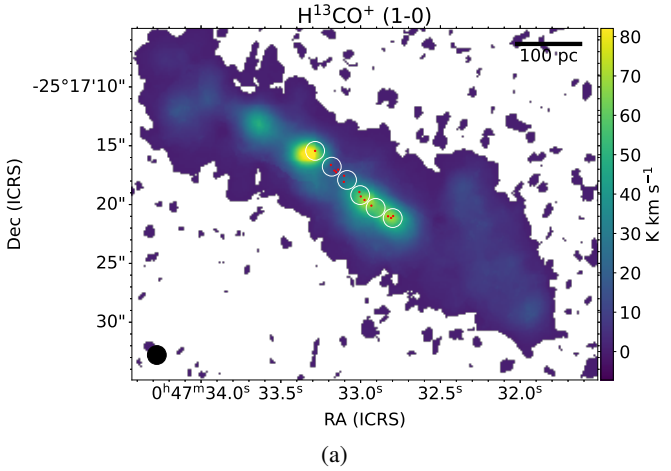

(a)

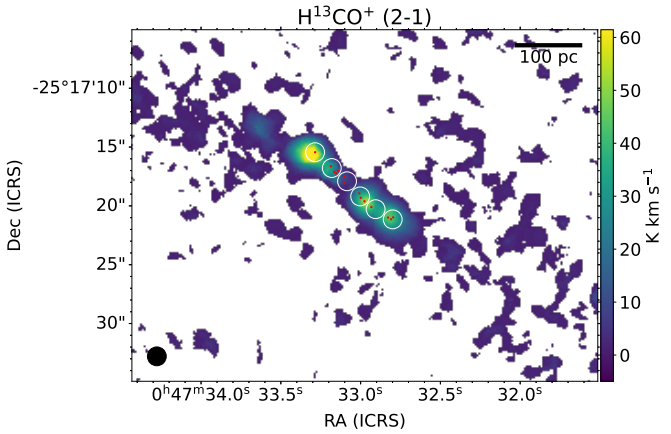

(b)

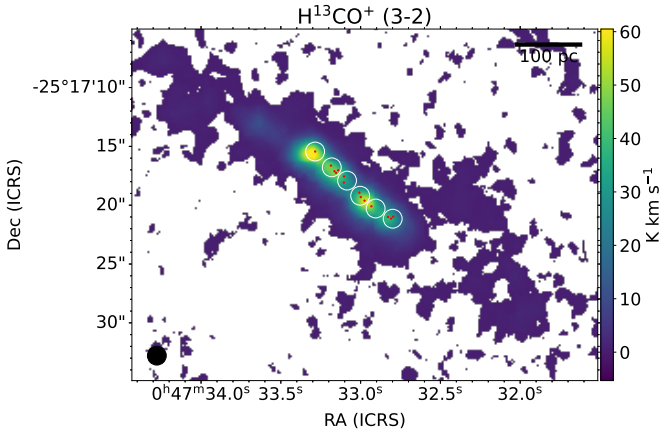

(c)

Fig. A.9. Velocity-integrated line intensities in [K km s^{-1}] of $H^{13}CO^+$ (1-0), (2-1) and (3-2). Each of the maps shown was generated using a signal-to-noise-ratio cutoff of 3. The studied SSC regions as listed in Table 4 are labelled in white text on the map. The original SSC locations with appropriate beam sizes from Leroy et al. (2018) are shown by the red regions. The ALCHEMI 1″.6×1″.6 beam is displayed in the lower-left corner of the map.

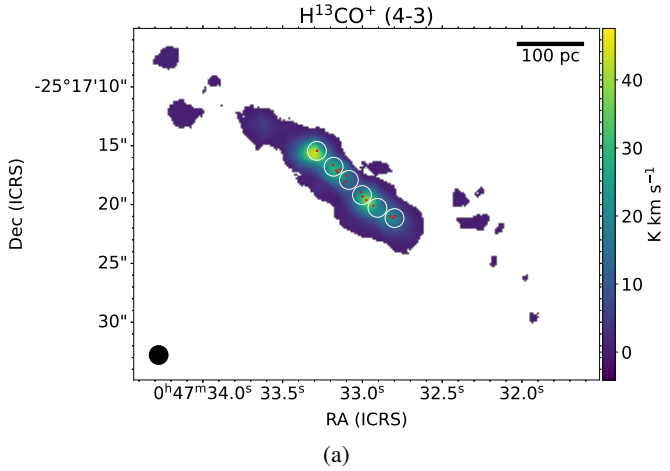

(a)

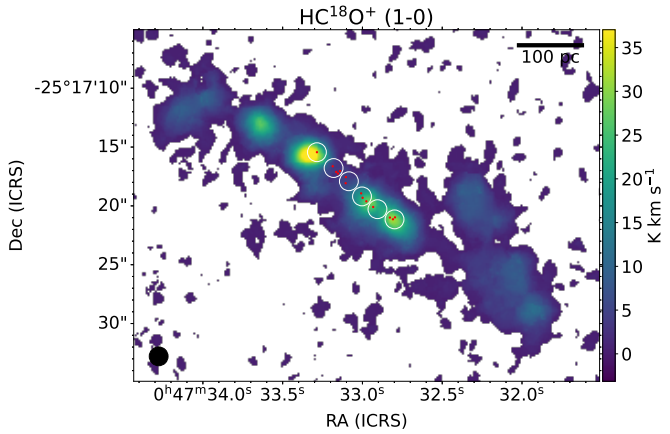

(b)

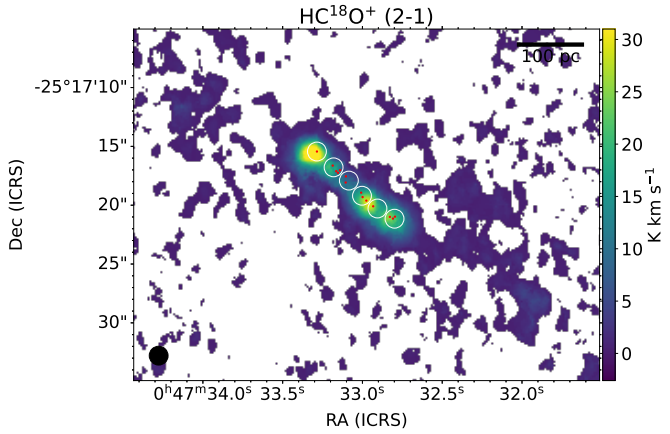

(c)

Fig. A.10. Velocity-integrated line intensities in [K km s^{-1}] of $H^{13}CO^+$ (4-3), $HC^{18}O^+$ (1-0) and (2-1).Each of the maps shown was generated using a signal-to-noise-ratio cutoff of 3. The studied SSC regions as listed in Table 4 are labelled in white text on the map. The original SSC locations with appropriate beam sizes from Leroy et al. (2018) are shown by the red regions. The ALCHEMI 1″.6×1″.6 beam is displayed in the lower-left corner of the map.

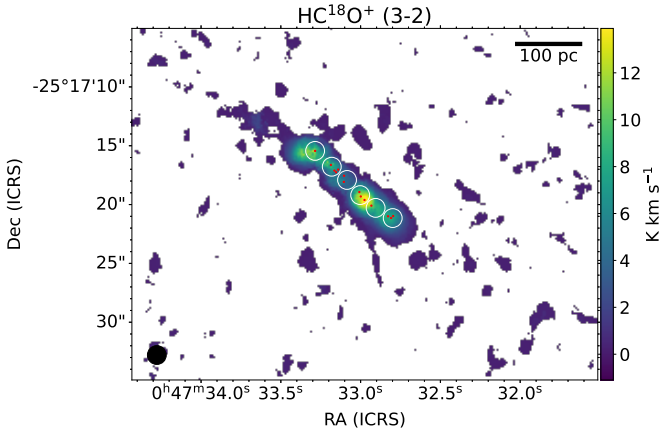

Fig. A.11. Velocity-integrated line intensities in [K km s^{-1}] of $HC^{18}O^+$ (3-2). Each of the maps shown was generated using a signal-to-noise-ratio cutoff of 3. The studied SSC regions as listed in Table 4 are labelled in white text on the map. The original SSC locations with appropriate beam sizes from Leroy et al. (2018) are shown by the red regions. The ALCHEMI 1″.6 × 1″.6 beam is displayed in the lower-left corner of the map.

Appendix B: Absorption at the TH2 position

Within this section, the effect of the TH2 region on SSC-13* and SSC-9* is demonstrated. This effect is shown both for the affected spectra and on column density ratio versus age diagrams.

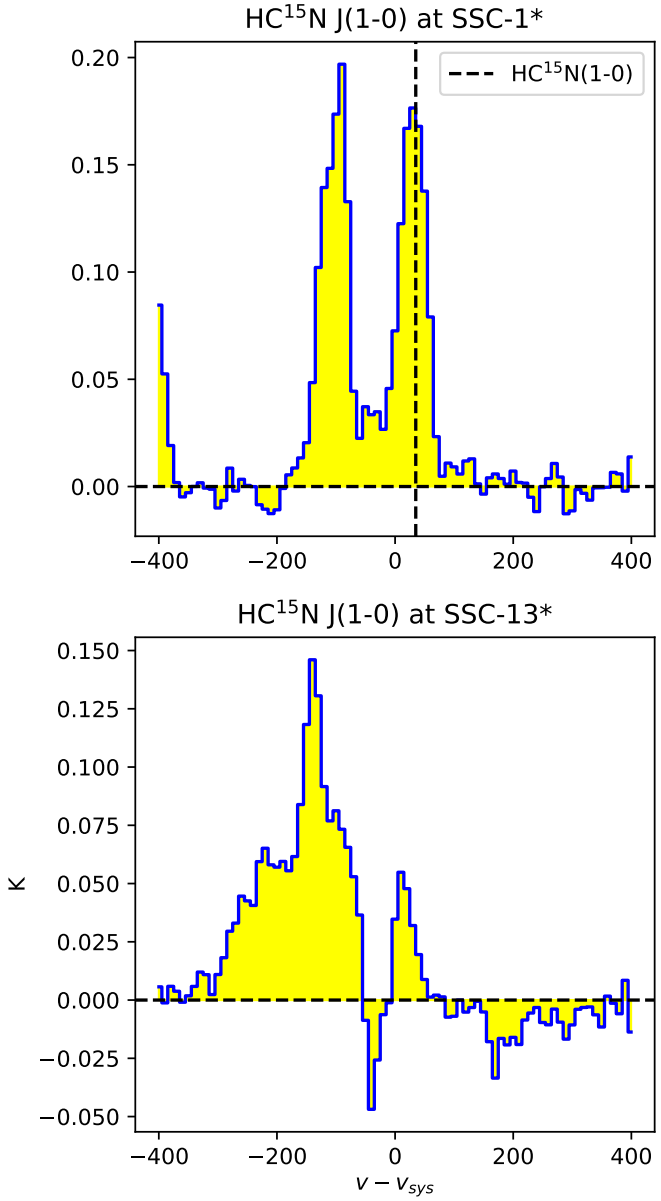

Fig. B.1. Systemic subtracted velocity spectra for $HC^{15}(1\text{-}0)$ shown for regions SSC-1* (representative of unaffected regions) and SSC-13* (representative of absorption-affected regions).

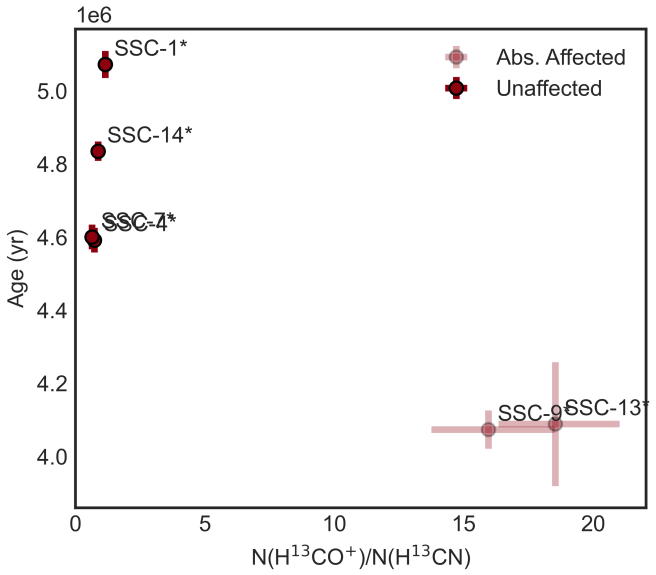

Fig. B.2. $H^{13}CO^+/H^{13}CN$ column density ratio derived from RADEX. The regions unaffected by the absorption effects observed near GMC-5 in NGC 253 are shown in full colour, whereas those regions that are effected are shaded.

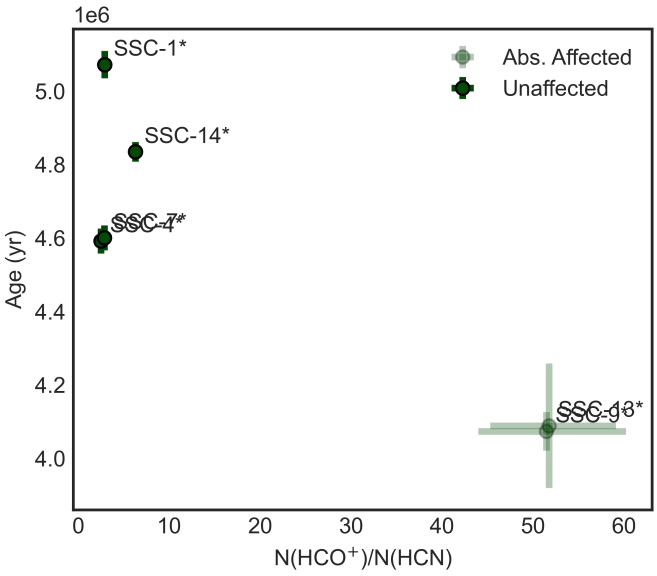

Fig. B.3. The HCO^+/HCN column density ratio derived from RADEX. The regions unaffected by the absorption effects observed near GMC-5 in NGC 253 are shown in full colour, whereas those regions that are effected are shaded.

Appendix C: Additional posterior distributions

This section contains the remaining posterior distributions generated from the nested sampling of the RADEX modelling.

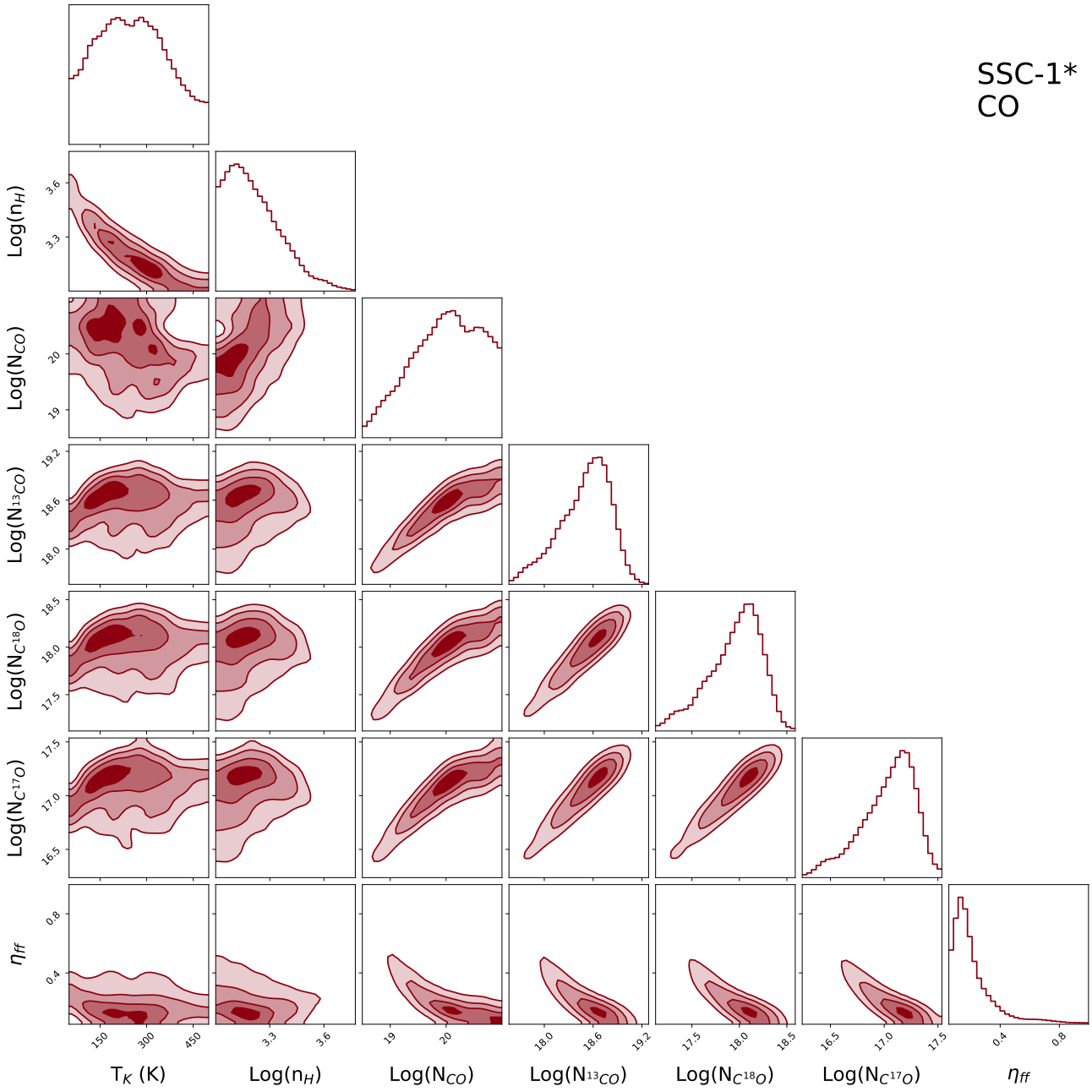

Fig. C.1. Posterior distributions for SSC-1* of the kinetic temperature, neutral H_2 number density, beam filling factor and column densities of CO, ^{13}CO, C^{18}O, and C^{17}O, as predicted by RADEX.

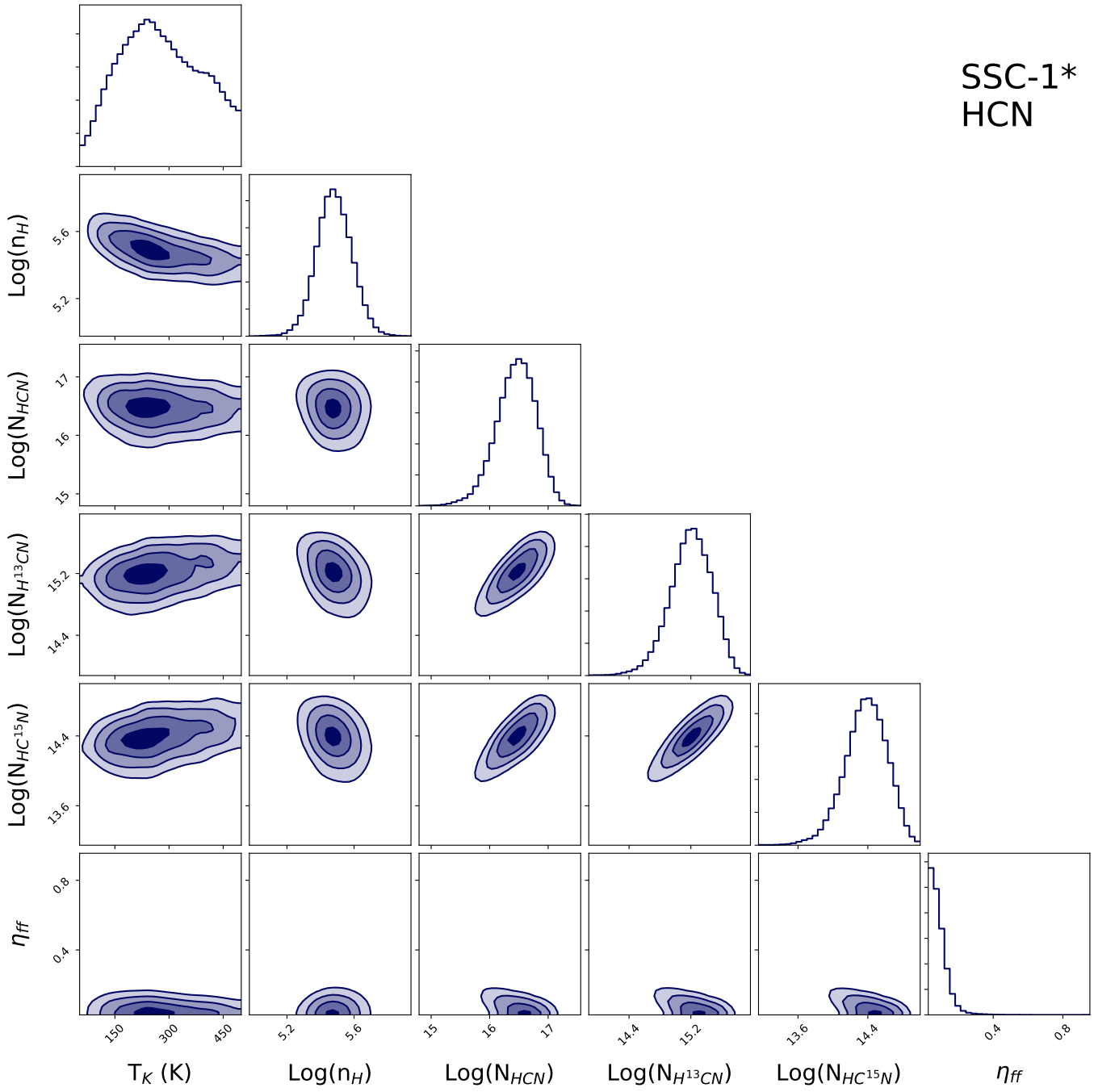

Fig. C.2. Posterior distributions for SSC-1* of the kinetic temperature, neutral H_2 number density, beam filling factor and column densities of HCN, $H^{13}CN$ and HC ^{15}N, as predicted by `RADEX`.

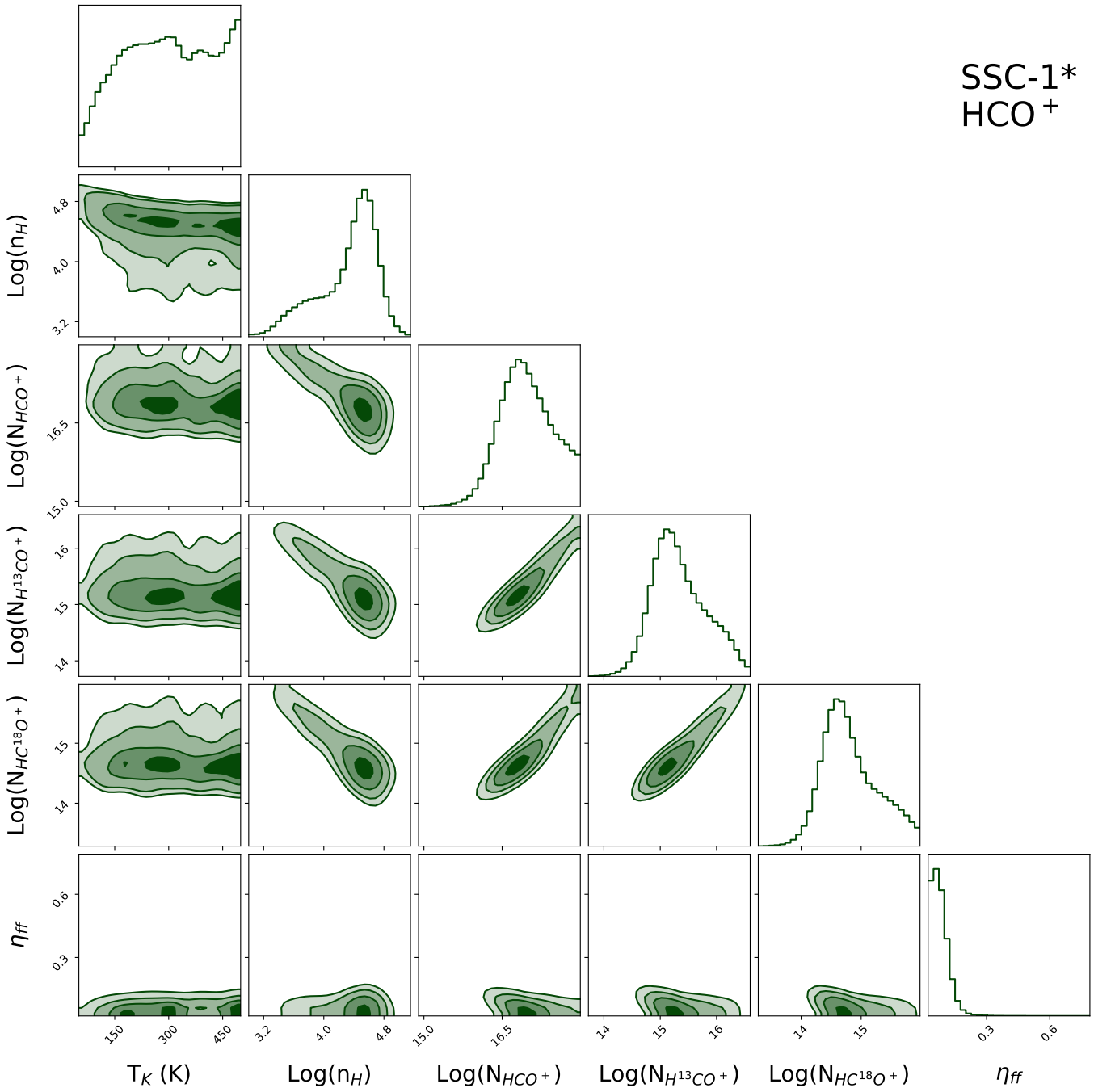

Fig. C.3. Posterior distributions for SSC-1* of the kinetic temperature, neutral H_2 number density, beam filling factor, and column densities of HCO^+, $H^{13}CO^+$, and $HC^{18}O^+$, as predicted by `RADEX`.

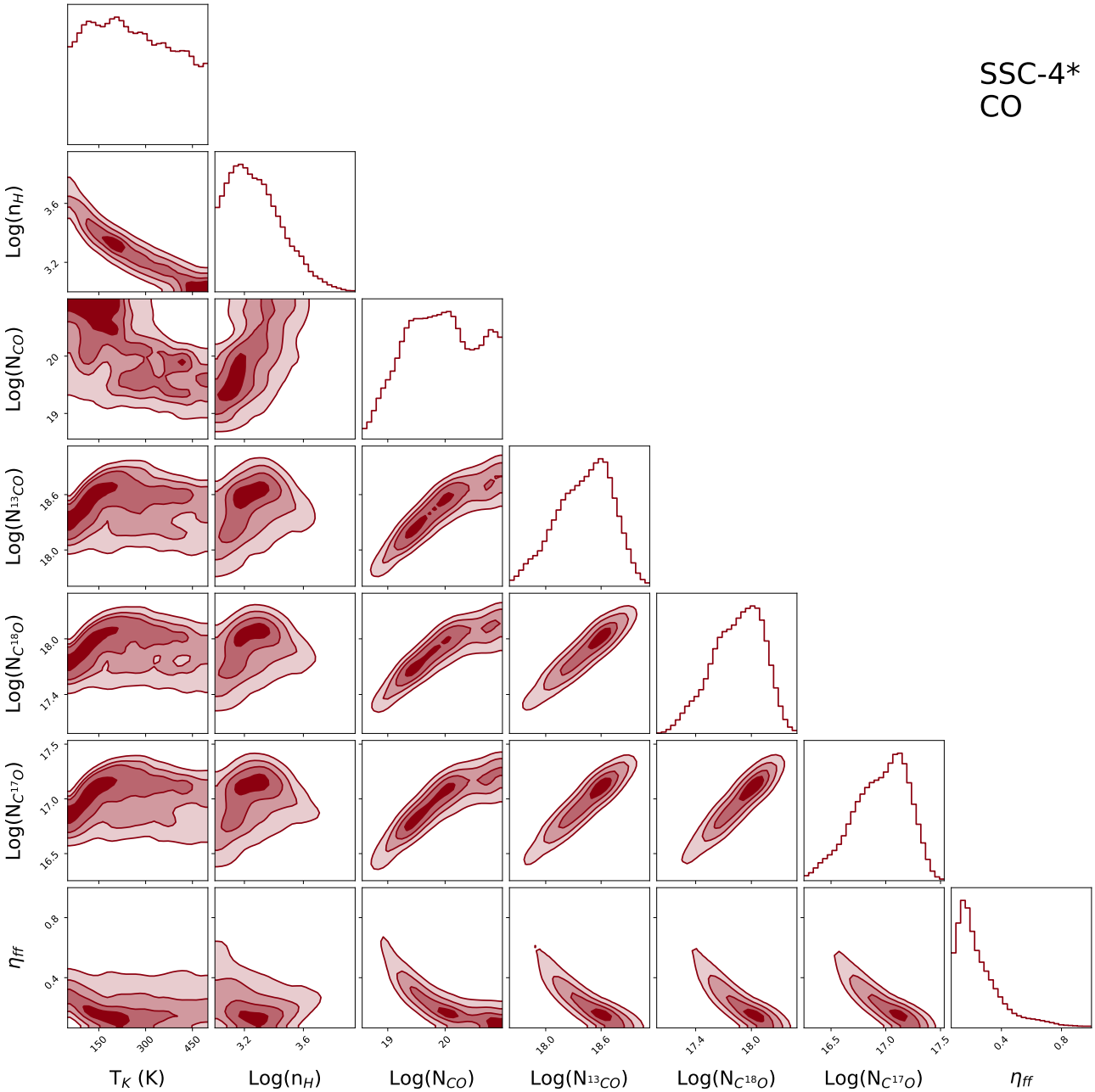

Fig. C.4. Posterior distributions the kinetic temperature, neutral H_2 number density, beam filling factor, and column densities of CO, ^{13}CO, C^{18}O, and C^{17}O, as predicted by RADEX for SSC-4* .

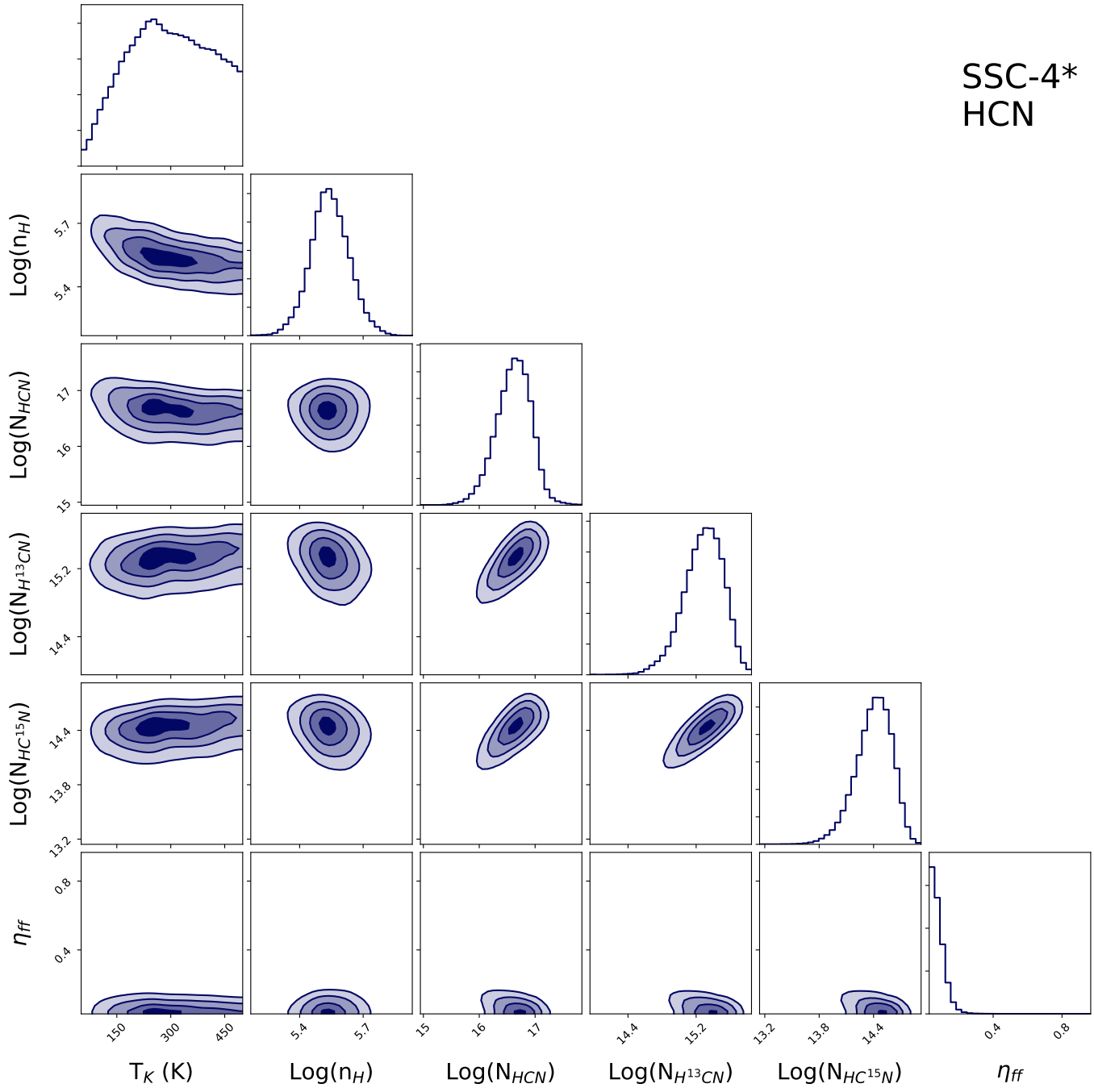

Fig. C.5. Posterior distributions of kinetic temperature, neutral H_2 number density, beam filling factor, and column densities of HCN, $H^{13}CN$, and $HC^{15}N$, as predicted by RADEX for SSC-4* .

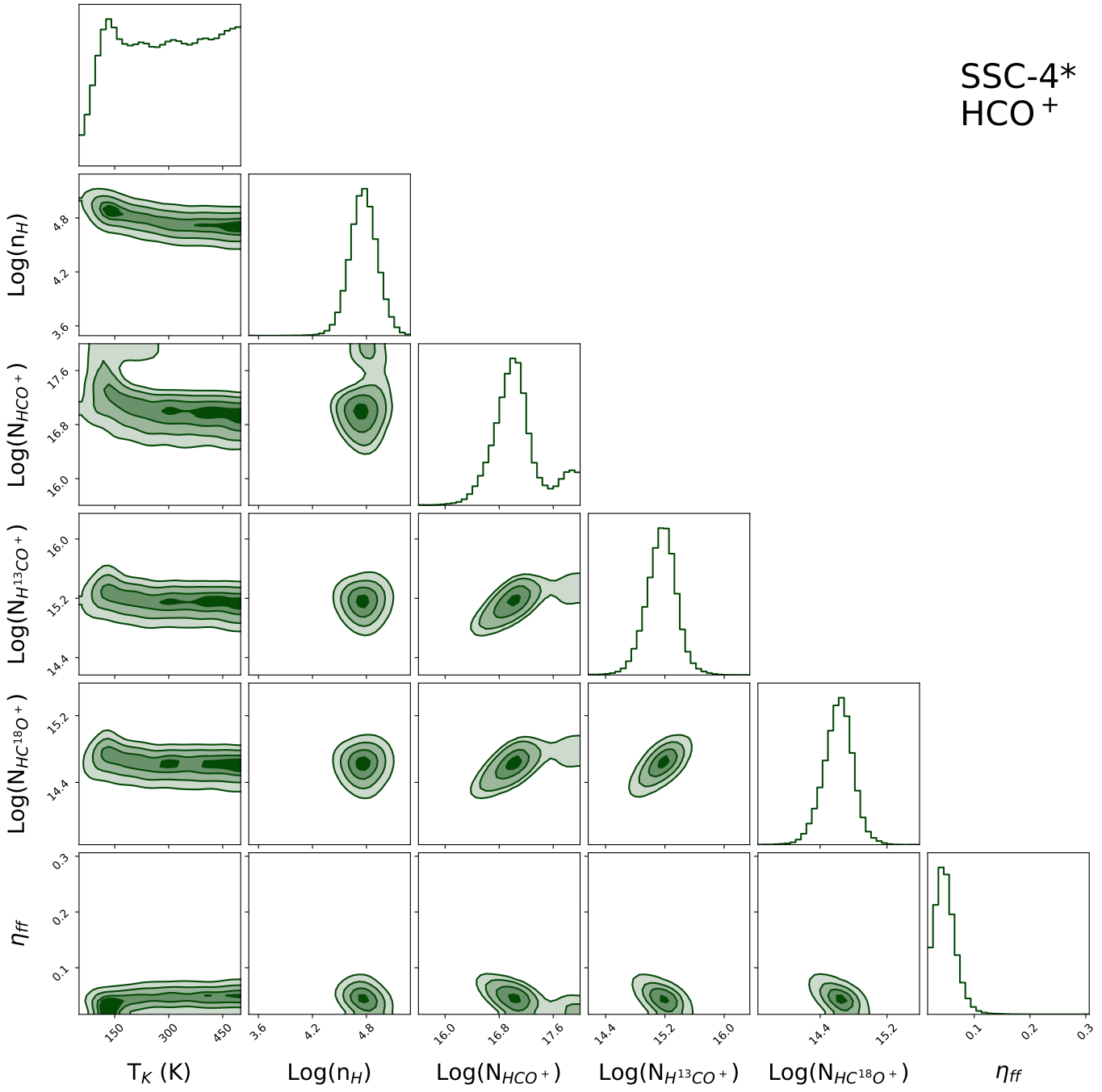

Fig. C.6. Posterior distributions of the kinetic temperature, neutral H_2 number density, beam filling factor, and column densities of HCO^+, $H^{13}CO^+$, and $HC^{18}O^+$, as predicted by `RADEX` for SSC-4*.

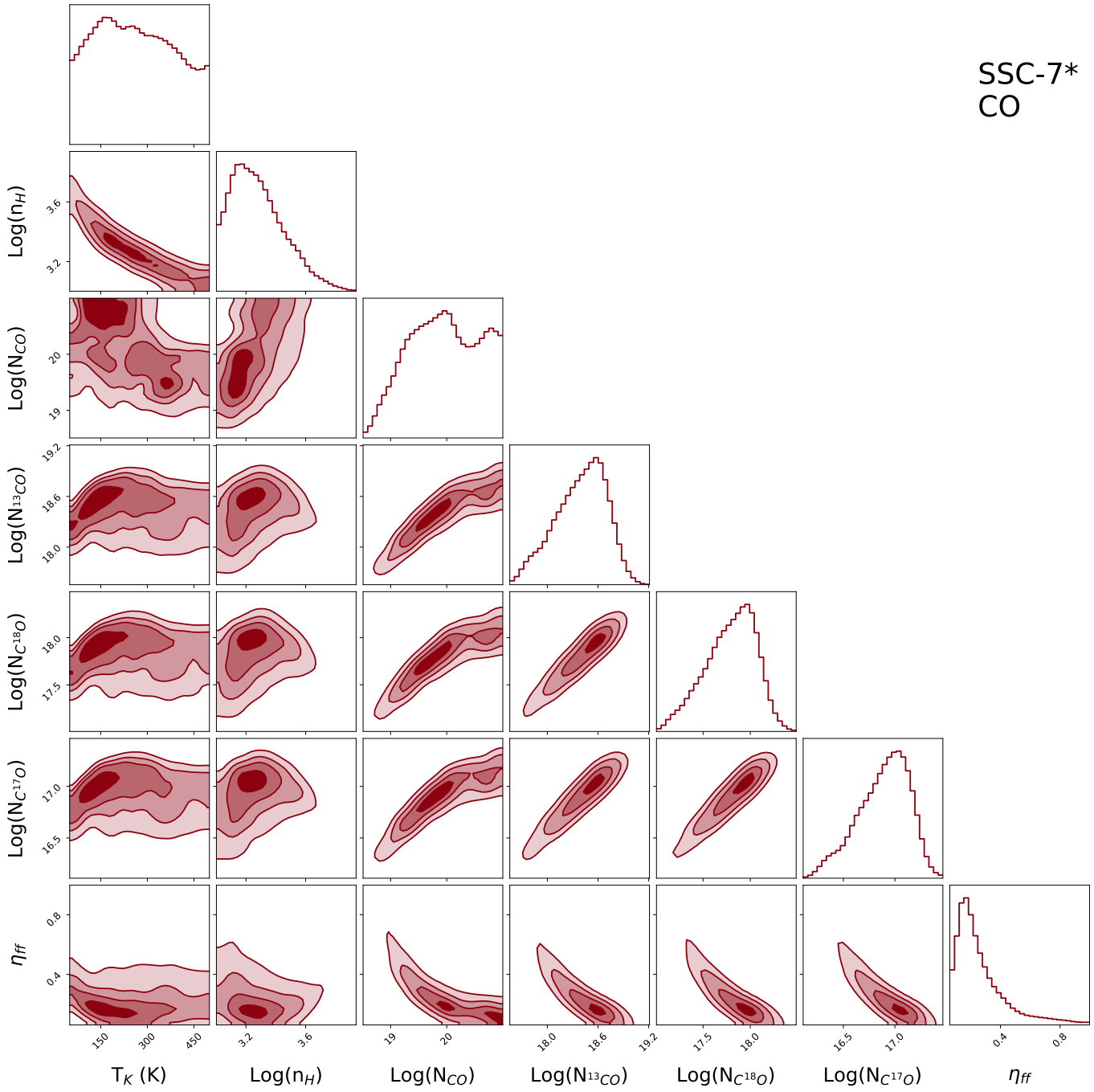

Fig. C.7. Posterior distributions for SSC-7* of the kinetic temperature, neutral H_2 number density, beam filling factor and column densities of CO, ^{13}CO, $C^{18}O$, and $C^{17}O$, as predicted by `RADEX`.

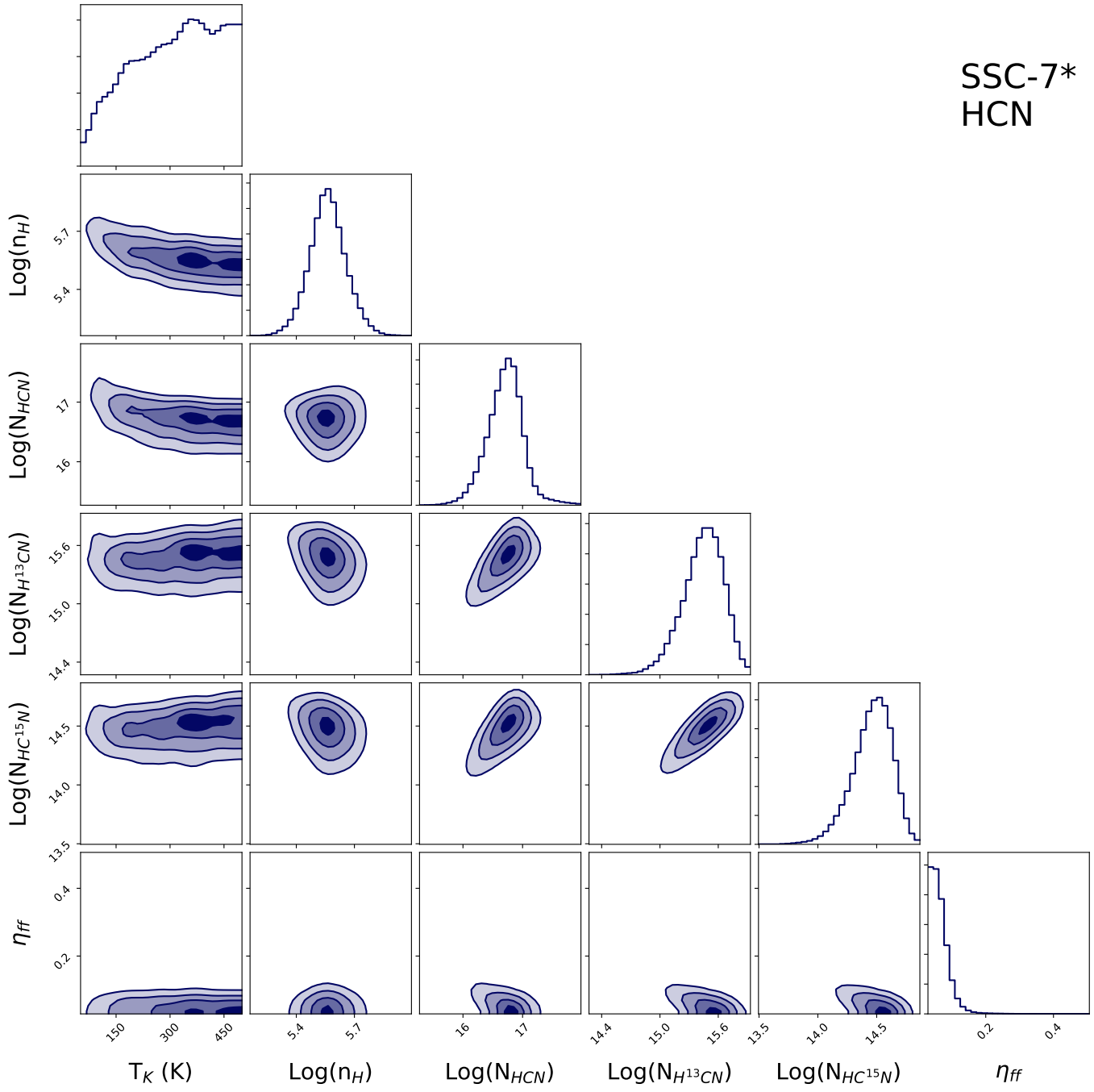

Fig. C.8. Posterior distributions for SSC-7* of the kinetic temperature, neutral H_2 number density, beam filling factor and column densities of HCN, $H^{13}CN$ and HC ^{15}N, as predicted by RADEX.

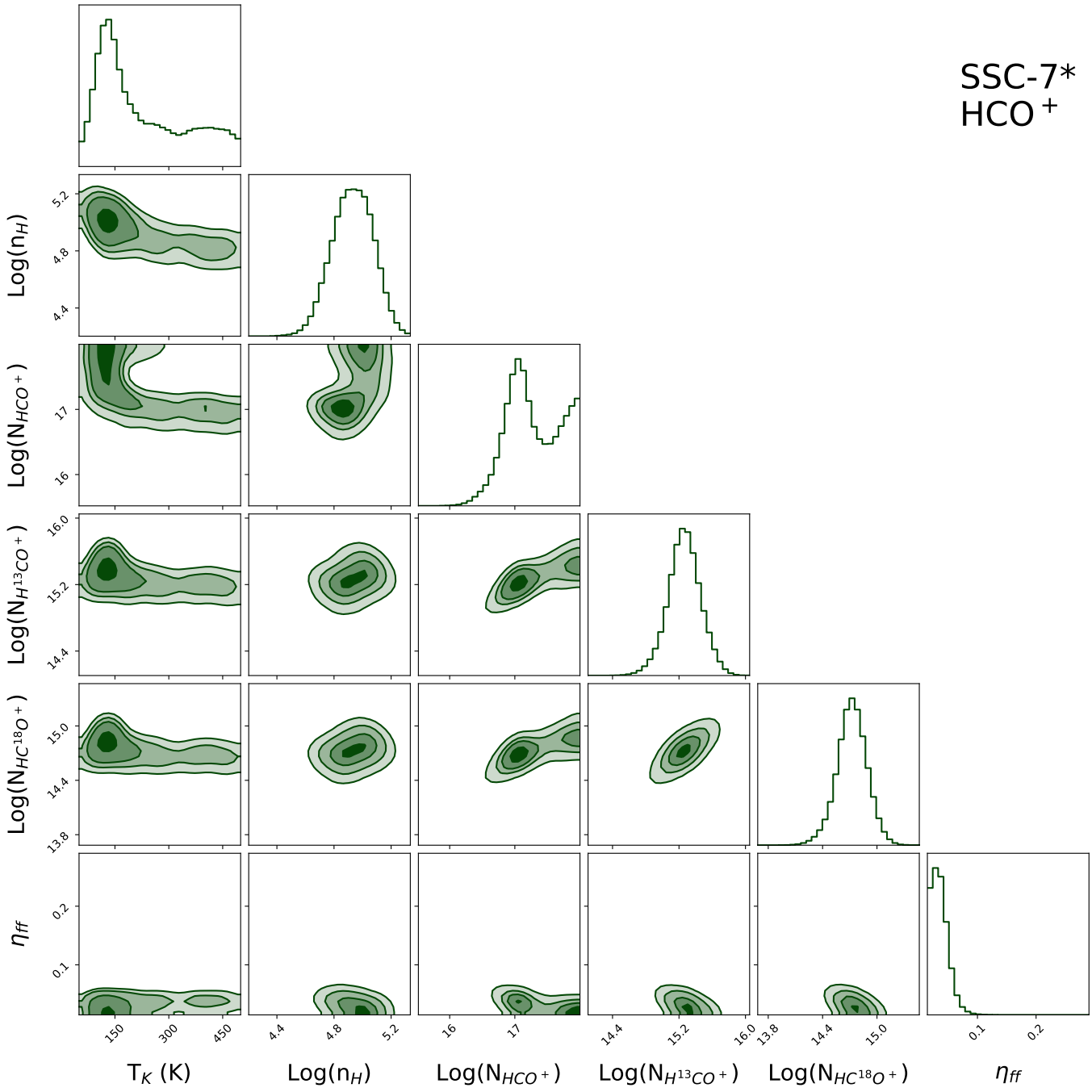

Fig. C.9. Posterior distributions for SSC-7* of the kinetic temperature, neutral H_2 number density, beam filling factor and column densities of HCO^+, $H^{13}CO^+$ and $HC^{18}O^+$, as predicted by `RADEX`.

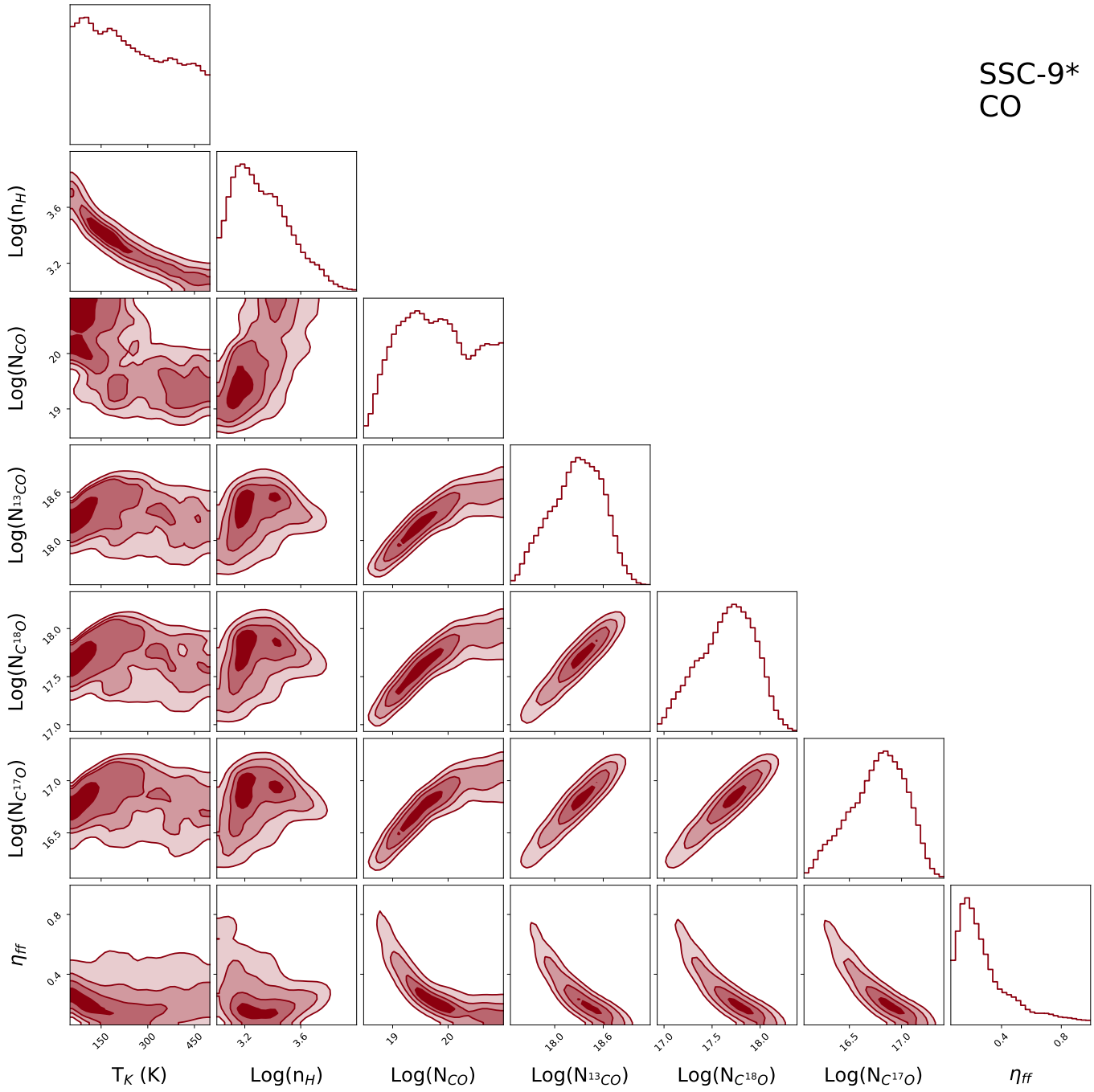

Fig. C.10. Posterior distributions for SSC-9* of the kinetic temperature, neutral H_2 number density, beam filling factor and column densities of CO, ^{13}CO, C^{18}O, and C^{17}O, as predicted by `RADEX`.

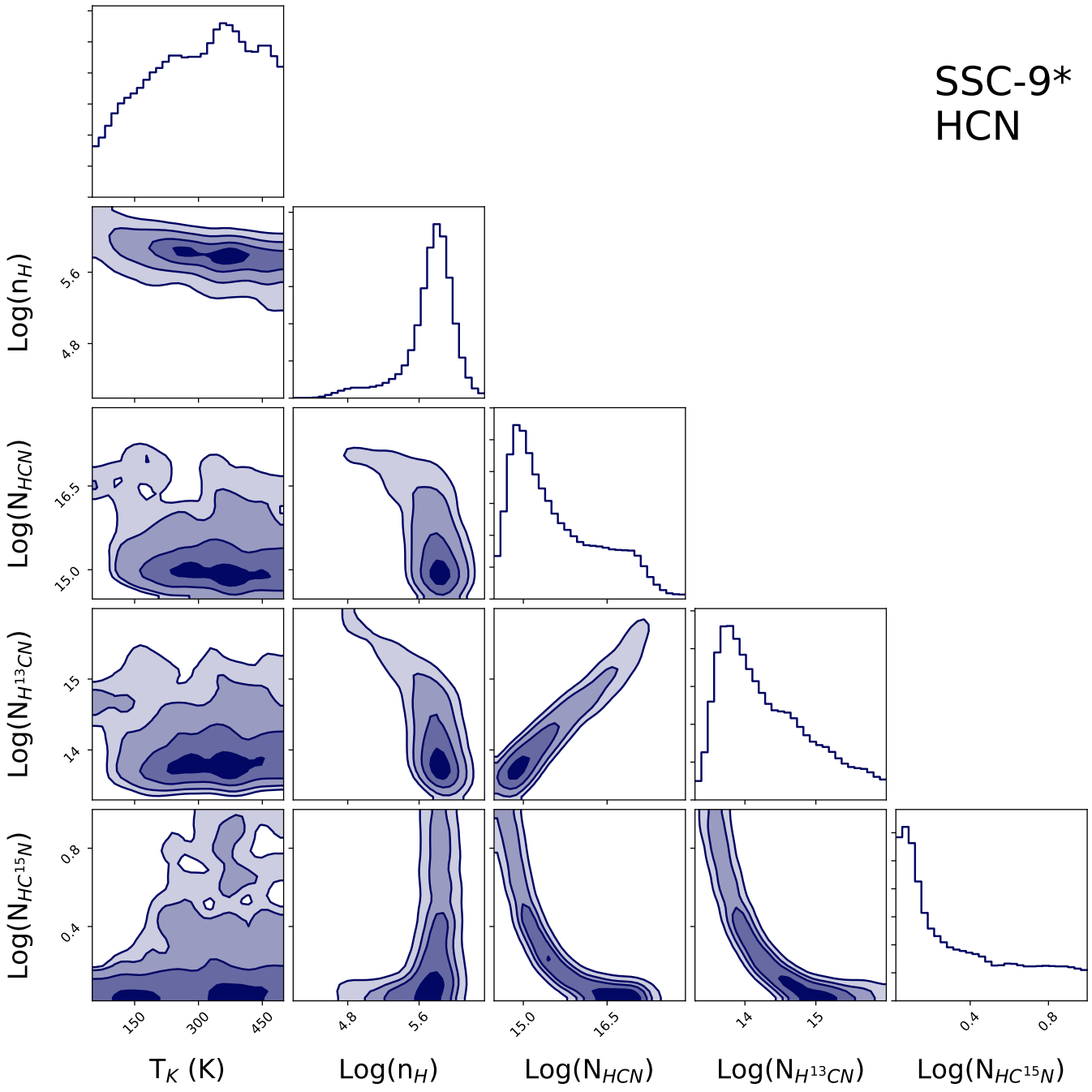

Fig. C.11. Posterior distributions for SSC-9* of the kinetic temperature, neutral H_2 number density, beam filling factor and column densities of HCN, $H^{13}CN$ and HC ^{15}N, as predicted by `RADEX`.

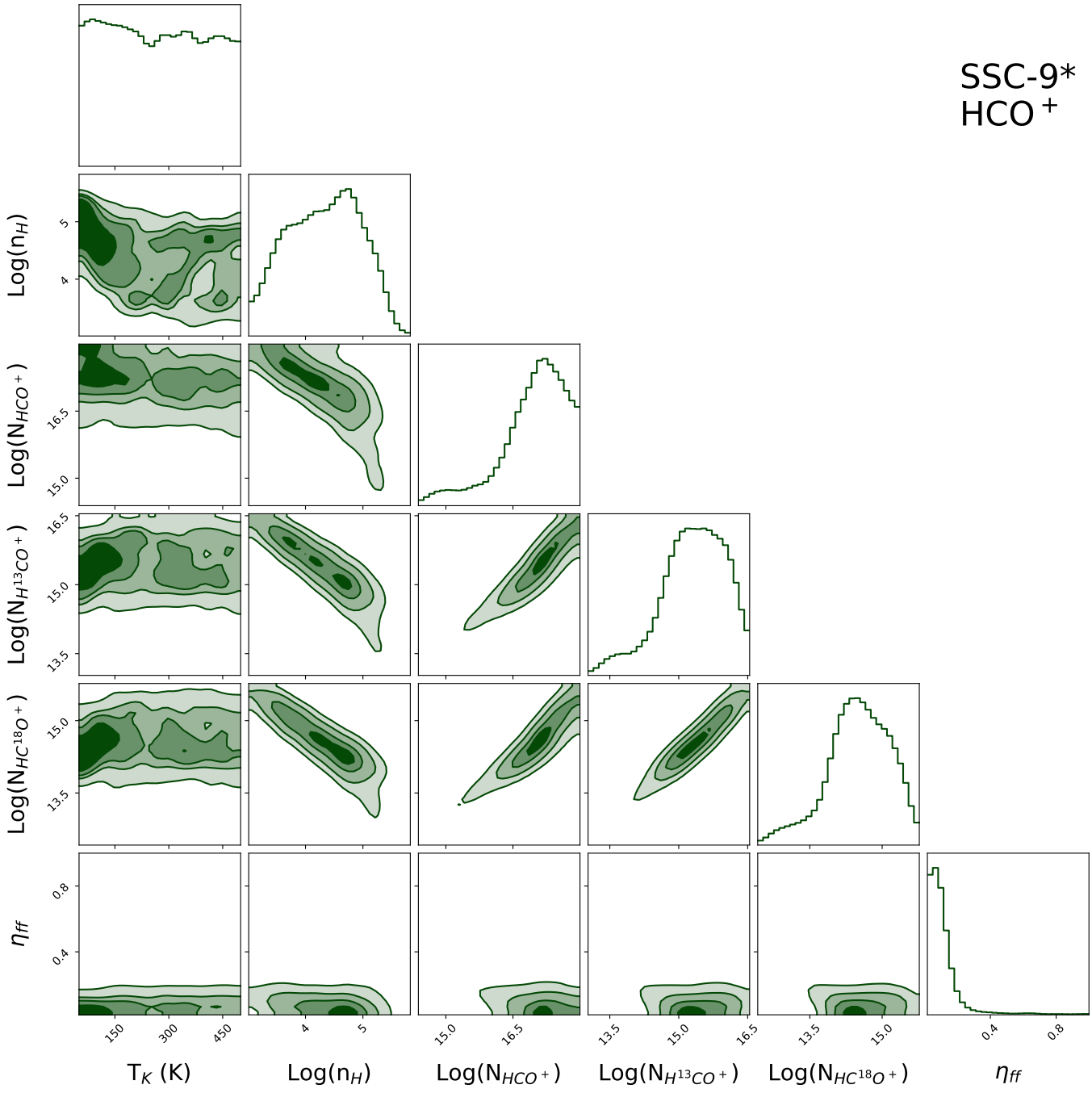

Fig. C.12. Posterior distributions for SSC-9* of the kinetic temperature, neutral H_2 number density, beam filling factor and column densities of HCO^+, $H^{13}CO^+$ and $HC^{18}O^+$, as predicted by RADEX.

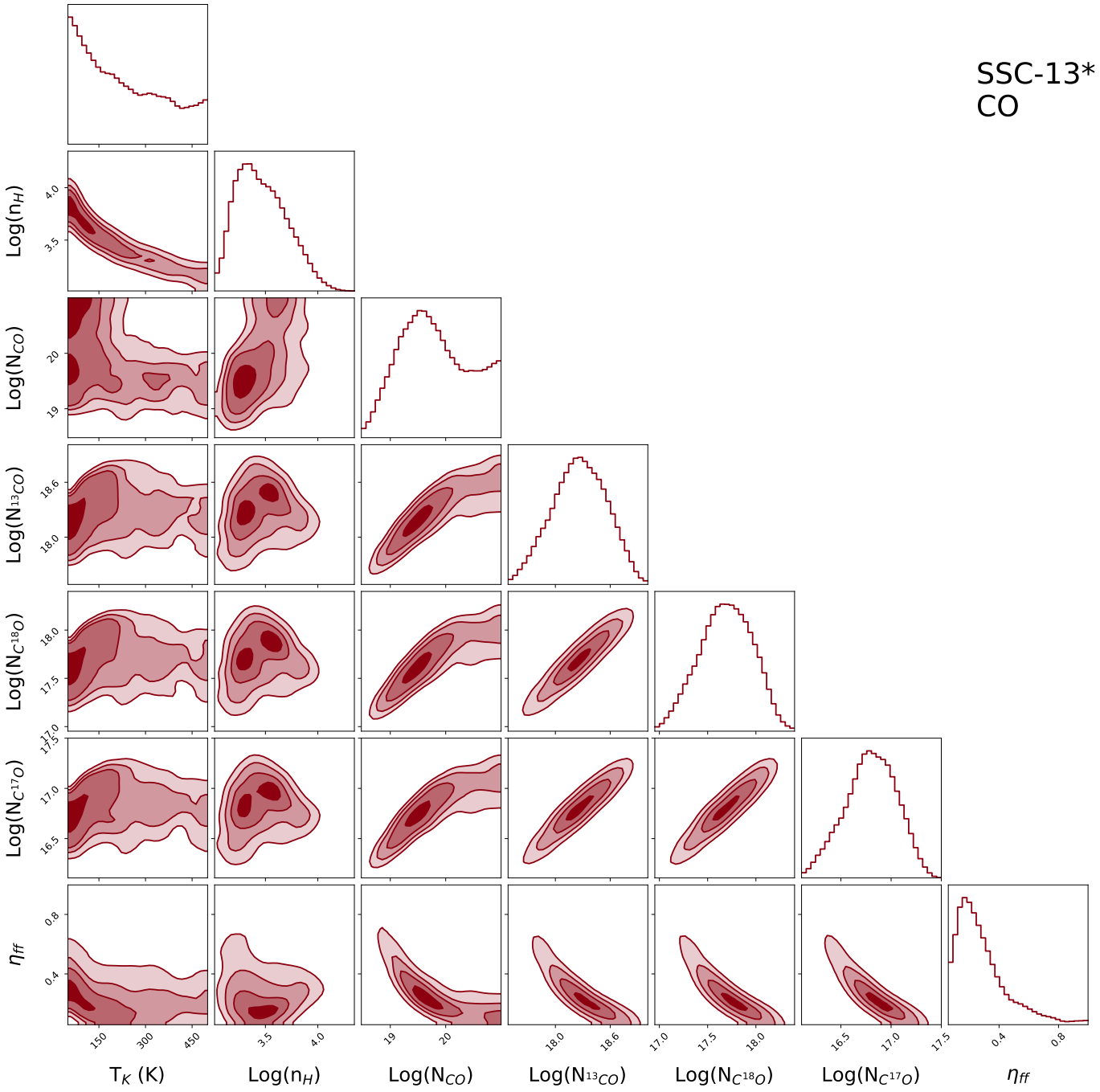

Fig. C.13. Posterior distributions for SSC-13* of the kinetic temperature, neutral H_2 number density, beam filling factor and column densities of CO, ^{13}CO, C^{18}O, and C^{17}O, as predicted by `RADEX`.

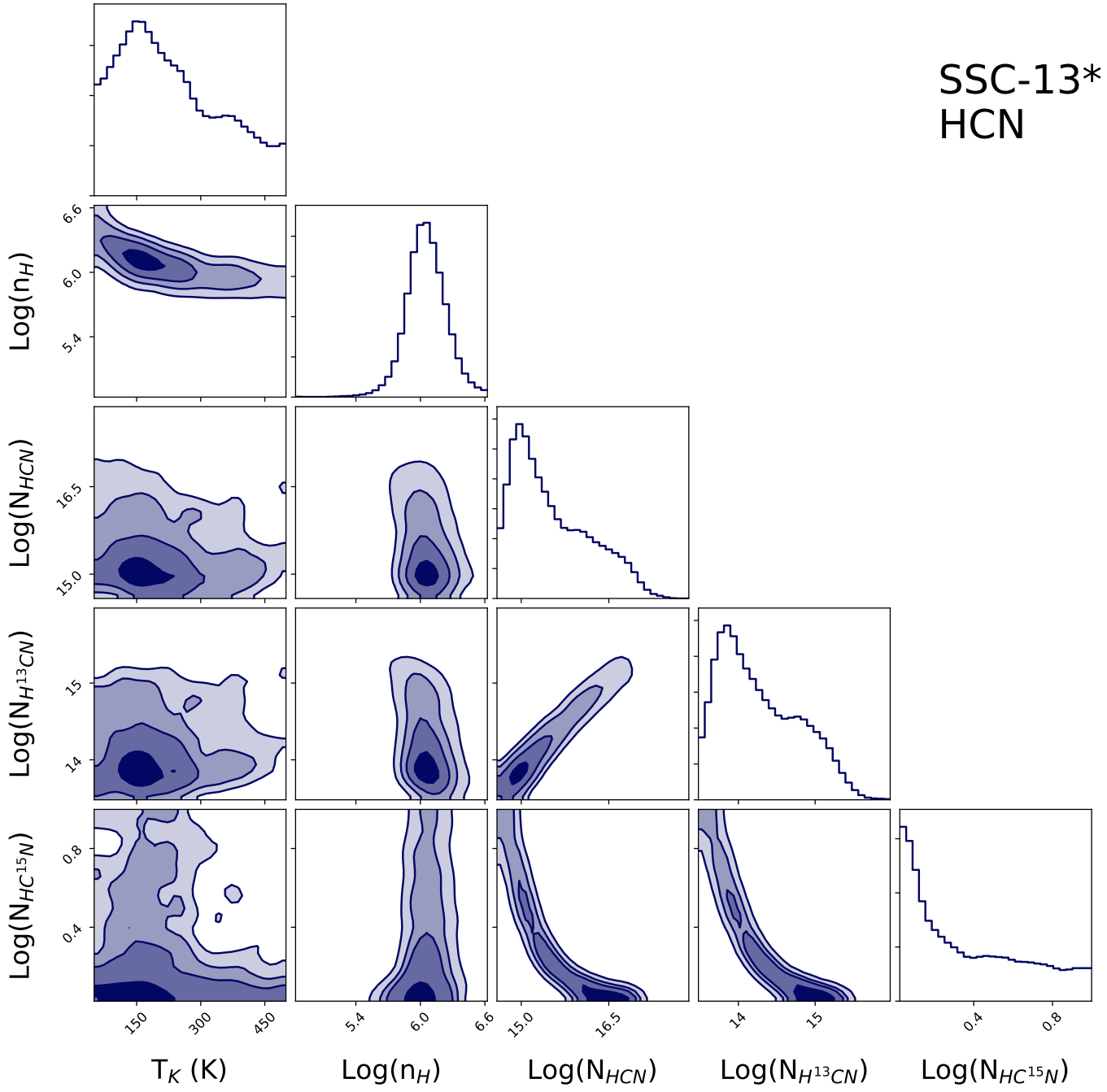

Fig. C.14. Posterior distributions for SSC-13* of the kinetic temperature, neutral H_2 number density, beam filling factor and column densities of HCN, $H^{13}CN$ and $HC^{15}N$, as predicted by `RADEX`.

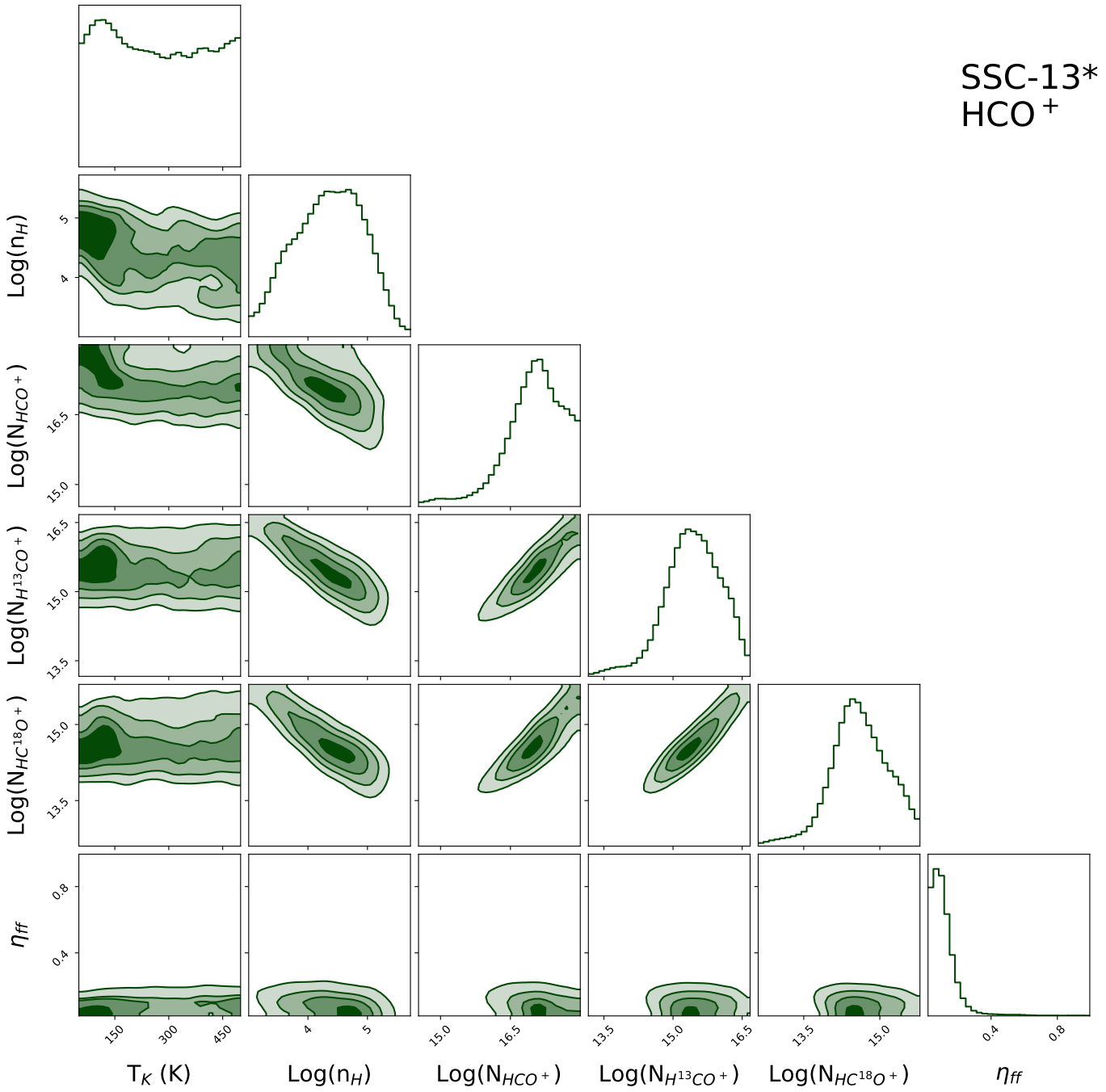

Fig. C.15. Posterior distributions for SSC-13* of the kinetic temperature, neutral H_2 number density, beam filling factor and column densities of HCO^+, $H^{13}CO^+$ and $HC^{18}O^+$, as predicted by RADEX.

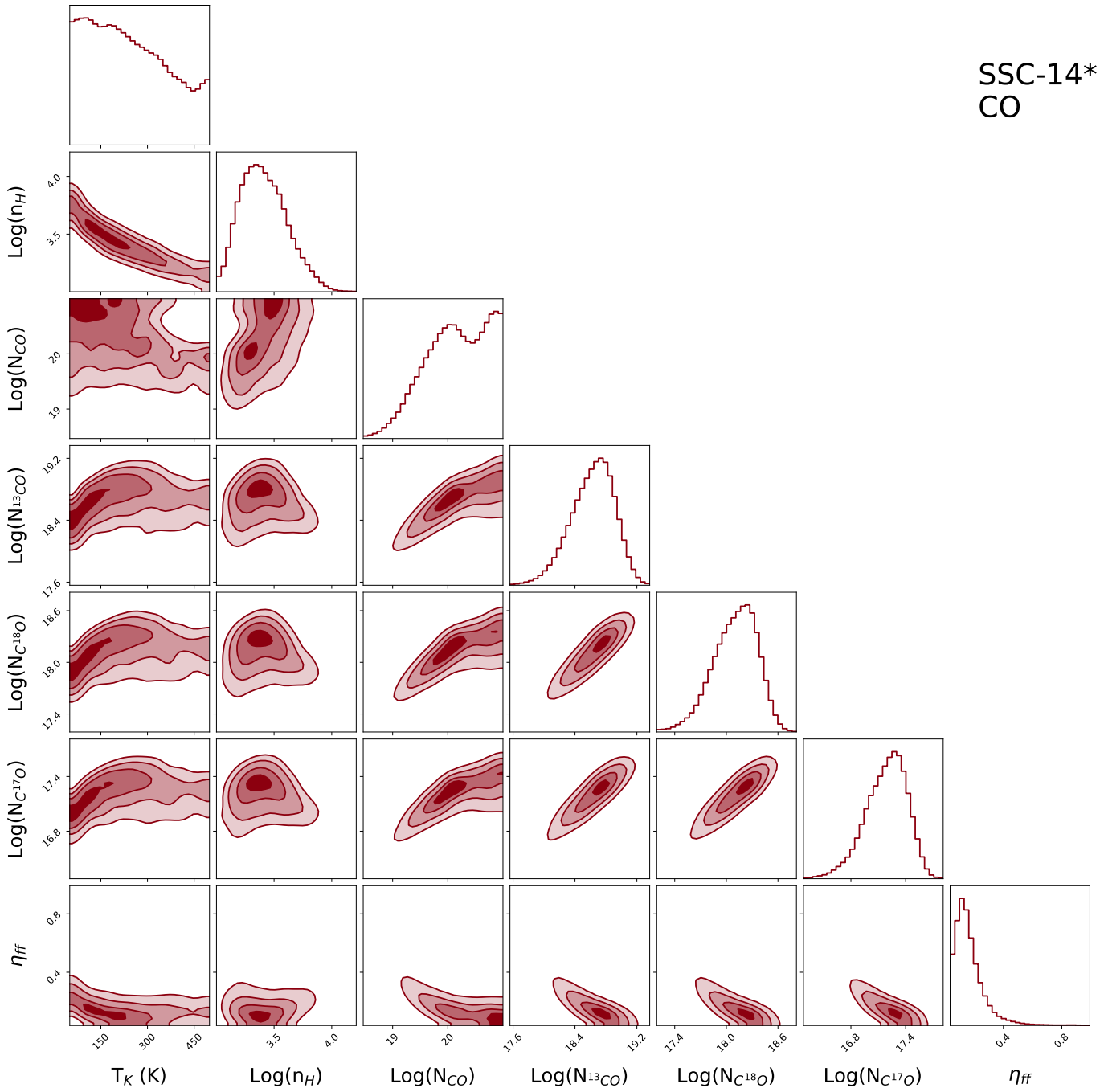

Fig. C.16. Posterior distributions for SSC-14* of the kinetic temperature, neutral H_2 number density, beam filling factor and column densities of CO, ^{13}CO, C^{18}O, and C^{17}O, as predicted by `RADEX`.

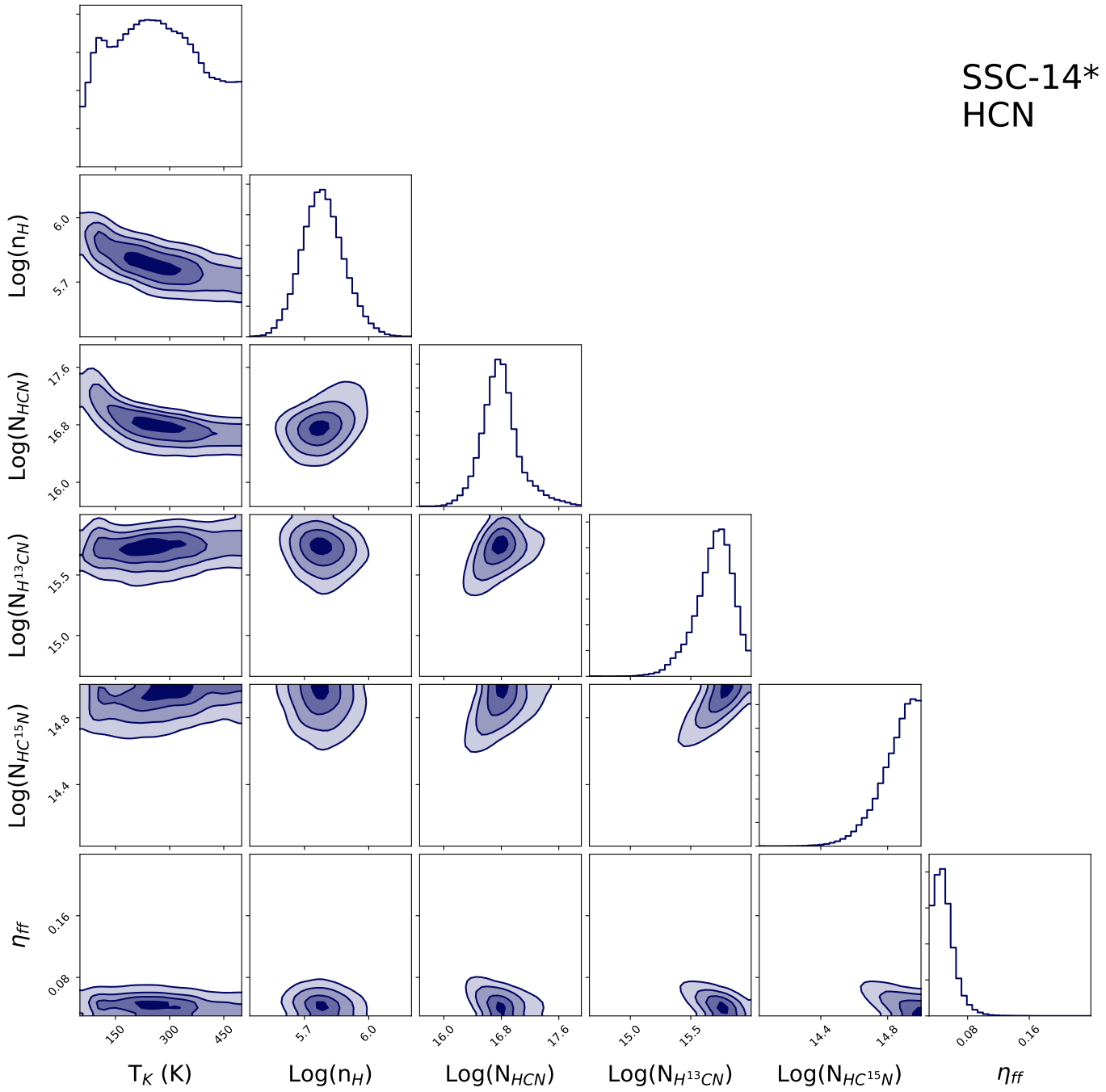

Fig. C.17. Posterior distributions for SSC-14* of the kinetic temperature, neutral H_2 number density, beam filling factor and column densities of HCN, $H^{13}CN$ and HC ^{15}N, as predicted by `RADEX`.

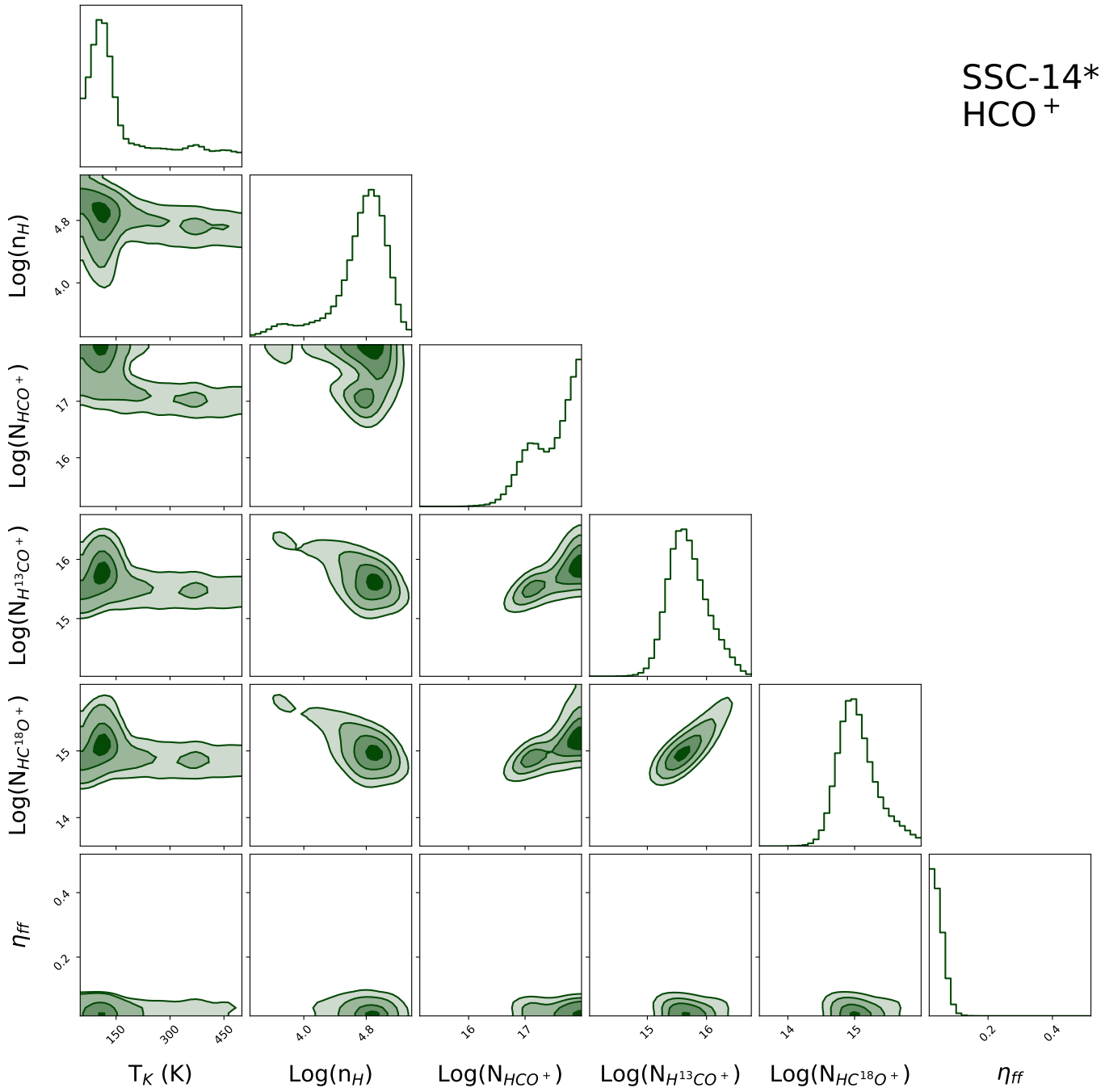

Fig. C.18. Posterior distributions for SSC-14* of the kinetic temperature, neutral H_2 number density, beam filling factor and column densities of HCO^+, $H^{13}CO^+$ and $HC^{18}O^+$, as predicted by RADEX.

Appendix D: Ultranest RADEX model fitting summary

This appendix contains a summary of the `Ultranest RADEX` model fitting results for molecule and isotopologue within each SSC* region.

Table D.1. Median, 16th, and 84th percentile parameter value results from the `Ultranest RADEX` model fitting of the CO, ^{13}CO, C^{18}O, and C^{17}O observed transition lines for each SSC* region.

Location	T_K (K)	Log(n_H) (cm^{-3})	Log(N_{CO}) (cm^{-2})	Log($N_{^{13}CO}$) (cm^{-2})	Log($N_{C^{18}O}$) (cm^{-2})	Log($N_{C^{17}O}$) (cm^{-2})	Beam filling factor
SSC-1*	253^{123}_{-120}	$3.19^{0.18}_{-0.12}$	$20.0^{0.6}_{-0.7}$	$18.5^{0.2}_{-0.4}$	$18.0^{0.2}_{-0.3}$	$17.1^{0.2}_{-0.3}$	$0.167^{0.164}_{-0.056}$
SSC-4*	252^{158}_{-133}	$3.26^{0.20}_{-0.16}$	$19.9^{0.7}_{-0.6}$	$18.5^{0.3}_{-0.3}$	$17.9^{0.2}_{-0.3}$	$17.0^{0.2}_{-0.3}$	$0.206^{0.185}_{-0.077}$
SSC-7*	256^{150}_{-129}	$3.26^{0.21}_{-0.15}$	$19.9^{0.7}_{-0.7}$	$18.4^{0.3}_{-0.4}$	$17.8^{0.2}_{-0.3}$	$16.9^{0.2}_{-0.3}$	$0.211^{0.201}_{-0.077}$
SSC-9*	239^{170}_{-134}	$3.29^{0.24}_{-0.17}$	$19.8^{0.8}_{-0.7}$	$18.3^{0.3}_{-0.4}$	$17.7^{0.3}_{-0.3}$	$16.8^{0.2}_{-0.3}$	$0.233^{0.245}_{-0.098}$
SSC-13*	203^{183}_{-117}	$3.44^{0.28}_{-0.21}$	$19.7^{0.8}_{-0.6}$	$18.3^{0.3}_{-0.3}$	$17.7^{0.3}_{-0.3}$	$16.8^{0.2}_{-0.3}$	$0.241^{0.199}_{-0.103}$
SSC-14*	227^{158}_{-123}	$3.39^{0.21}_{-0.18}$	$20.2^{0.6}_{-0.6}$	$18.7^{0.2}_{-0.3}$	$18.1^{0.2}_{-0.3}$	$17.2^{0.2}_{-0.2}$	$0.137^{0.103}_{-0.045}$

Table D.2. Median, 16th, and 84th percentile parameter value results from the `Ultranest RADEX` model fitting of the HCN, H^{13}CN, and HC^{15}N observed transition lines for each SSC* region.

Location	T_K (K)	Log(n_H) (cm^{-3})	Log(N_{HCN}) (cm^{-2})	Log($N_{H^{13}CN}$) (cm^{-2})	Log($N_{HC^{15}N}$) (cm^{-2})	Beam filling factor
SSC-1*	271^{134}_{-109}	$5.48^{0.10}_{-0.09}$	$16.5^{0.3}_{-0.3}$	$15.2^{0.3}_{-0.3}$	$14.4^{0.2}_{-0.2}$	$0.069^{0.041}_{-0.022}$
SSC-4*	294^{131}_{-120}	$5.54^{0.09}_{-0.08}$	$16.6^{0.3}_{-0.3}$	$15.3^{0.2}_{-0.2}$	$14.4^{0.2}_{-0.2}$	$0.063^{0.031}_{-0.017}$
SSC-7*	325^{120}_{-147}	$5.56^{0.09}_{-0.08}$	$16.7^{0.2}_{-0.3}$	$15.5^{0.2}_{-0.2}$	$14.5^{0.1}_{-0.2}$	$0.055^{0.023}_{-0.011}$
SSC-9*	310^{127}_{-144}	$5.78^{0.15}_{-0.26}$	$15.4^{1.2}_{-0.5}$	$14.2^{0.9}_{-0.5}$	-	$0.260^{0.472}_{-0.187}$
SSC-13*	211^{163}_{-99}	$6.05^{0.17}_{-0.14}$	$15.3^{1.0}_{-0.5}$	$14.2^{0.7}_{-0.4}$	-	$0.293^{0.437}_{-0.222}$
SSC-14*	264^{138}_{-130}	$5.78^{0.09}_{-0.09}$	$16.8^{0.2}_{-0.2}$	$15.7^{0.1}_{-0.2}$	$14.9^{0.1}_{-0.1}$	$0.047^{0.012}_{-0.007}$

Table D.3. Median, 16th, and 84th percentile parameter value results from the `Ultranest RADEX` model fitting of the HCO$^+$, H^{13}CO$^+$, and HC^{18}O$^+$ observed transition lines for each SSC* region.

Location	T_K (K)	Log(n_H) (cm^{-3})	Log(N_{HCO^+}) (cm^{-2})	Log($N_{H^{13}CO^+}$) (cm^{-2})	Log($N_{HC^{18}O^+}$) (cm^{-2})	Beam filling factor
SSC-1*	297^{143}_{-137}	$4.44^{0.22}_{-0.57}$	$16.9^{0.6}_{-0.5}$	$15.3^{0.6}_{-0.4}$	$14.7^{0.6}_{-0.3}$	$0.068^{0.032}_{-0.018}$
SSC-4*	291^{147}_{-151}	$4.77^{0.13}_{-0.13}$	$17.0^{0.4}_{-0.3}$	$15.2^{0.2}_{-0.2}$	$14.6^{0.1}_{-0.2}$	$0.045^{0.017}_{-0.010}$
SSC-7*	180^{208}_{-67}	$4.93^{0.14}_{-0.14}$	$17.2^{0.6}_{-0.3}$	$15.3^{0.2}_{-0.2}$	$14.7^{0.1}_{-0.1}$	$0.033^{0.011}_{-0.008}$
SSC-9*	270^{154}_{-154}	$4.36^{0.62}_{-0.73}$	$17.1^{0.6}_{-0.8}$	$15.4^{0.6}_{-0.7}$	$14.5^{0.6}_{-0.6}$	$0.081^{0.066}_{-0.030}$
SSC-13*	263^{165}_{-148}	$4.38^{0.57}_{-0.66}$	$17.1^{0.6}_{-0.6}$	$15.4^{0.6}_{-0.6}$	$14.6^{0.6}_{-0.5}$	$0.091^{0.064}_{-0.032}$
SSC-14*	125^{212}_{-36}	$4.80^{0.21}_{-0.34}$	$17.6^{0.3}_{-0.5}$	$15.7^{0.4}_{-0.3}$	$15.0^{0.3}_{-0.2}$	$0.039^{0.014}_{-0.010}$

Appendix E: H39α recombination line fitting

In Figure E.1, we show spectra in heliocentric velocity with respect to the H39α transition at a rest frequency of 106.73738 GHz for each of the SSC*s. Other spectral emission present comes from He39α at a rest frequency of 106.78084 GHz which corresponds to -122.1 km s^{-1} offset in velocity from H39α, and C_2H_3CN at a rest frequency of 106.64139 GHz or offset by -269.6 km s^{-1} with respect to H39α. We have marked the rest velocity velocities of He39α (cyan) and C_2H_3CN (purple) with respect to the fitted central velocity of H39α (pink) with vertical dashed lines in the top panel.

We simultaneously fit Gaussian profiles to H39α and He39α emission, and for SSC-13* C_2H_3CN emission as well. Gaussian fits to the emission are shown with dotted lines for H39α (pink), He39α (cyan) and C_2H_3CN (purple). The sum of the Gaussian fits is shown by a solid red line.

By combining Equations A4 and A14 from Emig et al. (2020), the total ionising photon rate expressed in terms of the flux density of the recombination line is

$$Q_0 = \left(6.473 \times 10^{51}\ \mathrm{s}^{-1}\right)\left(\frac{\int S_{\mathsf{n}}\,\mathrm{d}v}{100\ \mathrm{mJy\ km\ s}^{-1}}\right)\left(\frac{1}{b_{\mathsf{n}+1}}\right)$$
$$\left(\frac{D}{4\ \mathrm{Mpc}}\right)\left(\frac{\nu_{\mathsf{n}}}{100\,\mathrm{GHz}}\right)\left(\frac{T_e}{10^4\ \mathrm{K}}\right)^{0.667-0.034\ln\left(T_e\ /\ 10^4\ \mathrm{K}\right)}$$

where $\int S_{\mathsf{n}}\,\mathrm{d}v$ is the integrated flux density of the RRL with principal quantum number n, $b_{\mathsf{n}+1}$ is the LTE departure coefficient at $\mathsf{n}+1$, D is the distance to the emitting region, T_e is the electron temperature, and ν_{n} is the rest frequency of the RRL. To derive the total ionising photon rate at each SSC*, we use the Gaussian area of the H39α emission or when necessary, the sum of the Gaussian areas of the H39α components. We assume a temperature of $T_e = 6000$ K and an LTE departure coefficient of $b_{\mathsf{n}+1} = 0.8$ (Bendo et al. 2015; Mills et al. 2021).

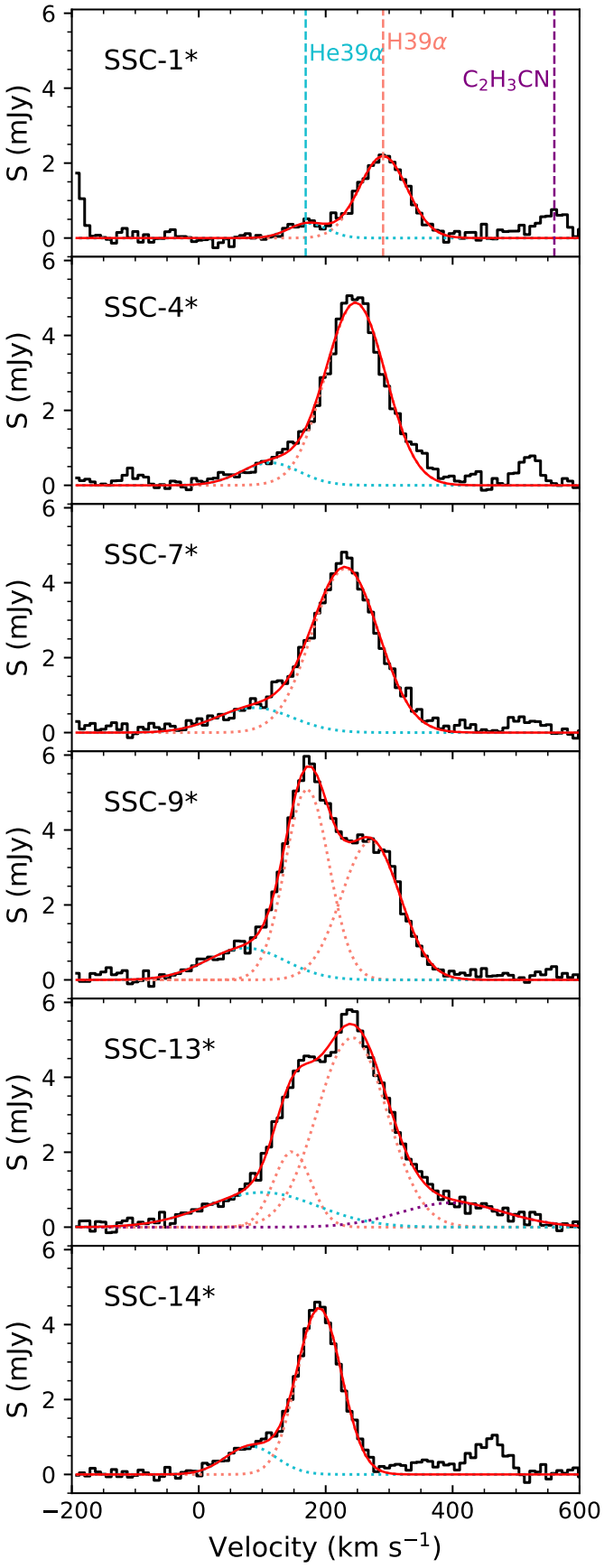

Fig. E.1. Spectra and resulting spectral fitting of H39α.

Appendix F: Optical depths

This section contains the predicted optical depths of the best-fitting RADEX model for each region and for each transition.

Table F.1. Transition optical depth, τ_{ul}, predicted for each region from the best-fitting RADEX model.

Transition	SSC-1*	SSC-4*	SSC-7*	SSC*-9	SSC-13*	SSC-14*
			CO			
(1-0)	0.31	0.00	0.00	0.16	0.22	0.2
(2-1)	4.87	3.93	3.94	3.33	2.86	4.45
(3-2)	10.11	8.27	8.32	7.04	6.14	9.41
			^{13}CO			
(1-0)	0.29	0.28	0.27	0.22	0.18	0.33
(2-1)	1.13	0.83	0.79	0.61	0.44	0.83
(3-2)	2.02	1.60	1.53	1.18	1.02	1.92
			C^{18}O			
(1-0)	0.17	0.13	0.12	0.09	0.08	0.18
(2-1)	0.57	0.38	0.33	0.24	0.18	0.42
(3-2)	0.88	0.65	0.58	0.42	0.40	0.95
			C^{17}O			
(1-0)	0.03	0.02	0.02	0.01	0.01	0.03
(2-1)	0.09	0.06	0.05	0.04	0.03	0.07
(3-2)	0.12	0.09	0.08	0.06	0.06	0.14
			HCN			
(1-0)	0.11	0.27	0.39	0.24	0.17	0.62
(2-1)	3.42	3.27	3.13	0.41	0.21	2.44
(3-2)	6.31	6.51	6.50	0.86	0.67	5.46
(4-3)	7.35	8.58	9.05	0.65	0.63	8.1
			H^{13}CN			
(1-0)	0.19	0.28	0.37	0.04	0.03	0.54
(2-1)	1.23	1.19	1.29	0.07	0.03	1.16
(3-2)	1.46	1.67	2.11	0.12	0.11	2.51
(4-3)	0.73	1.03	1.60	0.07	0.08	2.77
			HC^{15}N			
(1-0)	0.07	0.10	0.11	-	-	0.23
(2-1)	0.40	0.36	0.36	-	-	0.47
(3-2)	0.34	0.36	0.41	-	-	0.88
(4-3)	0.12	0.15	0.19	-	-	0.62

Table F.1. continued.

Transition	SSC-1*	SSC-4*	SSC-7*	SSC*-9	SSC-13*	SSC-14*
			HCO^+			
(1-0)	3.30	1.40	1.39	4.47	4.28	4.26
(2-1)	13.49	8.23	8.35	17.43	16.79	17.75
(3-2)	25.03	16.73	17.38	32.77	31.46	36.67
(4-3)	31.8	24.72	26.86	42.83	40.88	57.43
			$H^{13}CO^+$			
(1-0)	1.22	0.18	0.01	1.74	1.81	0.76
(2-1)	4.44	2.53	2.44	5.59	6.09	4.97
(3-2)	3.81	2.87	3.31	4.78	5.74	7.20
(4-3)	1.23	1.38	2.07	1.54	2.15	5.51
			$HC^{18}O^+$			
(1-0)	0.67	0.07	0.04	0.64	0.67	0.34
(2-1)	2.17	1.30	1.33	1.58	1.74	2.64
(3-2)	1.13	1.02	1.31	0.59	0.70	2.52